PLASMONIC NANOANTENNAS FOR ENHANCED LIGHT-MATTER INTERACTIONS AND GRAPHENE BASED TUNABLE NANOPHOTONIC DEVICES

A DISSERTATION SUBMITTED TO

THE GRADUATE SCHOOL OF ENGINEERING AND SCIENCE

OF BILKENT UNIVERSITY

IN PARTIAL FULFILLMENT OF THE REQUIREMENTS FOR

THE DEGREE OF

DOCTOR OF PHILOSOPHY

IN

PHYSICS

By

Semih Çakmakyapan

January, 2015

PLASMONIC NANOANTENNAS FOR ENHANCED LIGHT-MATTER INTERACTIONS AND GRAPHENE BASED TUNABLE NANOPHOTONIC DEVICES

By Semih Çakmakyapan

January, 2015

We certify that we have read this thesis and that in our opinion it is fully adequate, in scope and in quality, as a dissertation for the degree of Doctor of Philosophy.

Prof. Dr. Ekmel Özbay(Advisor)

Assoc. Prof. Dr. Mehmet Özgür Oktel

Assist. Prof. Dr. Ali Kemal Okyay

Prof. Dr. Oğuz Gülseren

Assoc. Prof. Dr. Hamza Kurt

Approved for the Graduate School of Engineering and Science:

Prof. Dr. Levent Onural
Director of the Graduate School

ABSTRACT

PLASMONIC NANOANTENNAS FOR ENHANCED LIGHT-MATTER INTERACTIONS AND GRAPHENE BASED TUNABLE NANOPHOTONIC DEVICES

Semih Çakmakyapan
Ph.D. in Physics
Advisor: Prof. Dr. Ekmel Özbay
January, 2015

Focusing, manipulating and beaming of electromagnetic waves are important for many applications such as antennas, optical isolators, biological sensor, chemical sensors, and solar cells. There is an extensive research about the manipulation of light, and its interaction with different types of materials including subwavelength structures. However, manipulating light at the nanoscale has many difficulties due to the diffraction limit. In this thesis, we mainly focus on the characterization and experiments of subwavelength plasmonic structures. We investigated the spatial distribution of the electric field through subwavelength slits by using symmetric and non-symmetric periodic metallic grating structures in order to obtain one-way transmission, off-axis beaming, collimation and diode-like beaming. We also studied various plasmonic structures such as circular rings and fractal bowtie antennas. After combining them with Raman active molecules, we showed that these plasmonic structures can be used as efficient surface enhanced Raman spectroscopy substrates. Finally, we designed, fabricated and measured nanoantennas and split ring resonators on graphene in order to tune their optical response using the electrically controllable doping property of the graphene.

Keywords: Surface Plasmons, Subwavelength Localization, Metamaterial, Split Ring Resonator, Metallic Gratings, Plasmonic Lens, Raman Spectroscopy, Nanoantennas, Graphene..

ÖZET

ZENGİNLEŞTİRİLMİŞ IŞIK-MADDE ETKİLEŞİMLERİ İÇİN PLAZMONİK NANOANTENLER VE GRAFEN TABANLI AYARLANABİLİR NANOFOTONİK AYGITLAR

Semih Çakmakyapan
Fizik, Doktora
Tez Danışmanı: Prof. Dr. Ekmel Özbay
Ocak, 2015

Elektromanyetik dalgaları odaklamak, kontrol etmek ve yönlendirmek; anten, optik izolasyon, biyolojik sensör, kimyasal sensör ve güneş pilleri gibi uygulamar için önem taşımaktadır. Işığın yönlendirilmesi ve dalga boyu altı yapılar dahil olmaz üzere farklı maddelerle etkileşimi yaygın bir araştırma konusudur. Ancak, nano boyutlarda ışığı kontrol etmek kırılım limitleri sebebi ile zorlaşmaktadır. Bu tezde, dalga boyu altı plazmonik yapıların karakterizasyonu ve deneyleri üzerine yoğunlaştık. Dalga boyu altı yarıkları simetrik ve asimetrik metalik ızgara yapılarını tek yönlü geçirgenlik, eksen dışı yönelim ve hizalama için kullanarak, uzaysal elektrik alan dağılım özelliklerini inceledik. Dairesel halkalar ve papyon antenler gibi plazmonik yapılar üzerine çalışıldı. Bu yapıları Raman aktif moleküller ile birleştirerek, bu plazmonik yapıların zenginleştirilmiş yüzey Raman spektroskopisi için verimli bir katman olabileceğini gösterdik. Son olarak, grafen üzerine nanoantenler ve ayrık halka rezonatörleri üretip, grafenin elektriksel olarak taşıyıcı yoğunluğunun değiştirilmesi özelliğini kullanarak plazmonik yapıların optik yanıtının ayarlanabilirliğini gösterdik.

Anahtar sözcükler: Yüzey Plazmonları, Dalga Boyu Altı Lokalizasyon, Metamalzeme, Ayrık Halka Rezonatörü, Metal Izgara, Plazmonik Lens, Raman Spektroskopisi, Nanoantenler, Grafen.

Acknowledgement

It is my great pleasure to express my gratitude to my supervisor Prof. Ekmel Özbay for his support, understanding, guidance, patience and encouragement. I would like to thank him very much for making this dissertation possible for me. It has been an honor for me to complete my Ph.D. degree under his supervision at Nanotechnology Research Center, where I grew up and evolved as a researcher.

I would like to thank Assoc. Prof. Mehmet Özgur Oktel, who built an important part of my physics background. I feel extremely fortunate that I had the chance to take four courses from him. I am grateful for his friendly approach, time and support.

I would like to thank Assist. Prof. Ali Kemal Okyay for his endless support and kindness towards me. His valuable suggestions and comments improved the quality of my thesis. I feel indebted to him for his time and help whenever I needed.

I would like to thank Prof. Oğuz Gülseren and Assoc. Prof. Hamza Kurt for accepting to be a part of my thesis committee and taking their valuable time to evaluate my dissertation.

I would like to thank Assoc. Prof. Ceyhun Bulutay, from whom I learned a lot of physics and good personality traits.

I thank all of the former and present Nanotechnology Research Center members. I am grateful to Assist. Prof. Hümeyra Çağlayan, who introduced me to Prof. Özbay and spent time to train me and collaborate with me. I would like to thank Dr. Serkan Bütün for training me in the clean room. I am thankful to Dr. Neval Cinel for her unrequited friendship, support and for our fruitful discussions during our collaborations. I want to thank Adil Burak Turhan, who became my first trainer for nanolithography techniques; I can never forget his help and friendship. I would like to thank Dr. Engin Arslan, Dr. Zhaofeng Li, Dr. Andriy Serebryannikov, Mehmet Mutlu and Dr. Atilla Özgür Çakmak for their kindness and invaluable help in our joint studies. It was a great pleasure to work and to be friends with Doğan Yılmaz, Pakize Öztop, Özgür Kazar, and Ayça Emen. I also would like to express my thankfulness to the Özbay Group members: Okan Ateşal, Yasemin Kanlı, Dr. Deniz Çalışkan, Dr. Bayram Bütün, Dr. Mutlu

Gökkavas, Ramazan Özsoy, Ahmet Toprak, Ahmet Akbaş, Dr. Özlem Şen, Dr. Funda Gündoğdu, Cihan Çakır, and Dr. Tolga Kartaloğlu. Their suggestions and support have helped me during my Ph.D. studies.

I feel very lucky to have amazing friends like Emre Ozan Polat, Gülesin Eren, Damla Ateş, Seher Acer, Can Fahrettin Koyuncu, Alper Gürlek, İpek Mete, Pelin Avcu, Mehmet Ergin and Saygın Yağ. They always stood by my side and made me feel better with their friendship. I am thankful to Pervin İskenderova and Merve Tunci, whose immense friendship made me stronger in both joy and bitterness. I am very glad to have known two super cool people, Melis Aygar and Onur Özdemir, who boosted my mood all the time.

I feel elated to be friends with Murat Çolakoğlu, who has been there for me for 14 years now. He shared my joy with the greatest sincerity and shed light on me in the darkest of times. His presence gives me strength and makes me brave to explore new horizons. *Thanks for showing me the comet. You are my person.*

Finally, I would like to thank my parents and my sister for their support and unconditional love. I am thankful to them for giving me the freedom to choose the path I want to walk. I dedicate this work to my baby nephew Kuzey.

Contents

1 Introduction **1**

1.1 Organization of the thesis 3

2 Transmission and Beaming Properties of Metallic Grating Structures with Single Subwavelength Slit **5**

2.1 Introduction 5

2.2 One-way transmission through symmetric gratings with different interfaces 7

2.2.1 Design 7

2.2.2 Results and Discussion 8

2.3 Multiplexing and collimation through asymmetric gratings 13

2.3.1 Design 13

2.3.2 Results and Discussion 14

2.4 One-way diode like beaming with symmetric gratings and metamaterial based polarization rotator 21

2.4.1 Design 21

2.4.2 Results and Discussion 22

2.5 Conclusion 24

3 Surface Enhanced Raman Spectroscopy Substrate based on Plasmonic Structures **27**

3.1 Introduction 27

3.2 Circular plasmonics lenses with a single ring 29

3.2.1 Design and Fabrication 30

3.2.2 Preparation of self-assembled monolayer Raman active molecules on plasmonic lenses 30
3.2.3 Results and Discussions 32
3.3 SERS enhancement with the concentric ring structures 36
3.3.1 Design and Fabrication 36
3.3.2 Imaging surface plasmons 40
3.3.3 Simulation Results 41
3.3.4 Experimental Results and Discussions 43
3.4 Fractal bowtie nanoantennas 46
3.4.1 Design and Fabrication 47
3.4.2 Measurements and Simulations 49
3.4.3 Results and Discussions 50
3.5 Conclusion 56

4 Graphene Based Nanophotonic Devices 57
4.1 Introduction 57
4.2 Electrical characterization of graphene 59
4.3 Epitaxial graphene transistor with transparent top-gate for resonance broadening and tuning of split ring resonators 60
4.3.1 Design and Fabrication 60
4.3.2 Results and Discussions 63
4.4 Resonance tuning and broadening of bowtie nanoantennas on graphene 67
4.4.1 Design and Fabrication 69
4.4.2 Results and Discussion 71
4.5 Coupling enhancement of split ring resonators on graphene 75
4.5.1 Methods 76
4.5.2 Results and Discussion 79
4.6 Conclusion 81

5 Conclusion 84

A Publications in SCI journals 103

List of Figures

2.1 Schematic of the metallic (aluminum) gratings. Slit width is 2 mm, and groove depth is 4 mm. Sample A: (upper plot) Grating period of the front side is b=16 mm, and grating period of back side is a=26 mm. Sample B: (lower plot) Grating period of the front side is b=16 mm, and grating period of back side is c=22 mm. 7

2.2 Calculated transmission for Samples A, C, D, E, and F at θ=30^o. Illumination side is specified in brackets for Samples A, D, and F. 9

2.3 Measured and calculated transmission results for Sample A at θ=30^o. 9

2.4 Electric field distribution for Sample A at f =9.8 GHz: (a) front-side, and (b) back-side illumination; tilting by 30 degrees. Color bar is normalized to 0.6; maximum is brown. 10

2.5 Calculated angular distribution of transmission at 9.8 GHz for Samples A, C, D, E, and F at θ=30^o. Positive angles represent the right-hand side of the structure, negative angles represent the left-hand side of the structure, and Θ=30^o is defined to correspond to the direction that is perpendicular to the grating. 11

2.6 Measured and calculated angular distribution of transmission at 9.8 GHz for Sample A at θ=30^o. 12

2.7 Measured and calculated angular distribution of transmission at 11.2 GHz for Sample B at θ=0^o. 13

2.8 (a) Geometry of Sample G and schematic of the paths of the incident (red arrows) and outgoing (blue arrows) beams that illustrates the expected collimation effect; front-side illumination (upper left plot) and back-side illumination (lower left plot), (b) Schematic of the experimental setup. 14

2.9 Maps of electric field intensity for Sample G at front-side (a) and back-side (b) illumination; θ=5^o. 15
2.10 Maps of electric field intensity for Sample G at front-side (a) and back-side (b) illumination; θ=$-$5^o. 15
2.11 Field distribution maps at f=14.5 GHz for Sample G at front-side(a) and at back-side (b) illumination; θ=5^o. 16
2.12 Field distribution maps at f=14.5 GHz for Sample G at front-side(a) and at back-side (b) illumination; θ=$-$5^o. 17
2.13 Time-dependent power flow calculated at the slit center for (a) the front-side, and (b) the back-side of the structure. 17
2.14 Angular distribution of electric field intensity at f=14.5 GHz: (a) for several positive values of θ, simulation; (b) for two values of θ that differ in sign, simulation; (c) same as (b), experiment; (d) same as (b) but for larger $|\theta|$, simulation; front-side (solid lines) and back-side (dashed lines) illuminations. 19
2.15 Calculated angular distribution of the electric field intensity at (a) $\theta = 5^o$ and (b) $\theta = 10^o$ for three frequency values, at front-side (solid lines) and back-side (dashed lines) illuminations. 21
2.16 (a) Schematic of the metallic grating with a subwavelength slit, (b) front layer of the polarization rotator, and (c) schematic of the experimental setup. 22
2.17 Magnitudes of the experimental linear transmission coefficients for the polarization rotator. The maximum of $\left|T_{sp}\right|$ is observed at 6.98 GHz. The inset shows the geometry of the subwavelength mesh sandwiched between the front and back layers of the rotator. 23
2.18 Magnitudes of the experimental linear co-polarized transmission coefficients of the metallic grating with a single subwavelength slit. 24

2.19 Field intensity distributions of p-polarized components for (a) the only grating for p-polarized incidence, (b) the composite structure for s-polarized forward propagating waves, and (c) field intensity distribution of the s-polarized component for p-polarized backward propagating waves. The grating with a subwavelength slit is enclosed in a dashed white rectangle and the position of the rotator is shown by a black line. 25

3.1 Scanning electron microscopy image of ring-shaped hole on silver film. 31
3.2 SERS spectra of p-ATP obtained from (a) plasmonic lens, and (b)thin silver film. 33
3.3 SERS spectra obtained from plasmonics lenses with different slit widths. 34
3.4 SERS intensity ratio depending on slit width. 34
3.5 SERS spectra obtained from plasmonic lenses having the same slit width and different ring diameters. 35
3.6 SERS intensity ratio depending on changes ring diameter changes. 36
3.7 Electric field intensity $|E|^2$ distribution on the plasmonic lens. . . 37
3.8 (a) Illustration of fabrication steps for a five-ring coupled structure (b) schematic of coupled concentric rings (c) schematic of etched concentric rings (d) SEM image of the coupled structure. Inner ring diameter 965 nm, period 500 nm. The scale bar corresponds to 2 μm. 39
3.9 Optical microscope image (a) under white light illumination (b) imaging of surface under LED excitation. The scale bar corresponds to 2 μm for both figures. 40
3.10 Cross-sectional Formula-field distributions $|E|^2$ of the coupled resonant (a, d), coupled nonresonant (b), (e) and etched ring (c), (f) structures, respectively. The same color scale is used for (d), (e) and (f). 42

3.11 SER spectra of Benzenethiol from the *coupled ring* structures and plain gold film. No background correction is done. Spectra are shifted for a better view. A horizontal axis break is applied to save space. In the legend, the letter P denotes period and the letter D denotes diameter. 44
3.12 SER spectrum of Benzenethiol from the coupled rings and the etched rings. No background correction is done. A horizontal axis break is applied to save space. 45
3.13 Schematics (above) and SEM (below) images of (a) Bowtie, (b) Fractal-1, and (c) Fractal-2 structures. $g = 65nm$, $r = 400nm$, $y = 420nm$. Scale bar is 100 nm. 47
3.14 Transmission spectra of the antenna arrays (a) experiment, (b) simulation results. 51
3.15 Transmission spectra of open and connected Fractal-1 structures: (a) experiment, (b) simulation. 53
3.16 SERS measurement results for Bowtie, Fractal-1 and Fractal-2. . . 54
3.17 Electric field distributions at the Stokes shifted wavelength, 895 nm. (a) Bowtie, (b) Fractal-1, and (c) Fractal-2. The maximum of the color bar is set to the same value for comparison. 55

4.1 Fabricated Van der Pauw Hall device. 60
4.2 Temperature dependence of the sheet carrier density (N_H) and Hall mobility (μ_H) of electrons in the graphene. 61
4.3 Schematic of the device fabrication steps. 61
4.4 DC-IV Measurements (a) drain voltage vs drain current, (b) gate voltage vs drain current; inset shows drain voltage vs gate current. 64
4.5 Transmission measurements before and after depositing ITO and SiO_2 layers. 65
4.6 Transmission measurements under different gate voltage differences, $\Delta\ V$, for (a) Device 1, and (b) Device 2. 66
4.7 Line width difference, $\Delta\ \lambda$, and quality factor variation for (a) Device 1, and (b) Device 2.(Black squares represent the line width difference, and red triangles represent the quality factor.) 68

4.8 (a) Fabricated four-contact Van der Pauw device for Hall measurements, (b) optical microscopy image of the tunable bowtie device, i.e. active graphene region with nanostructures between drain (D) and source (S) contacts; inset showing SEM picture of a bowtie antenna, (c) measured drain-source current with respect to the gate voltage, and (d) calculated variation of carrier concentration and Fermi energy with respect to the gate voltage difference ΔV. . . . 70

4.9 (a) Measured reflectance spectra at different ΔV; enlarged view of resonance peaks shown in the inset, and (b) relative reflectivity of bowtie antenna array at different gate voltages; inset showing the x-component of electric field intensity for Sample 1 at 5.5 μm and 7 μm. 72

4.10 Calculated reflectance spectra at different ΔV. 73

4.11 Quality factor (black squares) and line width difference (red dots) under different gate bias. 74

4.12 Relative reflectivity of Sample 2 for (a) TE polarization, electric field in the x-direction, and (b) TM polarization, electric field in the y-direction. 75

4.13 (a) Cross-section view of the tunable SRR device; schematics and SEM image of (b) SRR-1, and (c) SRR-2 structures, scale bar is 100 nm. w = 70 nm, u = 400 nm, g = 40 nm, and h = 120 nm. . 77

4.14 DC-IV measurements: (a) current between drain and source under applied gate voltage, (b) current vs. voltage dependence and resistance of graphene. 77

4.15 Reflectivity spectra of SRR-1 structure (a) experiment, (b) simulation results. The resonance peak shifts to longer wavelengths. . 79

4.16 Reflectivity spectra of SRR-2 structure (a) experiment, (b) simulation results. The resonance wavelength shifted 95 nm. 80

4.17 Resonance wavelength shift with respect to the reflectivity measurement taken at the charge neutrality point for (a) SRR-1, and (b) SRR-2; λ_{res} represents the resonance wavelength, and λ_0 is the resonance wavelength at the charge neutrality point, $\Delta V = 0V$, so that the difference $|\lambda_{res} - \lambda_0|$ gives the shift with respect to the undoped graphene. Electric field distributions at resonance frequencies for (c) SRR-1 at 3.5 μm, (d) SRR-2 at 3.9 μm; the maximum of the color bar is set to the same value in both figures for comparison, and the electric field is in the x-direction. 82

Chapter 1

Introduction

Advances in optoelectronics have led the scientists to control and manipulate the light for efficient devices. There has been a considerable progress in nanostructured material characterization for enhanced performance and miniaturization of the nanophotonic integrated circuits. Nanophotonics is a growing research field, which leads to potential optical devices that can control and manipulate light at the nanometer scale [1]. The field has attracted high attention due to the potential applications of optical devices by controlling, manipulating and amplifying light on the nanometer scale, constructing novel sensors, and building photonics circuits [2].

As the device sizes get smaller, it becomes more difficult to focus the electromagnetic wave because of the diffraction limit. Plasmonics have been a growing field of research and an emerging branch of the nanophotonics. Nanophotonics research is mainly focuses on understanding and manipulation of surface plasmons generated on metal surfaces.

Surface plasmons are collective oscillation of conduction band electrons on a noble metal surface excited by electromagnetic light. The free electrons respond collectively by oscillating in resonance with the electromagnetic wave. The effective wavelength of resonant surface plasmons is less than the free space of the

radiation [3], which provides confinement of the incident field into subwavelength dimensions.

Recent progresses in nanolithography techniques provide controllable and simpler methods to pattern metals at nanoscale. These improvements open up new doors to use the surface plasmon properties in various applications. For instance, surface plasmons are promising especially for near field optics [4], magneto-optic data storage [5], solar cells [6], surface enhanced Raman spectroscopy [7, 8], and biosensing [9, 10] applications.

Another important class of plasmonic nanostructures is the metamaterials. Metamaterials have attracted attention over the years, since they provide the flexibility to design structures with the desired permittivities and permeabilities, including negative refractive index. These artificial materials have special electromagnetic wave responses that cannot be obtained by ordinary materials. A well-known example for the metamaterial family is the split ring resonator (SRR), which was originally proposed by Pendry et al. in order to create the desired susceptibility [11]. Later, it was shown experimentally that SRRs can exhibit negative permittivity and permeability values at the same time [12–14]. SRR is a resonant structure where the resonance frequency is determined by the geometrical properties of the structure. SRRs can produce an effect of being electrically smaller when responding to an oscillating electromagnetic field and support resonance wavelengths much smaller than their physical sizes. Therefore, they are able to concentrate the electric field in a small volume and, furthermore, enhance the electric field [12, 15]. Moreover, the metamaterials lead to the applications such as superlenses [16], biosensing [17] and cloaking [18].

The researchers have been seeking for the ways to use the plasmonic structures in active devices, since they are generally resonant structures operating at with a narrow bandwidth. Graphene has been proven to be a good candidate for this goal in last few years. Graphene is a monolayer structure composed of hexagonally arranged carbon atoms. It has a two-dimensional (2D) honeycomb lattice structure. Graphene is a versatile optical material for nanophotonics applications [19] such as metamaterials [20], photodetectors [21], light emitting devices and

ultrafast lasers [22]. Plasmonic resonances in graphene give outstanding potential for designing novel optoelectronic devices by its remarkably high absorption [19, 23, 24]. plasmon resonance of graphene-hybrid device like split ring resonators (SRRs) can be modulated by applying gate voltage [25, 26], which changes the carrier concentration, and thus modulating the optical conductivity [27, 28].

1.1 Organization of the thesis

In Chapter 2, we investigate the transmission and beaming properties of symmetric and asymmetric metallic gratings with a subwavelength slit. We studied the unidirectionality with a metallic grating having different input and output interfaces. Later, we worked on the off-axis directional beaming, and investigated the effect of output surface design on the beam steering and resonance frequency. Then, we designed a composite structure by combining a symmetric metallic grating structure with a 90^o polarization rotator in order to obtain a one-way diode like beaming.

In Chapter 3, we studied several plasmonic structures for surface enhanced Raman spectroscopy (SERS). First, we showed that the SER signal is enhanced with plasmonic lenses having a single circular slit. We further enhanced the SER signal with concentric ring structures. Then, we worked on fractal bowtie nanoantennas which can increase SER efficiency due to the electric field enhancement. Both the simulations and measurement results confirmed that as the degree of fractals are increased the SER signal intensity increase, as well

In Chapter 4, we presented graphene based tunable nanophotonic devices. First, we investigated the electrical properties of graphene. Then, we fabricated and characterized a device with a split ring resonator (SRR) array on epitaxial graphene. We obtained resonance broadening and tuning of split ring resonators by utilizing an epitaxial graphene transistor with transparent top-gate. We also fabricated a back-gated graphene device in order to tune the optical response of bowtie antennas. In order to understand the tuning mechanism in a better way,

we compared two SRR designs having different mode area.

We concluded this thesis with our final remarks in Chapter 5.

Chapter 2

Transmission and Beaming Properties of Metallic Grating Structures with Single Subwavelength Slit

2.1 Introduction

Electromagnetic response of subwavelength apertures has been studied extensively since Bethe showed the theory of diffraction through the subwavelength holes, where the transmitted beam is very low and it is diffracted to every direction [29]. It was shown that the transmitted beam can be enhanced with the aid of periodic corrugations [30]. Optical properties of metallic grating structures can be explained by surface plasmons. A plane or a grooved surface between a Drude metal and dielectric medium can support surface plasmons [31]. Since the skin depth approaches zero for the plane metallic surfaces in the microwave regime, they are not supported by surface plasmons. It was shown theoretically that surface plasmon like modes can be obtained in the perfect electric conductor regime, if there are subwavelength hole arrays on the surface [32]. Later, Hibbins

et al. experimentally showed that the surface plasmon like modes are achievable in microwave frequencies [33]. Coupling the light to the surface plasmons with a periodic structure on the input surface provides enhancement through a subwavelength slit [30]. When the output surface is patterned with periodic gratings, spatial distribution of the transmitted beam can be controlled [34, 35]. Surface plasmon based unidirectional transmission has been studied theoretically and experimentally by using non-symmetric metallic grating structures with one subwavelength slit and double side corrugations [36, 37]. Asymmetric metallic gratings, e.g., those with different corrugations at the left and right side of the exit grating, or at the front and the back side of the structure that has the same corrugations at the left and right sides, enable asymmetry in the excitation of surface plasmons. Asymmetric excitation of surface plasmons at the left and right side can be realized for both slit containing [38, 39] and slit-free [40–43] structures. In the former case, surface plasmons can be unidirectionally excited at the slit-free incidence interface. A proper combination of the corrugation parameters and width and location of the incident beam spot often helps blocking in-plane propagation in unwanted direction(s). In the latter case, surface plasmons can be excited asymmetrically at the left and right sides, or only at one of the sides, while the corrugations at the two sides are either different or placed at one of the sides only. In this case, transmission through a subwavelength hole is a necessary part of the used unidirectional mechanism. In fact, off-axis beaming with a single outgoing beam as that studied in [44, 45] originates from the asymmetry of the surface plasmons with respect to the slit, at the exit interface. In the structures with a single slit, asymmetry in surface plasmons at the left and right sides can be obtained at optical frequencies due to the asymmetry of the slit, while corrugations are absent [46].

2.2 One-way transmission through symmetric gratings with different interfaces

2.2.1 Design

Figure 2.1 shows the metallic grating structures made of aluminum (Al) with a subwavelength slit at the center. The slit width is 2 mm. Both the front-side and back-side interfaces have rectangular periodic grooves of a depth of 4 mm. These values are kept for all the structures considered. Consideration is restricted here to the microwave frequencies.

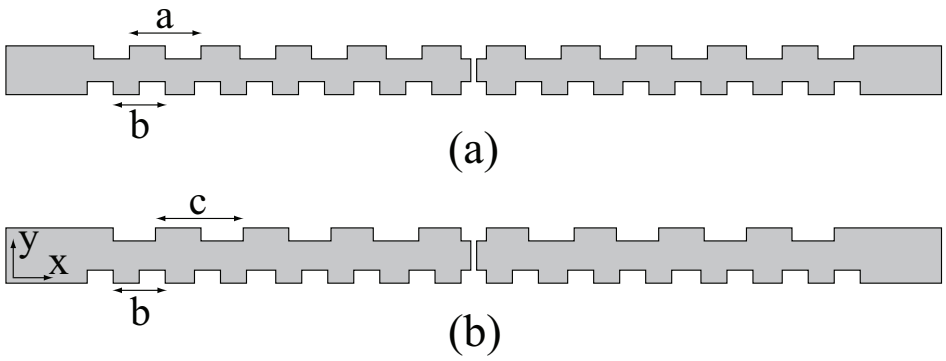

Figure 2.1: Schematic of the metallic (aluminum) gratings. Slit width is 2 mm, and groove depth is 4 mm. Sample A: (upper plot) Grating period of the front side is b=16 mm, and grating period of back side is a=26 mm. Sample B: (lower plot) Grating period of the front side is b=16 mm, and grating period of back side is c=22 mm.

We worked with several different grating structures. Grating periods of the front-side and back-side interfaces are different for both Sample A and Sample B, which are symmetric with respect to the center of the slit. The other studied grating structures differ from Sample A and Sample B, where they have the same corrugations at the both sides, whose period is b=16 mm (Sample C) and a=26 mm (Sample E), or the corrugated front-side interface with b=16 mm (Sample D) and a=26 mm (Sample F) and the non-corrugated back-side interface. The structures are illuminated with a TM-polarized plane wave (electric field vector

is perpendicular to the slit -x-direction-).

2.2.2 Results and Discussion

Transmission results, which are calculated 50 cm away from the center of the slit, are presented in Figure 2.2. The value of θ, the angle of incidence, was chosen so that the angle-dependent resonance frequencies differ substantially, depending on which side is illuminated. Among the presented results, the strongest transmission is observed for Sample A at the resonance frequency at f=9.8 GHz, in case of the front-side illumination, and the resonance frequency at f=15.7 GHz, in case of the back-side illumination. On the other hand, transmission is substantially weaker at f=9.8 GHz in case of the back-side illumination, and approximately f=15.7 GHz in case of the front-side illumination. Hence, strong directional selectivity takes place in the vicinity of these two resonance frequencies. In short, at the resonance frequency of one of the interfaces, the transmission for the other becomes close to zero. This is evidence for the effect of unidirectional transmission. In Figure 2.2, one can see that the same effect is observed for Samples D and F, which show us that the requirement of non symmetry of the grating is necessary, but it is not necessary that the both interfaces are corrugated.

Figure 2.3 compares the results of experiments and simulations for Sample A. The experimental results are obtained by sending an incident beam, with a horn antenna, which is 20 cm away from the input interface. Transmission results are collected 50cm away from the output interface. Measurements were carried out in the frequency range from 8 GHz to 18 GHz by using two standard horn antennas and HP 8510C network analyzer. The main attention has been paid to detection of the cases, when transmission strongly depends on the illumination direction at fixed θ. In Figure 2.3, the coincidence between the simulation and experimental results is quite good.

Electric field distribution has been calculated at the frequencies corresponding to strong transmission, in order to demonstrate the effect of the distance away from the grating. The calculated electric field distributions for Sample A at 9.8

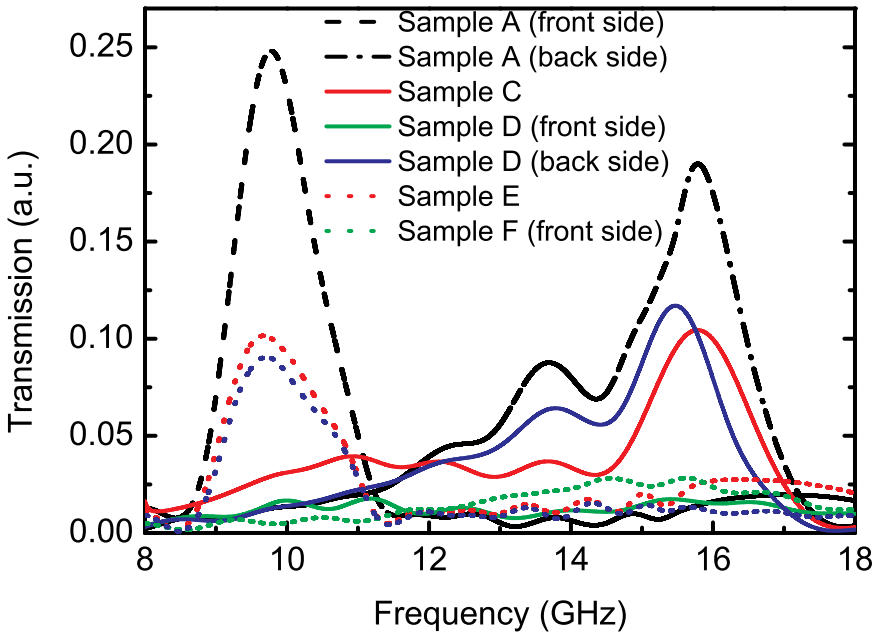

Figure 2.2: Calculated transmission for Samples A, C, D, E, and F at θ=30^o. Illumination side is specified in brackets for Samples A, D, and F.

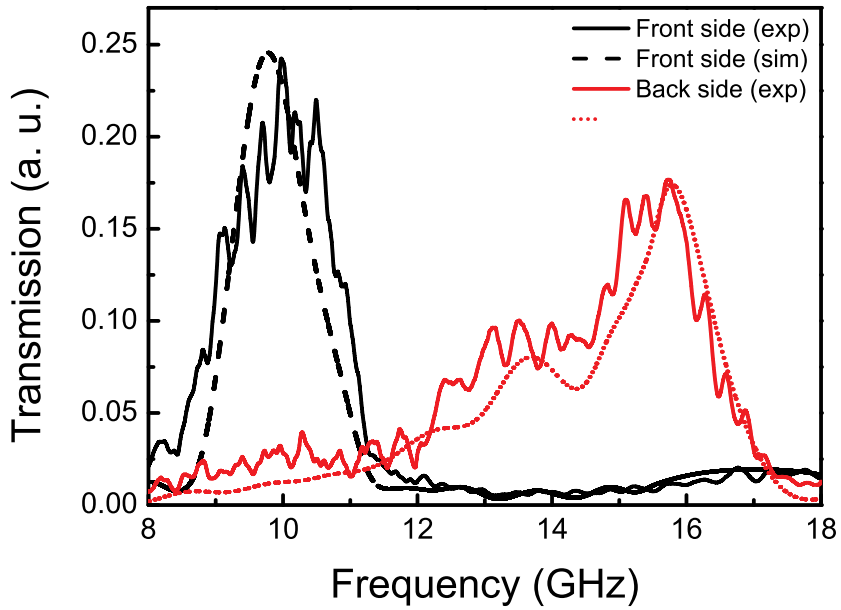

Figure 2.3: Measured and calculated transmission results for Sample A at θ=30^o.

GHz are presented in Figure 2.4 (a) and (b). When Sample A is illuminated from the front side at f=9.8 GHz, a stronger transmission takes place compared to the case where it is illuminated from the back side. For the smaller spatial distances, transmission is higher for the back-side illumination. This situation differs, when moving towards the far zone. For example, the value of electric field intensity is larger in case of the front-side illumination, starting from Y=20 cm, approximately.

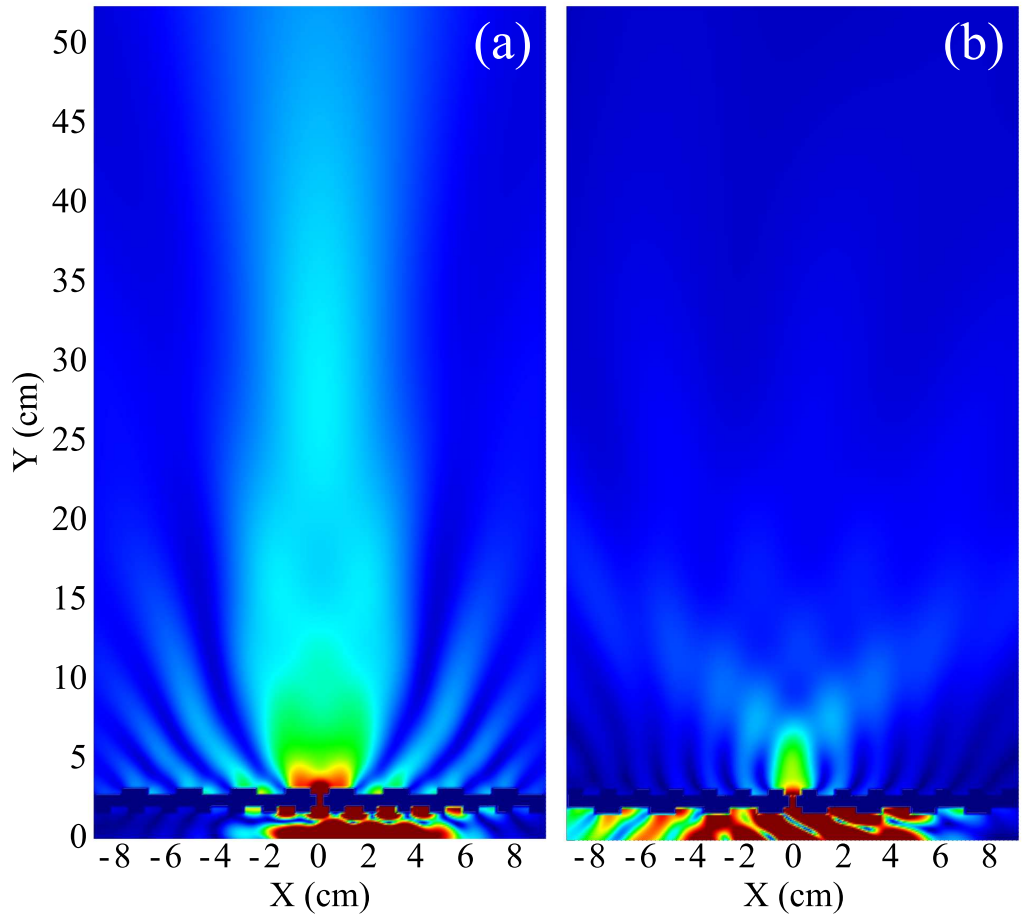

Figure 2.4: Electric field distribution for Sample A at f =9.8 GHz: (a) front-side, and (b) back-side illumination; tilting by 30 degrees. Color bar is normalized to 0.6; maximum is brown.

The observed selectivity can be interpreted in terms of isolation, which is understood in sense of the vanishing effect of the input interface on the appearance of higher-order, i.e., grating originated features in spatial distribution of the field

in the output half-space.

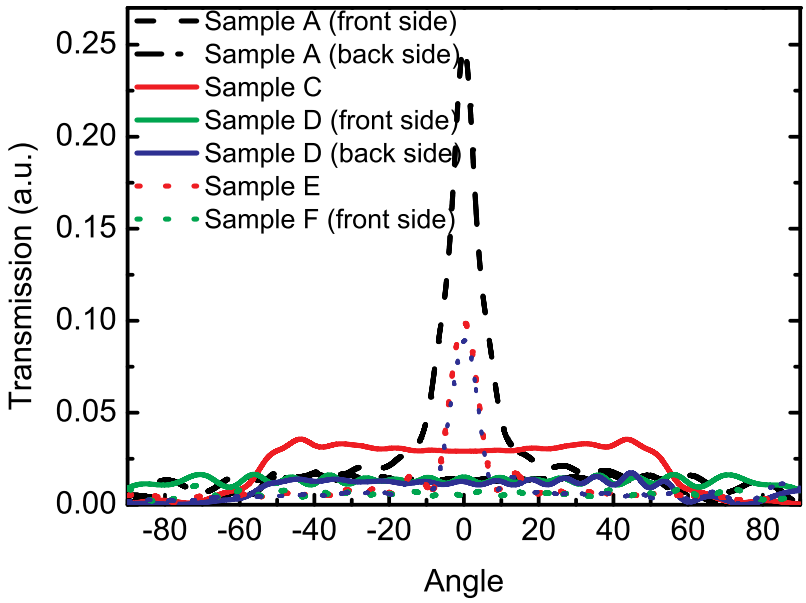

Figure 2.5: Calculated angular distribution of transmission at 9.8 GHz for Samples A, C, D, E, and F at θ=30^o. Positive angles represent the right-hand side of the structure, negative angles represent the left-hand side of the structure, and Θ=30^o is defined to correspond to the direction that is perpendicular to the grating.

In order to validate the appearance of unidirectional transmission in the beaming regime, we investigated details of the angular dependence of transmission near the resonance frequencies, at which the maxima are observed in Figure 2.2 and Figure 2.3. In Figure 2.5, the simulated dependences of transmission on the observation angle, Θ, are compared for the same samples as in Figure 2.2, at f=9.8 GHz. One can see that the beaming occurs not only for Sample A, but also for Samples E and F, for which the output interface is the same. However, strong directional selectivity appears only for non-symmetric gratings for Samples A and F. Half-power bandwidth in the angle domain is almost equal to 9^o, 112^o, and 9^o for Sample A (front-side illumination), Sample C, and Sample E, respectively. In Figure 2.6, the simulated and measured observation angle dependences of transmission are presented for Sample A.

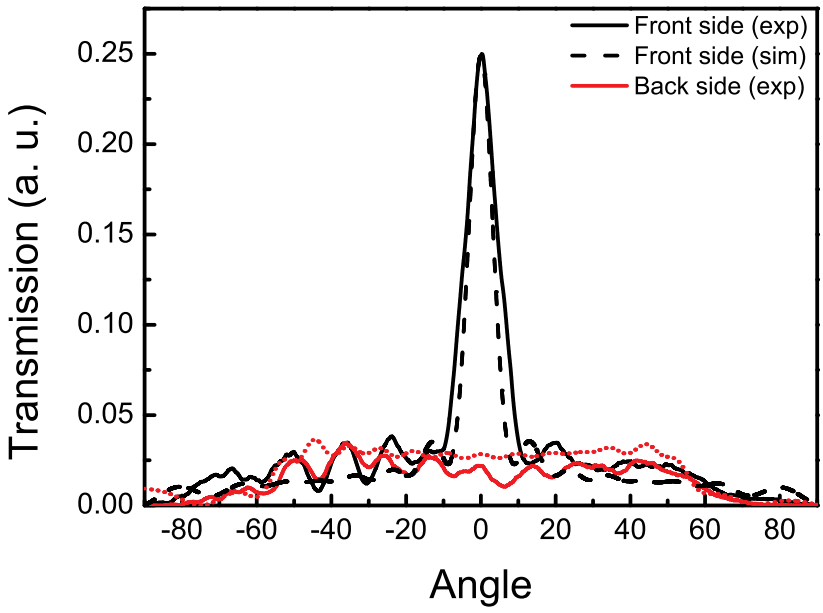

Figure 2.6: Measured and calculated angular distribution of transmission at 9.8 GHz for Sample A at θ=30^o.

Finally, the experimental and simulation results are presented in Figure 2.7 for Sample B, at f=11.2 GHz and θ=0^o. Again, the coincidence is quite good. For the front-side illumination, beaming is observed with the transmission maximum at Θ=0^o. However, when the structure is illuminated from the back side, no beaming occurs. Despite this, rather strong directional selectivity might appear in this case within a certain range of distances from the output interface. In the considered case, it occurs at $0^o < |\Theta| < 30^o$. One can see that it strongly depends on which side is illuminated. The reason is that the period of the output surface determines the grating wavevectors, $k_g = 2\pi/\lambda_g$, where $\lambda_g$is the grating period, which plays a crucial role in the spatial distribution of the transmitted wave [45].

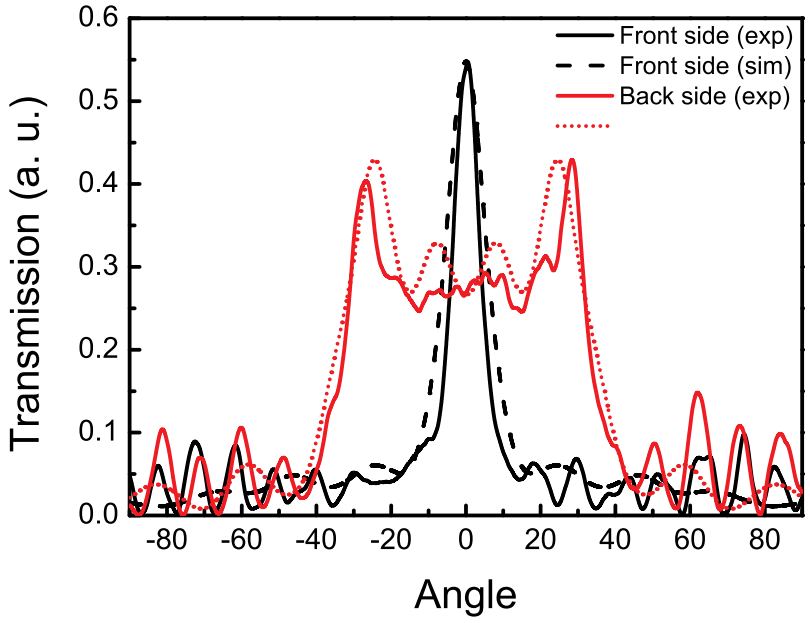

Figure 2.7: Measured and calculated angular distribution of transmission at 11.2 GHz for Sample B at θ=0^o.

2.3 Multiplexing and collimation through asymmetric gratings

2.3.1 Design

Figure 2.8 shows a schematic of the metallic grating with a single subwavelength slit and grating periods a=22 mm, b=14 mm, c=16 mm, and d=16 mm, which we refer to as Sample G; and a=d=22 mm and b=c=14 mm, which we refer to as Sample H [47]. The period of the corrugations at the front side is denoted by c and d, on the left and right side with respect to the slit, respectively. At the back side, the period of the corrugations is denoted by a and b, on the left and the right side with respect to the slit. Both Sample G and Sample H have no symmetry with respect to the vertical and horizontal midplanes. However, in contrast to Sample G, Sample H is symmetric with respect to the slit centerline, i.e., the crossing line of the vertical and horizontal midplanes, which is perpendicular to

the figure plane. The slit width is 2 mm, thickness of the slit channel is 8 mm, and the groove depth is 4 mm. The structure is illuminated with a p-polarized wide Gaussian beam, whose magnetic field vector is parallel to the slit and grooves that are assumed to be infinitely long. Transmission has been calculated at a distance of 50 cm from the slit centerline, which corresponds to the crossing of the horizontal and vertical midplanes, for the observation angle Θ that is varied in a wide range. The incidence angle θ is measured in the counter-clockwise direction from the normal to the incidence side. In turn, Θ is measured in the clockwise direction regarding the normal to the exit side.

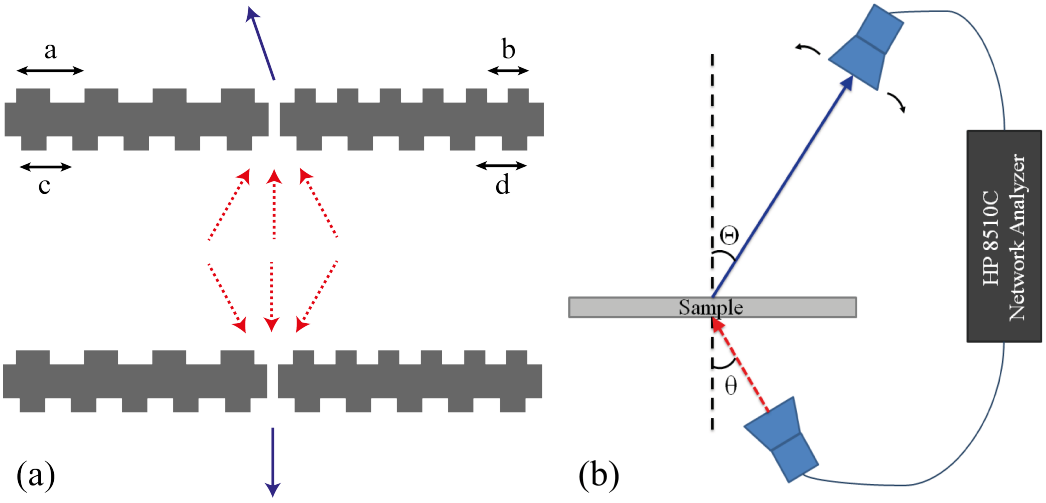

Figure 2.8: (a) Geometry of Sample G and schematic of the paths of the incident (red arrows) and outgoing (blue arrows) beams that illustrates the expected collimation effect; front-side illumination (upper left plot) and back-side illumination (lower left plot), (b) Schematic of the experimental setup.

2.3.2 Results and Discussion

Figure 2.9 presents the maps of the transmission intensity T that are plotted on the (f, Θ)-plane, where f is frequency, for $\theta = 5^o$, while the structure is illuminated from either the front or the back side. The use of such a map to present the transmission results allows us to directly observe the effect of simultaneous variation in f and θ on the direction of propagation of the outgoing beam(s).

As follows from the obtained results, the resonance appears at the front-side illumination near f=14.5 GHz. In this case, the transmitted beam is steered by approximately 13^o due to the specific properties of the spoof plasmons exited at the asymmetric exit interface. From the previous studies of metallic gratings with a slit, it is known that, at the properly adjusted parameters, spoof plasmons that are excited at the input interface are mainly responsible for the transmission enhancement through the subwavelength slit, while those excited at the exit interface result in the output beam shaping [48].

At the back-side illumination, the resonance appears near 15.5 GHz. Now, the maximum is observed at $\Theta = 0$, while the exit interface is symmetric with respect to the vertical midplane.

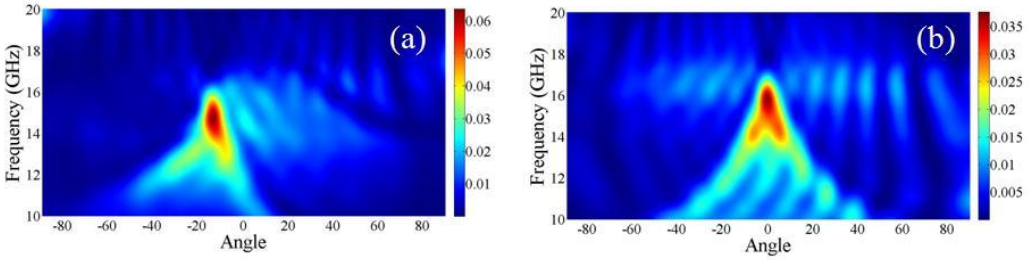

Figure 2.9: Maps of electric field intensity for Sample G at front-side (a) and back-side (b) illumination; θ=5^o.

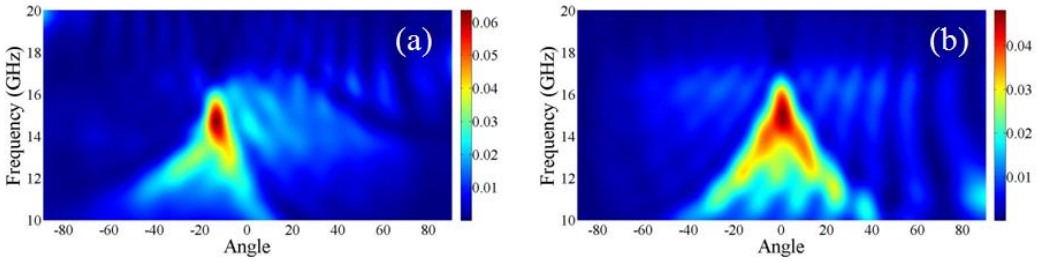

Figure 2.10: Maps of electric field intensity for Sample G at front-side (a) and back-side (b) illumination; θ=-5^o.

Transmission maps for $\theta = -5^o$ are presented in Figure 2.10, for the front-side and back-side illumination. The maps for $\theta = 5^o$ and $\theta = -5^o$ are very similar although not identical. In particular, this confirms the key hypothesis concerning

the dominant effect of the exit interface on the shaping of the outgoing radiation. From the obtained results it follows that when the two wide beams of the same frequency that is taken from the vicinity of the resonance are simultaneously incident at $\theta = 5^o$ and $\theta = -5^o$, the outgoing beams propagate in the same direction, i.e., they collimate.

Figure 2.11 and Figure 2.12 present the electric field distribution at the selected values of f and θ. It is seen that the change of sign of θ does not lead to a substantial change in the field map. Furthermore, the outgoing (off-axis) beams in Figure 2.11(a) and Figure 2.12(a) are expected to show nearly the same magnitude. In turn, the outgoing beams in Figure 2.11(b) and Figure 2.12(b) differ in magnitude. To understand the observed similarities and differences, we calculated the power flow through the slit. Figure 2.13 presents the results obtained at the horizontal midplane in the slit. In case of the front-side illumination, the results at $\theta = 5^o$ and $\theta = -5^o$ are identical. In case of the back-side illumination, they are distinguished. Therefore, one can assume the possibility of the introduction of the equivalent source at the center of the slit, whose characteristics depend on the input interface properties. Correspondingly, a symmetric input interface as in Figure 2.13(a) is associated with the source that is insensitive (in terms of power flow) to the change of $sgn\theta$. In the contrast, an asymmetric input interface as in Figure 2.13(b) is associated with the source, which is affected by the change of $sgn\theta$. It is noteworthy that placing an equivalent source, say, e.g. a dipole inside a slit is rather consistent with the theoretical model applied in [49] to similar structures operating at optical frequencies.

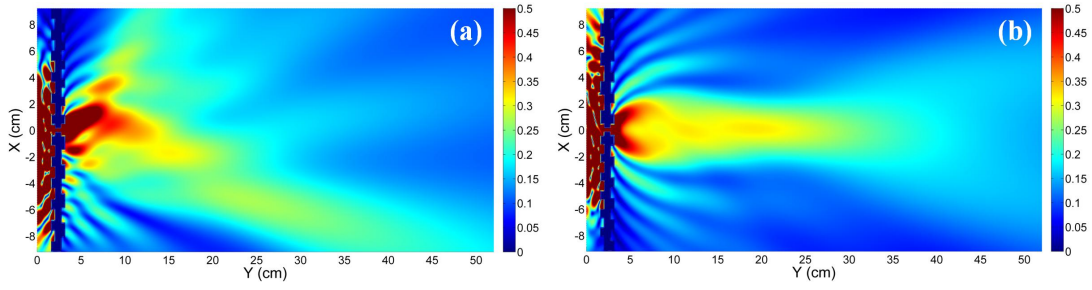

Figure 2.11: Field distribution maps at f=14.5 GHz for Sample G at front-side(a) and at back-side (b) illumination; θ=5^o.

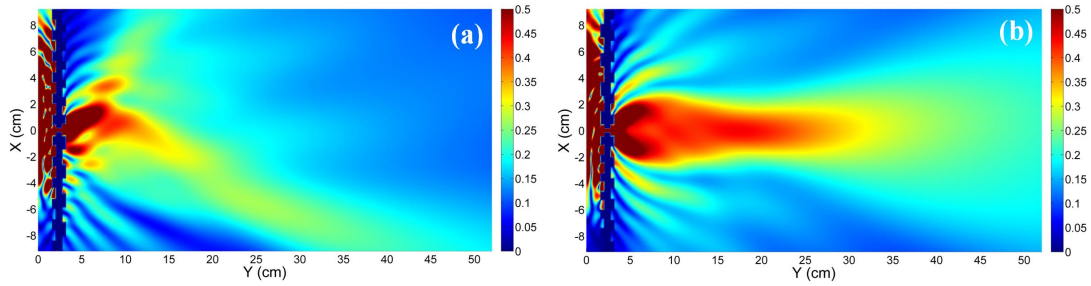

Figure 2.12: Field distribution maps at f=14.5 GHz for Sample G at front-side(a) and at back-side (b) illumination; θ=-5^o.

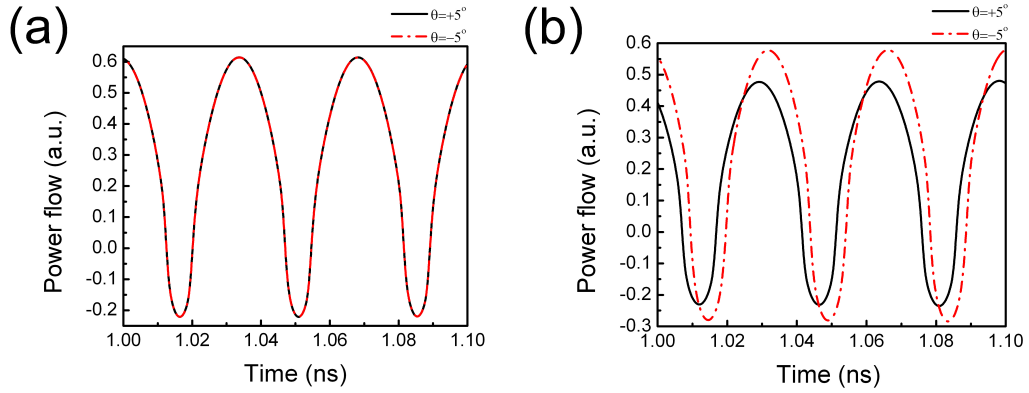

Figure 2.13: Time-dependent power flow calculated at the slit center for (a) the front-side, and (b) the back-side of the structure.

Now, let us examine the angular distribution of the electric field intensity that corresponds to a frequency near the maximum at the front-side illumination. In Figure 2.14(a), it is presented for the four values of $\theta \geq 0$. At the front-side illumination, strongly pronounced beaming occurs, with the transmission maximum at $\Theta = -13.5^o$ that does not depend on θ. The only difference between the curves for different θ is in the beam intensity at the peak, which decreases with increasing θ. This means, in fact, that $|\theta|$ affects the magnitude of the equivalent source while frequency is kept constant. At the back-side illumination, transmission is rather low in the vicinity of $\Theta = -13.5^o$, so that the off-axis beaming with a single transmitted beam appears in a one-way manner. Hence, collimation and one-way beaming can co-exit, as desired. According to the obtained results, the range of θ variation, in which collimation is observed, is at least 30^o wide. In turn, in the vicinity of $\Theta = 0^o$, the contrast between the transmittances for the front-side and the back-side illumination is substantially smaller, thereby leading to a one-way feature not being observed in the transmission. Despite this, collimation still takes place in the on-axis regime at the back-side illumination, although the outgoing beam is now wider than in the off-axis regime at the front-side illumination. Half-power bandwidth values are equal to 11^o at $|\theta| = 5^o$ and 12^o at $|\theta| = 10^o$, for the front-side illumination. A wider outgoing beam at the back-side illumination might be connected with the fact that the exit interface is quite close to but out of the resonance. It can also be seen that the combination of the collimation and one-way beaming observed for the front-side illumination at $-20^o < \Theta < -10^o$ can be the most interesting regime achievable for Sample G.

Figure 2.14(b) presents the simulated angular distribution of the transmitted electric field at f=14.5 GHz, when $\theta = 5^o$ and $\theta = -5^o$. The corresponding beams collimate and, furthermore, show the same magnitudes at the maximum at the front-side illumination. At the same time, the magnitudes are different but the beams still collimate at the back-side illumination. These features are in agreement with the above-used qualitative interpretation in terms of the equivalent source.

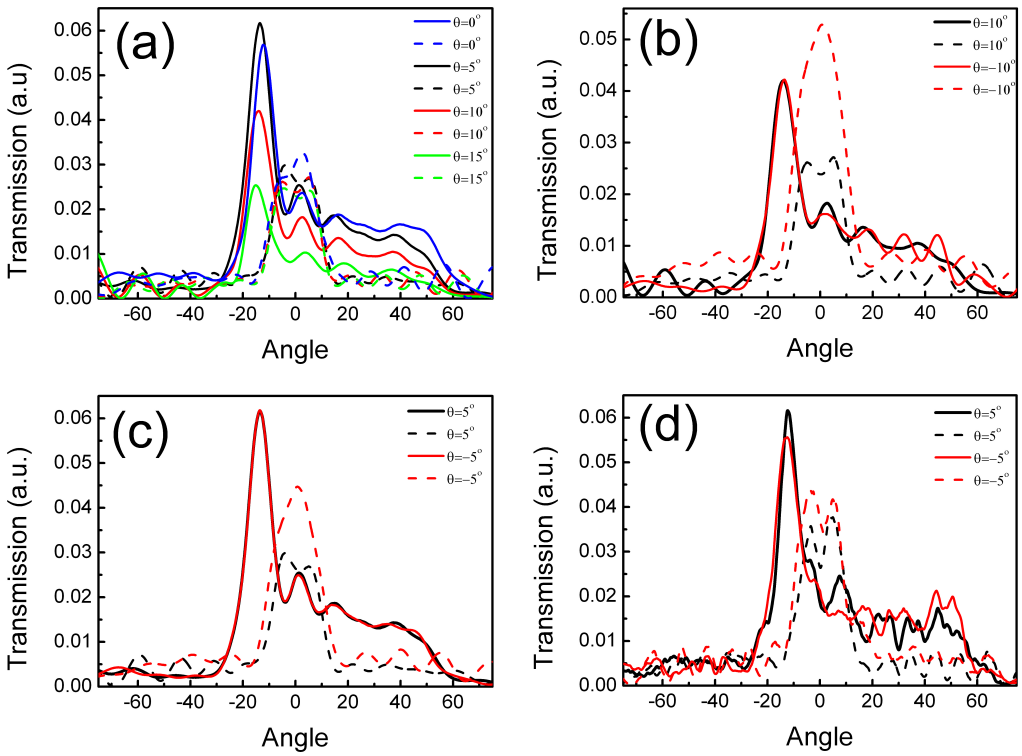

Figure 2.14: Angular distribution of electric field intensity at f=14.5 GHz: (a) for several positive values of θ, simulation; (b) for two values of θ that differ in sign, simulation; (c) same as (b), experiment; (d) same as (b) but for larger $|\theta|$, simulation; front-side (solid lines) and back-side (dashed lines) illuminations.

Here, electric field intensity is approximately six times higher than for the back-side illumination, so that asymmetry in transmission at changing the incidence direction to the opposite one is well pronounced. It is noteworthy that transmission can be rather asymmetric also within other Θ ranges, e.g., at $20^o < \Theta < 50^o$. However, beaming does not occur in this case. In Figure 2.14(c), the experimental angular distribution is presented at f=14.5 GHz for $\theta = 5^o$ and $\theta = -5^o$. Good agreement is observed in the vicinity of $\Theta = -13.5^o$, at the front-side illumination. The effect of changing sign of θ remains in a wide range of θ variation. As an example, Figure 2.14(d) shows the simulated angular distribution of the field intensity at f=14.5 GHz for $\theta = 10^o$ and $\theta = -10^o$. The only difference as compared in Figure 2.14(b) is that the magnitude achieved in the beaming regime at the back-side illumination can be larger than that at the front-side illumination in the vicinity of $\Theta = 0^o$.

Collection of the outgoing radiation has been observed in the one-way beaming regime also when several wide beams with different frequencies are incident at the same θ. This is possibly due to the resonance being rather wide, as seen in Figure 2.9 and Figure 2.10. An example of the angular distribution of the transmission intensity is presented at three values of f in Figure 2.15 (a) and (b) for $\theta = 5^o$ and $\theta = 10^o$, respectively. At the front-side illumination, there is a slight change in the transmission intensity, while the angle at which the maximum is observed remains nearly the same, at least if f is varied from 14 to 15 GHz. Therefore, *multiplexing* is realized here. At the back-side illumination, it appears in the vicinity of $\Theta = 0^o$, while neither a peak-type angular dependence of the resulting beam nor a one-way character of the transmission remain. The dependences on Θ show the same basic features at $f = const$ and $\theta = const$. In contrast to the similar regime observed in Figure 2.9 in [45], we demonstrate that it appears in a one-way manner. The observed features enable one to expect that the one-way feature in the collection of the outgoing radiation can also occur for electromagnetic waves (wide beams) with a rather wide frequency spectrum that are incident at different angles.

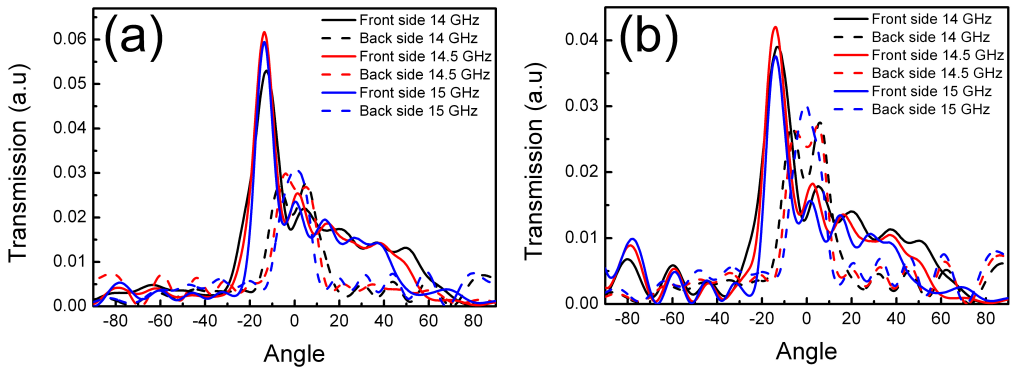

Figure 2.15: Calculated angular distribution of the electric field intensity at (a) $\theta = 5^o$ and (b) $\theta = 10^o$ for three frequency values, at front-side (solid lines) and back-side (dashed lines) illuminations.

2.4 One-way diode like beaming with symmetric gratings and metamaterial based polarization rotator

2.4.1 Design

We utilize the chiral metamaterial based ultrathin 90^o polarization rotator. It exhibits the unity transmission of the circularly polarized eigenwaves with a phase difference of π. The polarization rotator consists of three layers. A unit cell of each of the two resonant layers is composed of four mutually rotated U-shaped split ring resonators. The third layer, a subwavelength mesh that exhibits a negative effective permittivity, is placed between the resonant layers and allows for the obtaining of unity transmission due to the electromagnetic tunneling effect [50, 51]. The two-dimensional metallic grating is assumed to have the same corrugations at front- and back-side interfaces and a single subwavelength slit at the center. Figure 2.16 shows the grating geometry, a unit cell of one of the two resonant layers of the polarization rotator and the experiment setup. The utilized geometrical parameters for the grating are the following: a = 400 mm, b = 500 mm, w = 16 mm, p = 32 mm, h = 8 mm, and g = 18 mm. The width and the

length of the slit are given as 4 mm and 16 mm, respectively. For the front layer of the polarization rotator, which is depicted in Figure 2.16, we take t = 0.7 mm, f = 6 mm, r = 2 mm, and u = 16 mm. The back layer is obtained by rotating the individual split-ring resonators of the front layer by 90^o and as a result, a chiral structure with fourfold rotational symmetry is obtained. A subwavelength mesh that exhibits negative effective permittivity throughout a wide frequency range is sandwiched between the front and the back layers.

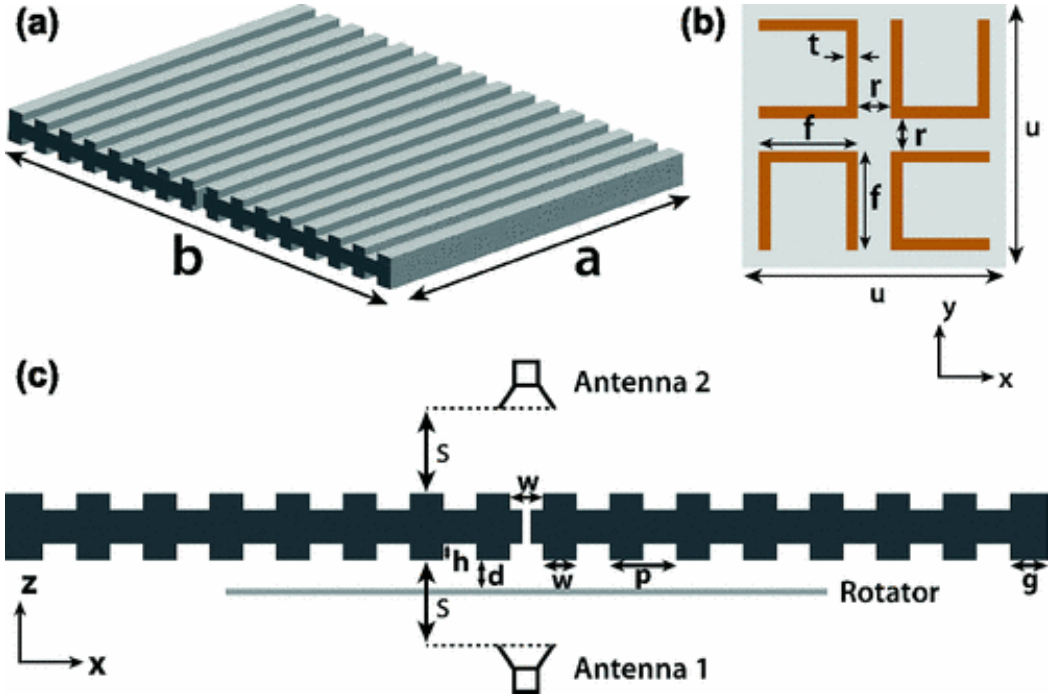

Figure 2.16: (a) Schematic of the metallic grating with a subwavelength slit, (b) front layer of the polarization rotator, and (c) schematic of the experimental setup.

2.4.2 Results and Discussion

The structures are positioned symmetrically between two horn antennas. The transmission coefficient measurements were performed by using an Anritsu 37369A network analyzer. For the purposes of the experimental study, we used the polarization rotator with the dimension of 18 x 18 unit cells. In Figure 2.17, we provide the magnitudes of the experimental linear transmission coefficients for

the polarization rotator, namely $|T_{pp}|$ (co-polarized component) and $|T_{sp}|$ (cross-polarized component). According to Figure 2.17, $f_{PR} = 6.98\ GHz$. The structure exhibits a cross-polarization conversion efficiency of 98 % at this frequency.

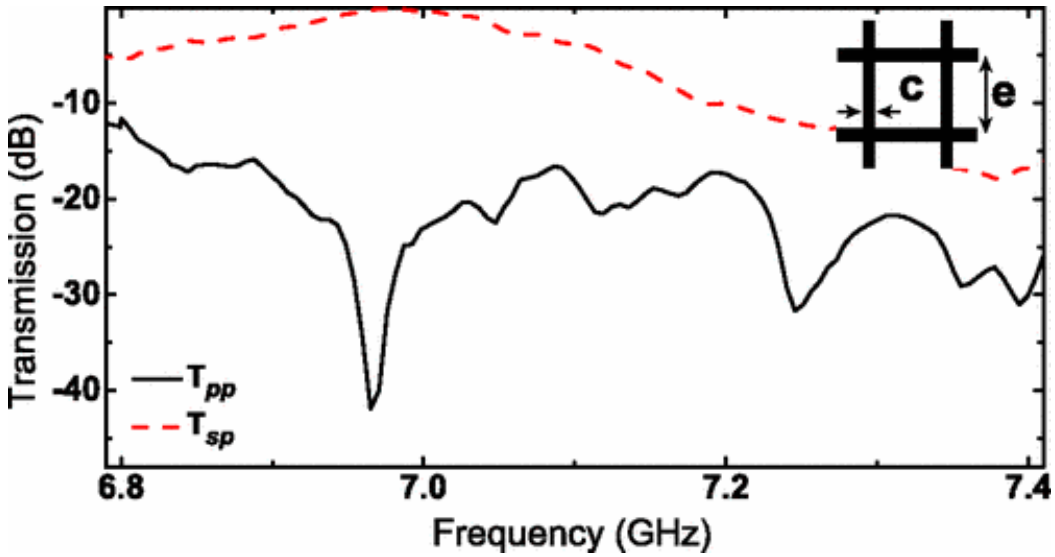

Figure 2.17: Magnitudes of the experimental linear transmission coefficients for the polarization rotator. The maximum of $|T_{sp}|$ is observed at 6.98 GHz. The inset shows the geometry of the subwavelength mesh sandwiched between the front and back layers of the rotator.

In the next step, the metallic grating that contains a single subwavelength slit has been characterized experimentally. Figure 2.18 presents the linear co-polarized transmission coefficients, T_{pp} and T_{ss}. The cross-polarization transmission coefficients, T_{sp} and T_{ps}, are zero due to the lack of optical activity and, thus, are not shown. At the chosen operation frequency, $f = f_{PR} = 6.98\ GHz$, $|T_{pp}| = -3.5\ dB$. On the other hand, $|T_{ss}| < -30\ dB$ throughout the frequency range of the measurement, so that the extinction ratio is better than 25 dB in the vicinity of 7 GHz.

We provide the spatial intensity distributions inside the simulation domain, for the same cases shown in Figure 2.19 for the purpose of stressing the observed beaming effect. Figure 2.19(a)(c) show the intensity distribution of p-polarized outgoing waves for p-polarized incidence for only grating, p-polarized outgoing

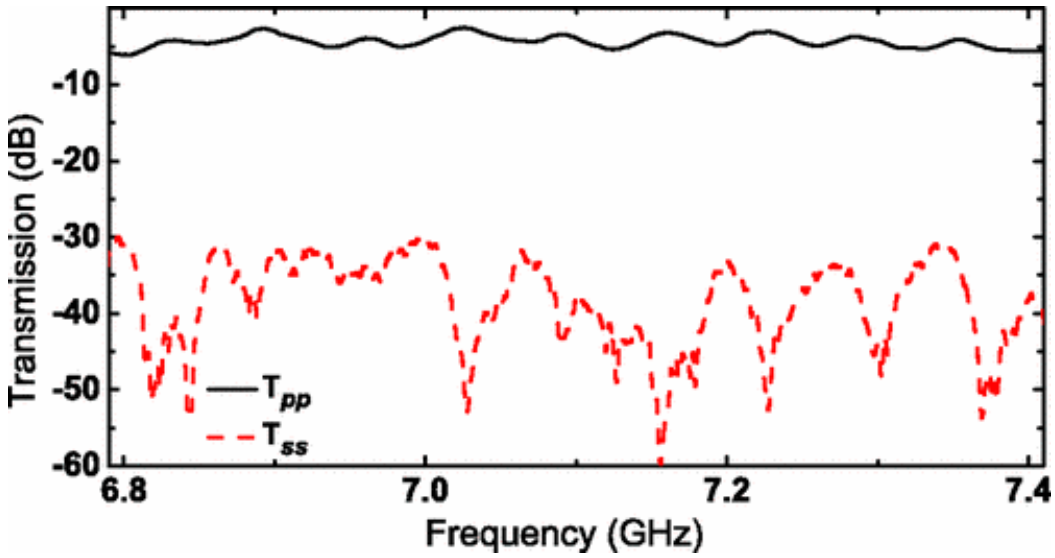

Figure 2.18: Magnitudes of the experimental linear co-polarized transmission coefficients of the metallic grating with a single subwavelength slit.

waves for s-polarized incidence for the forward propagation, and s-polarized outgoing waves for p-polarized incidence for the backward propagation cases, respectively. In Figure 2.19, the intensity distributions for the following cases are not shown since the transmission is found to be negligibly small: (i) s-polarized incidence for only grating, (ii) p-polarized incidence for the forward propagation, and (iii) s-polarized incidence for the backward propagation. The existence of low transmission for these cases is going to be verified by using the experimental results in the next section. If a cross-polarized wave is transmitted at s-polarized incidence for forward propagation and p-polarized incidence for backward propagation, the transmission occurs in the beaming regime, i.e., the transmitted beam is localized within desired angular regions of the exit half-space.

2.5 Conclusion

To summarize, we studied the unidirectional beaming through a subwavelength aperture in non-symmetric metallic gratings at microwave frequencies. The role of the surface plasmon resonance at the output interface in the appearance of

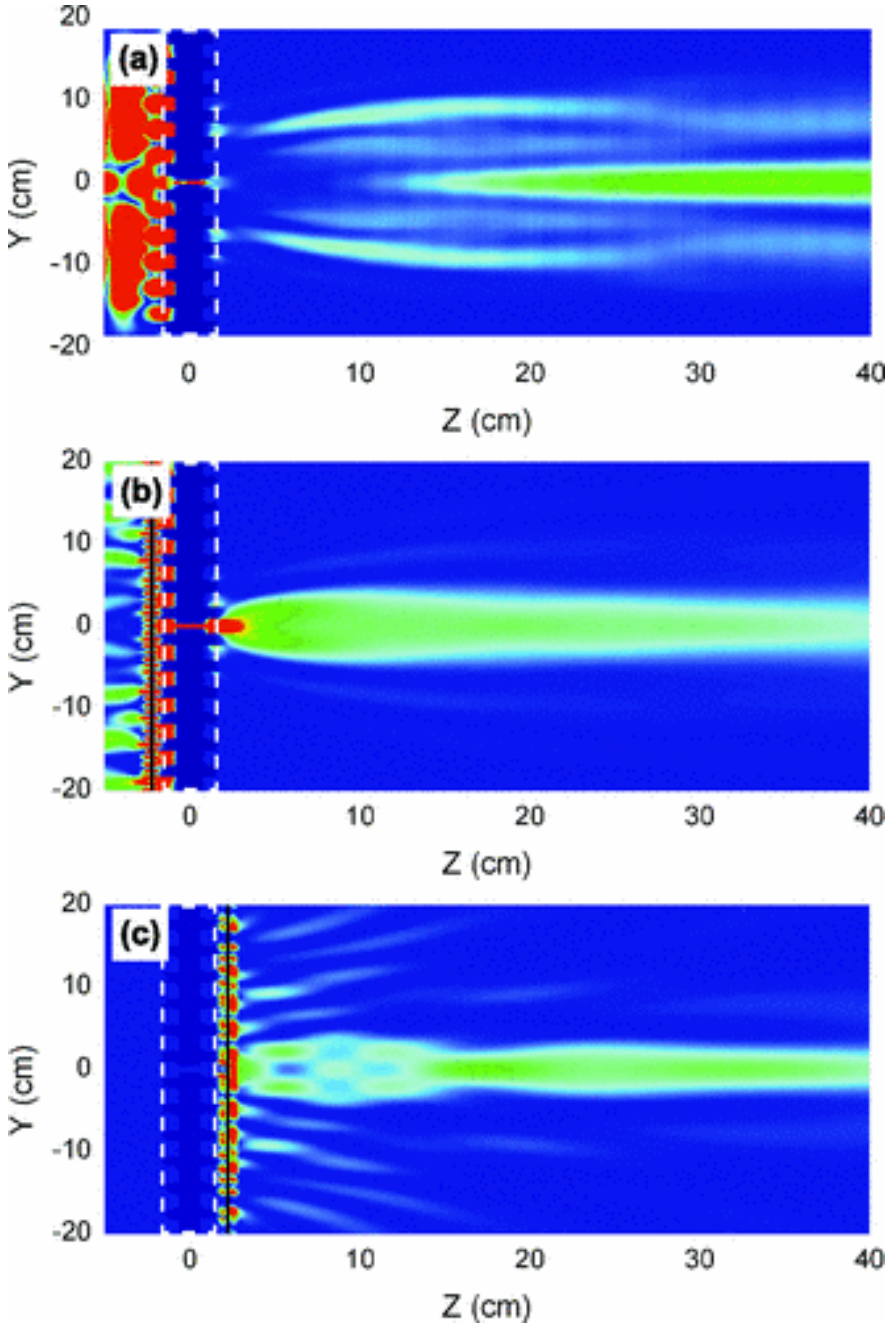

Figure 2.19: Field intensity distributions of p-polarized components for (a) the only grating for p-polarized incidence, (b) the composite structure for s-polarized forward propagating waves, and (c) field intensity distribution of the s-polarized component for p-polarized backward propagating waves. The grating with a subwavelength slit is enclosed in a dashed white rectangle and the position of the rotator is shown by a black line.

the strong directional selectivity is demonstrated theoretically and experimentally. The transmission characteristics can strongly differ because the output surface is only responsible for the spatial distribution of the transmitted field. The presented experimental results are such first results that validate the studied mechanism of unidirectional beaming. It is expected that the suggested mechanism can be implemented for a wide frequency range, including when frequency dispersion of metal cannot be neglected. In particular, for the structures with an asymmetric exit interface, a one-way transmission has been obtained due to the single, off-axis, forward transmitted beam, i.e., the backward transmission is rather weak within a limited range of the observation angle variation. Transmission maps plotted on the frequency-observation-angle plane for the incidence angles, which differ in sign only, are very similar, provided that the input interface is symmetric with respect to the slit. In this case, contributions of the corresponding incident wide beams into the narrow outgoing beam can show the same magnitude at and around the transmission maximum. For the structures with the exit interface being asymmetric with respect to the slit, one-way multiplexing can also occur in the single-beam off-axis regime. For the structures with a symmetric exit interface, the two resulting off-axis beams, or a single on-axis beam appear in a one-way regime a wide range of the observation angle variation. As a result, one-way, dual-band collimation can be obtained. The proposed structures can be utilized to collect contributions from different waves/sources, e.g., in sensing applications. The obtained results promise that a diode-like device can be designed after a proper optimization, opening a route to a new class of unidirectional devices which operate in the beaming regime.

Chapter 3

Surface Enhanced Raman Spectroscopy Substrate based on Plasmonic Structures

3.1 Introduction

The investigation of the use of optical properties (scattering and absorption) of noble metal nanostructures has been investigated by several groups [52, 53]. The study of interactions of molecules or molecular structures with plasmonic nanostructures is another rapidly growing research area having significant impact on several applications such as surface-enhanced Raman spectroscopy, nanoscale optical spectroscopy and surface plasmon resonance spectroscopy [7, 54]. Depending on the noble metal structure used, the surface plasmons can be classified into two groups. The surface plasmon polaritons (SPPs) occur on smooth thin films with thicknesses in the range of 10-200 nm of noble metals such as silver and gold. The localized surface plasmons (LSPR) are excited on isolated nanostructures such as nanoparticles or lithographically prepared nanostructures [7, 55]. The properties of surface plasmons depend on the thickness of metal film, type of the metal and roughness of the metal surfaces and dielectric constant of the adjacent medium.

When a Raman active molecule is subject to intensified electromagnetic fields (surface plasmons), the magnitude of the induced dipole moment increases. Thus, the intensity of Raman scattering obtained from the active molecule increases [8]. This phenomenon is known as surface-enhanced Raman scattering (SERS) and has emerged as a powerful technique used for detection, identification and characterization. Surface enhanced Raman scattering (SERS) overcomes the inefficiency of Raman scattering and provides highly resolved vibrational information of the adsorbed target molecules on metallic surfaces roughened by various methods. SERS is a type of spectroscopy that provides vibrational information about the Raman-active analyte molecules adsorbed on roughened metallic surfaces. There are two fundamental mechanisms responsible for the enhanced Raman signal, which are electromagnetic [56, 57], and chemical enhancement mechanisms [8, 58]. The chemical mechanism, which results from the chemical binding of the analyte molecules to the surface, is rather weak, when compared to the electromagnetic mechanism which is the dominant one. SERS benefits from the increased electric field due to the localized plasmons on the nanostructured metallic surfaces. Controlling the SERS signal via patterned metallic nanostructures and arrays has been an attractive research area over the last years. There are several examples, where the nanostructures with different geometries, shapes and sizes have been used as SERS substrates [59–62]. As a rule of thumb, an optimal substrate should provide the highest possible average field enhancement at the metal molecule interface.

Since the electromagnetic enhancement through the surface plasmons is the major contributing to the SERS enhancement mechanism, the construction of plasmonic structures for the optimization and manipulation of the surface plasmons is the focal point for the preparation of optimally performing SERS substrates [34]. The electromagnetic mechanism of SERS predicts the SERS enhancement factor, which is determined by the fourth power of the field enhancement in the local optical fields of metal surfaces [35]. The nano-scale surface roughnesses serve for the electromagnetic enhancement mechanism via propagating and/or localized surface plasmons they support. Designing efficient SERS substrates has attracted interest since the discovery of the phenomena. The studies

were accelerated after the exploration that specifically designed nano roughnesses overcome the unpredictable and irreproducible nature of SERS while increasing the signal intensity [36]. Methods such as oxidation-reduction cycling, metal island or cold deposited films, colloids are nowadays being compared and replaced with lithographic methods that end up with desired shape, size and arrangement. Nanostructured periodic arrays [36-39], concentric arcs [40], concentric rings [41] are only some of the work done in this area.

3.2 Circular plasmonics lenses with a single ring

In this study, circular plasmonic lens with different ring diameter and slit width were prepared by electron beam lithography (EBL) and the influence of plasmonic lens structure on SERS enhancement was investigated using self assembled p-ATP molecules on the plasmonic lenses. The SERS enhancement performance of the lenses was evaluated by comparing the enhancement between planar silver thin film and circular plasmonic lenses [63].

Incident electromagnetic field can be enhanced and localized in the slit region of a metal film [64]. This localized field couples surface plasmons on the surface of the metal. Surface plasmon polaritons propagate along the metal surface. Propagation length of surface plasmon polaritons can be expressed by Equation 3.1 [65]

$$d_{SPP} = \lambda_0 \frac{(\epsilon_m^{'})^2}{2\pi\epsilon_m^{''}} \left(\frac{\epsilon_m^{'} + \epsilon_d}{\epsilon_m^{'}\epsilon_d}\right) \tag{3.1}$$

where λ_0 is the wavelength of free space, $\epsilon_m^{'}$ and $\epsilon_m^{''}$, are real and imaginary parts of relative permittivity, respectively, and ϵ_d is the permittivity of dielectric medium. Surface plasmon polaritons focus at the center of the circle and create standing waves for the case of a circular slit structure, thus they can operate such as a plasmonic lens [66]. It was also shown that field enhancement and focusing of surface plasmon polaritons at the center is possible by circular slits into a silver

film [67]. Dependence of the circle diameter to the enhancement at the center was reported to be increasing almost linearly with radius r for the cases, where the propagation length of surface plasmon polaritons is much smaller than the radius of the ring [66].

3.2.1 Design and Fabrication

Circular slit structures were fabricated by using electron beam lithography. First, samples were spin coated by positive-tone electron beam resist. Then, a circular area, excluding the slit region, was exposed with Raith electron beam lithography system. 100 nm thick silver was deposited on the samples by electron beam evaporation. After the standard lift-off process, ring-shaped holes with different width and radii were obtained, as shown in Figure 3.1. The results obtained from the unpatterned part of the metal were compared to the ones obtained from the slit structures in order to calculate the SERS enhancement.

3.2.2 Preparation of self-assembled monolayer Raman active molecules on plasmonic lenses

4- aminothiophenol (p-ATP) is used to study the SERS enhancement property of the prepared lenses. Since this molecule has a free thiol (-SH) group, it forms a quite uniform monolayer, which is called self-assembled monolayer (SAM), on the metal surfaces [68]. Therefore, the prepared plasmonic lens samples were rinsed in Ethanolic solution of 4- aminothiophenol (p-ATP) (1 mM) for 2 hours in order to form an SAM. Then, the surface was cleaned with ethanol to remove the unwanted adsorbed molecules from the surface.

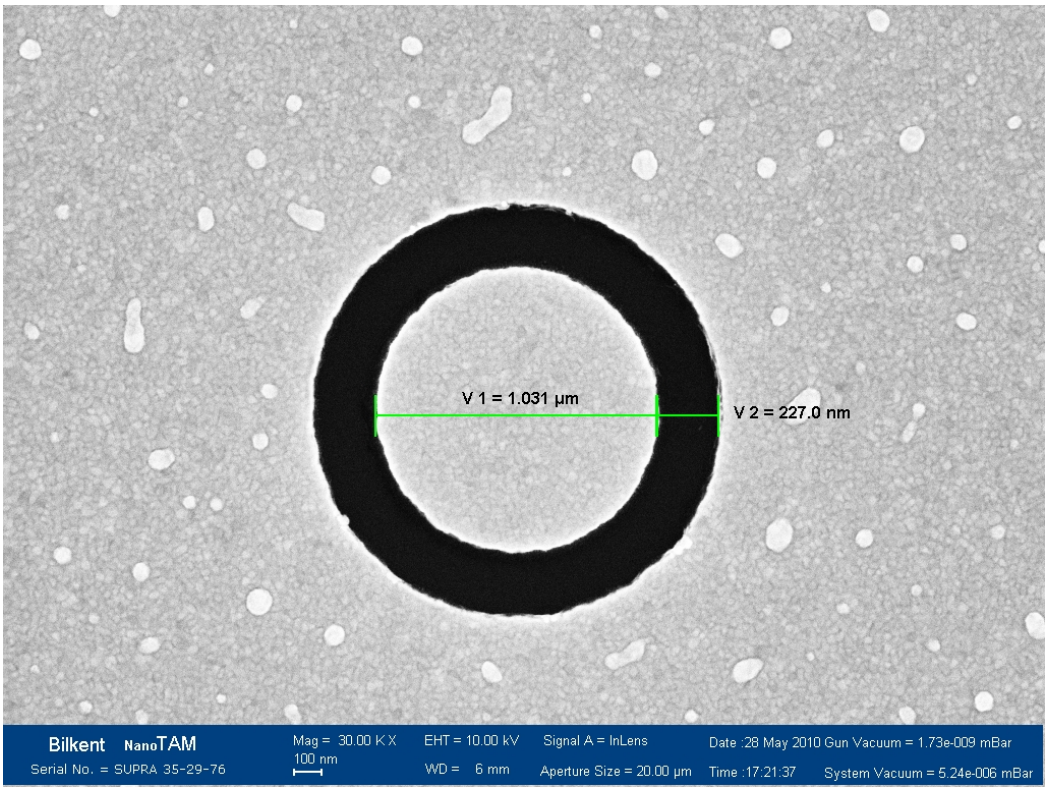

Figure 3.1: Scanning electron microscopy image of ring-shaped hole on silver film.

3.2.3 Results and Discussions

All of the Raman measurements are performed using a completely automated Renishaw InVia Reflex Raman Microscopy System equipped with an 830-nm diode and 514-nm argon-ion lasers. A laser with a wavelength of 514 nm is used to excite the surface plasmons on the silver plasmonic lenses. A 50x microscope objective is used to focus the laser beam to obtain SERS spectra from the self assembled ATP molecules on the plasmonic lenses.

The enhancement factor obtained in SERS experiments is the fourth power of electromagnetic field of surface plasmons generated on the nanostructure surfaces [69]. This means that the SERS enhancement is increased, when the intensity of the surface plasmons is higher. Plasmonic lenses have capability of focusing the surface plasmon depending on their structural properties such as shape and size [66, 67]. Although the near-field optical microscopy (NSOM) has generally been used for the optical characterization of the plasmonic lenses, Raman spectroscopy can also be used for the optical characterization and evaluation of plasmonic lenses. In this study, p-ATP is self-assembled on the silver plasmonic lenses as a Raman active molecule in order to compare the SERS performances depending on their ring diameters and slit widths. An average of ten SERS spectra measurements are taken into account for each lens for the sake of comparison. The SERS spectra are obtained by focusing the laser light on the center of the plasmonic lenses with a 50X objective. All of the experiments are carried out with a 50X objective and 514-nm laser with the same laser power, 25 mW.

The number of the Raman active molecules is assumed to be the same all over the surface, since p-ATP forms a self-assembled monolayer (SAM) on the silver surfaces. The SERS spectrum obtained from the p-ATP molecules on plasmonic lens is more intense than the regular thin silver film, as shown in Figure 3.2. This can be explained with the plasmon focusing ability of the lenses. The most intense peak at 1435 cm^{-1} on the SERS spectra is chosen to make the comparisons in this study. The intensity of chosen peak is 3.8 times higher on plasmonic lens than that of the thin silver film.

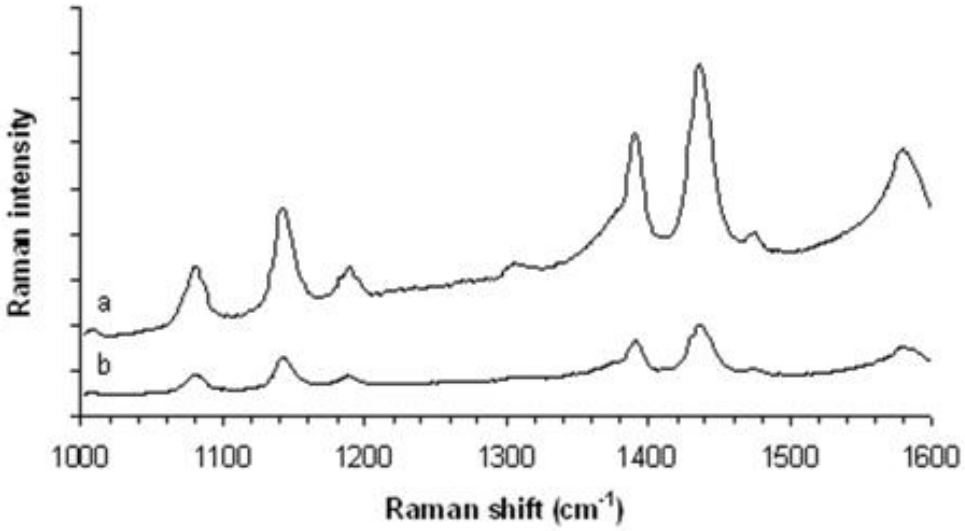

Figure 3.2: SERS spectra of p-ATP obtained from (a) plasmonic lens, and (b)thin silver film.

The influence of the slit width on SERS activity is investigated. As the diameter of the rings is kept constant at 2 m, the slit width is varied. Figure 3.3 shows the SERS spectra obtained on the structures with the increasing slit with. As the slit width increases, the intensity of the SERS spectra decreases.

Figure 3.4 shows the graph of the I_{lens}/I_{film} ratio for the lens with 3 m diameter with increasing slit width as an example. The ratio of intensity is decreasing with plasmonic lens having larger slit width. All ring-shaped lenses with different diameters show that the 200 nm slit width is the optimal. The intensity I at the center of the ring is expressed with the Equation 3.2[70]:

$$I = CI_0 \frac{2R}{\lambda_{SP}} \exp(-\frac{R}{2d_{SPP}}) \tag{3.2}$$

Next, the influence of the inner ring diameter on SERS is investigated using plasmonic lenses with a 200-nm slit width. The SERS spectra obtained from the plasmonic lenses having ring diameters of 0.5, 1.0, 2.0, 3.0, 4.0 μm are demonstrated in Figure 3.5. Figure 3.6 shows the change of the I_{lens}/I_{film} ratio with

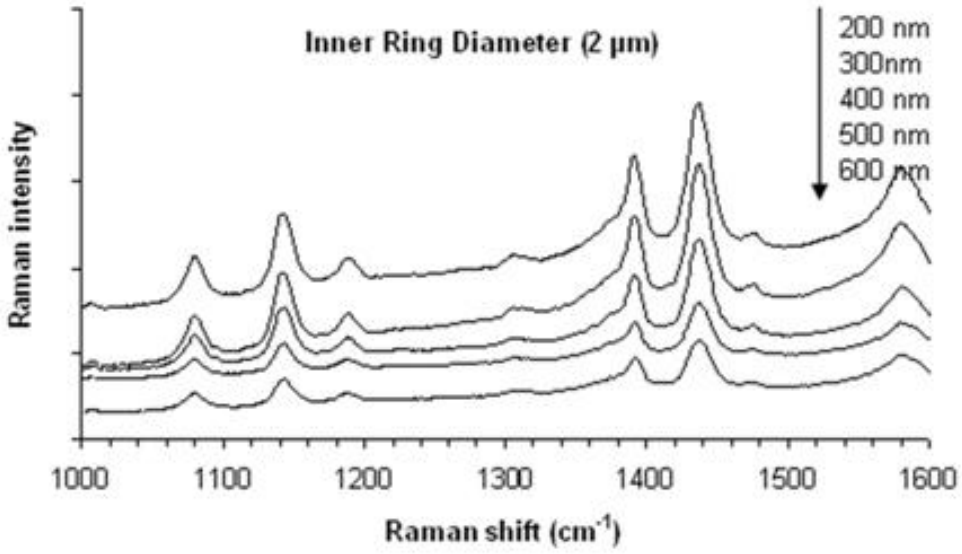

Figure 3.3: SERS spectra obtained from plasmonics lenses with different slit widths.

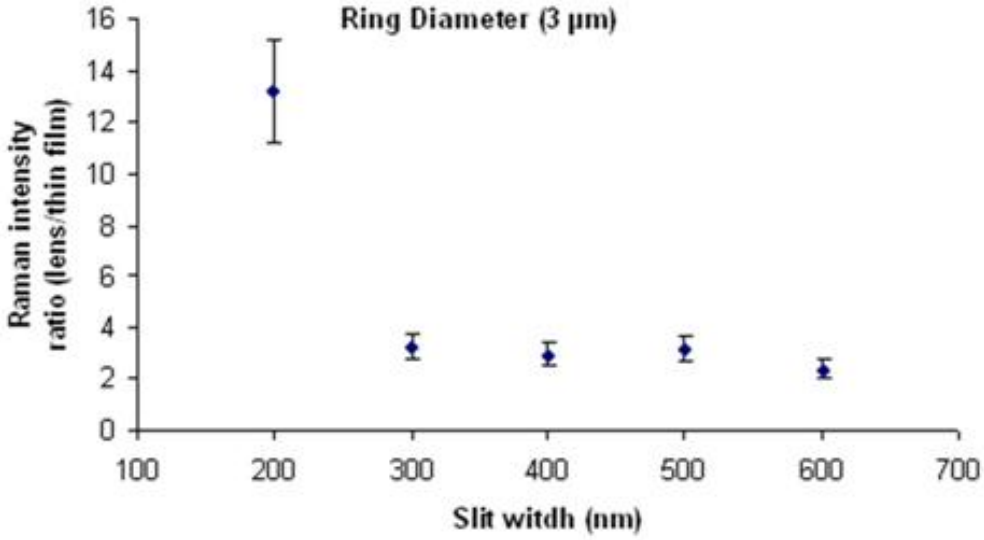

Figure 3.4: SERS intensity ratio depending on slit width.

the increasing diameter. The SERS intensity obtained from the plasmonic lens is 13.2 times higher compared to the thin silver film.

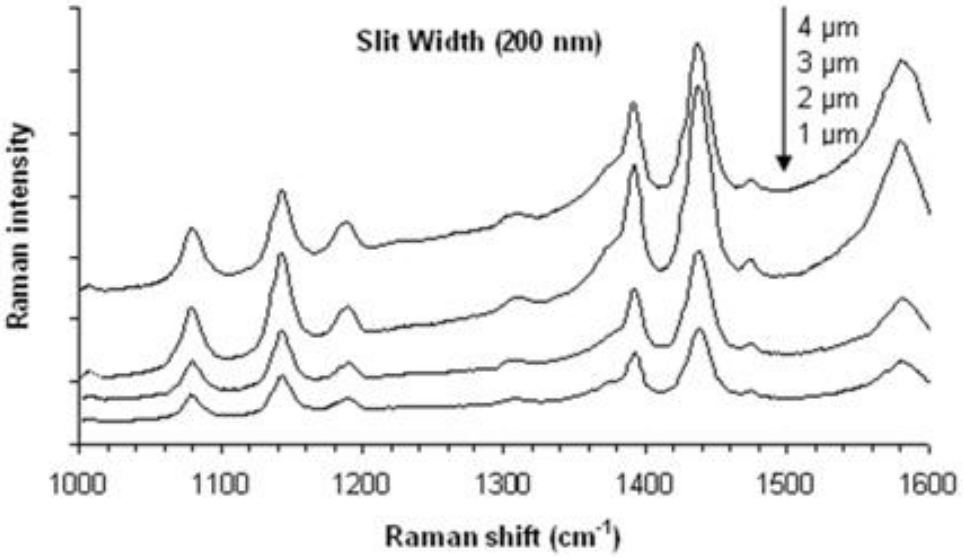

Figure 3.5: SERS spectra obtained from plasmonic lenses having the same slit width and different ring diameters.

Figure 3.7 illustrates the FDTD simulation result for the case, where the diameter of the ring is 3 μm and the slit width is 200 nm. The electric field is localized inside the slit region as seen in the figure. The reason of this localization is that the electromagnetic wave is enhanced due to the slits, which are smaller than the wavelength of the incident light [71]. The simulations are carried out by using TM polarized Gaussian beam. The electric field distribution on the surface of the structure is monitored. It is also seen that the field is focused in the center of the circle. We integrated the square of the electric field intensity on the surface for both patterned and unpatterned metal, and took the ratio of the integrations for the comparison. The fourth power of electric field ratio was calculated and found as 12.9. The FDTD simulation results also demonstrate that when the inner ring diameter is increased with a constant slit width, the electric-field intensity on plasmonic lenses increases. As the diameter of the ring increases, the area of the slit region increases, as well. This provides focusing of the excited surface plasmon polaritons towards the center more intensively. The results can also be explained by Equation 3.2. In this case, C is constant, since the slit width is kept constant.

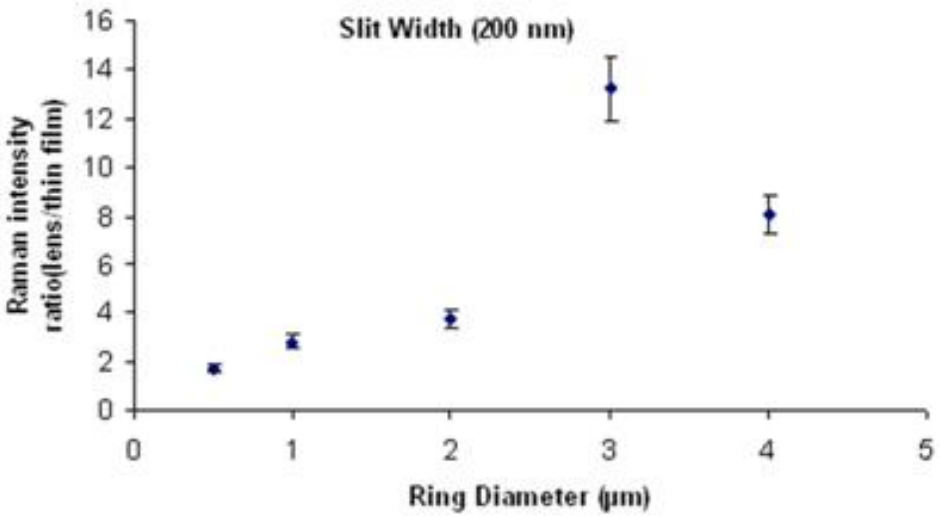

Figure 3.6: SERS intensity ratio depending on changes ring diameter changes.

The intensity at the center should increase monotonically with r up to surface plasmon propagation length d_{SPP} (Equation 3.1). The theoretical calculation is consistent with the experimental result and the literature [70] up to 4.0 μm inner diameter. This is due to the size of the laser spot used for the SERS experiment. The electromagnetic radiation is necessary for the excitation of surface plasmons on the nanostructured metal. When the 50x objective is used, the laser spot size is much smaller than 4.0 m and, therefore, it cannot excite plasmons in the large area. Thus, the ratio of the electric-field intensity decreases.

3.3 SERS enhancement with the concentric ring structures

3.3.1 Design and Fabrication

In this study, two different designs are prepared for the SERS comparison. The first sample is made of circular concentric rings etched from a planar gold film.

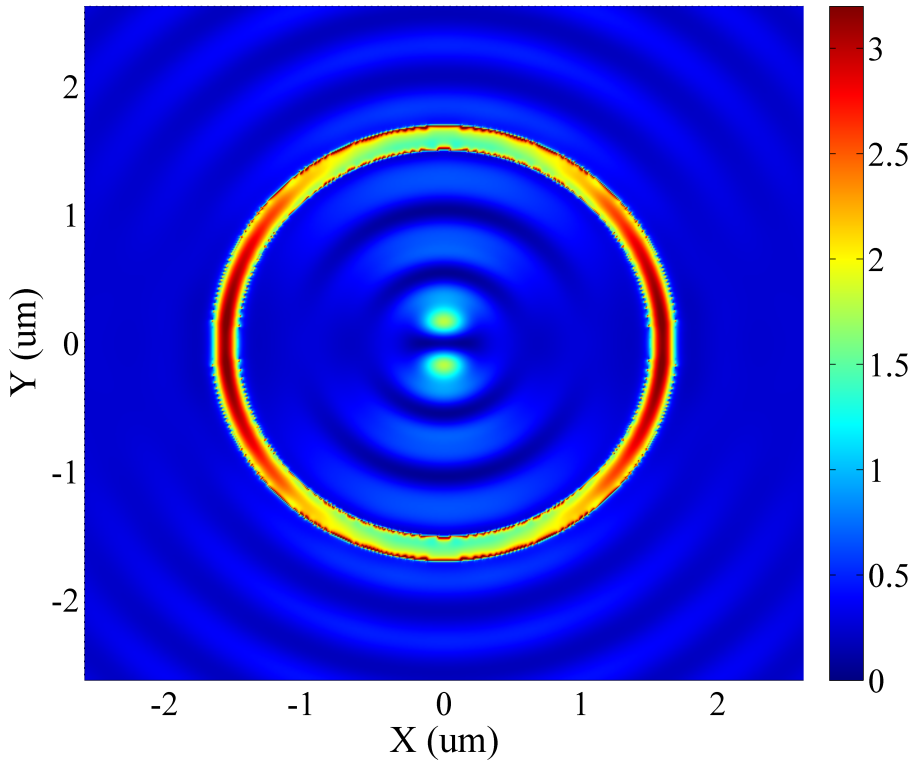

Figure 3.7: Electric field intensity $|E|^2$ distribution on the plasmonic lens.

In the second sample, the etched portions are filled with a dielectric spacer and a second layer of golden rings are deposited only at the top of the dielectric spacer forming a coupled ring structure. The performance of the *coupled ring* samples are compared to those with the *etched ring* samples and plain gold film. The motivation of this study is to show that the proposed design can be used as a SERS substrate with the benefit of the increased electric field intensity due to the coupling of plasmons localized between the rings and the center disk. It is also shown that the design can be tuned physically for better SERS performance.

Sapphire substrate is spin coated with Poly(methylmethacrylate) (PMMA 950 A-2) at 4000 rpm for 40 seconds. After baking for 90 seconds at 180^oC, Hydrogen silsesquioxane (HSQ), a negative tone electron-beam resist, is spin coated at 2000 rpm for 40 seconds. After baking for 90 seconds at 150^oC, aqua-save (polymer) coating is applied to reduce the charging effects. Raith E-Line system is used for lithography. The sample is developed with Tetramethyl ammonium Hydroxide (TMAH) developer for 75 seconds. An O_2 plasma etch is done to remove the parts surrounding the rings lithographed by electron beam exposure. The metal coating is performed with the Leybold Univex 350 Coating System. 5nm Ti adhesion layer and 40 nm Au is coated on the patterned sample which results in rings and gold film seperated by 100 nm thick resist (Figure 3.8 (b)). For the case of etched ring sample, a final lift off step in acetone is included (Figure 3.8 (c)). The fabrication steps are visualized in Figure 3.8 (a) for a 5-ring structure. SEM image of one of the samples is shown in Figure 3.8 (d).

Physically different structures that have varying dimensions are fabricated to optimize the SERS signal intensity. The number of rings for different samples is chosen to be 18, considering that the increased number of rings is expected to increase the resultant E-field intensity [72]. The inner disk diameter changes from 965 nm to 1750 nm. The period of slits vary between 500-860 nm.

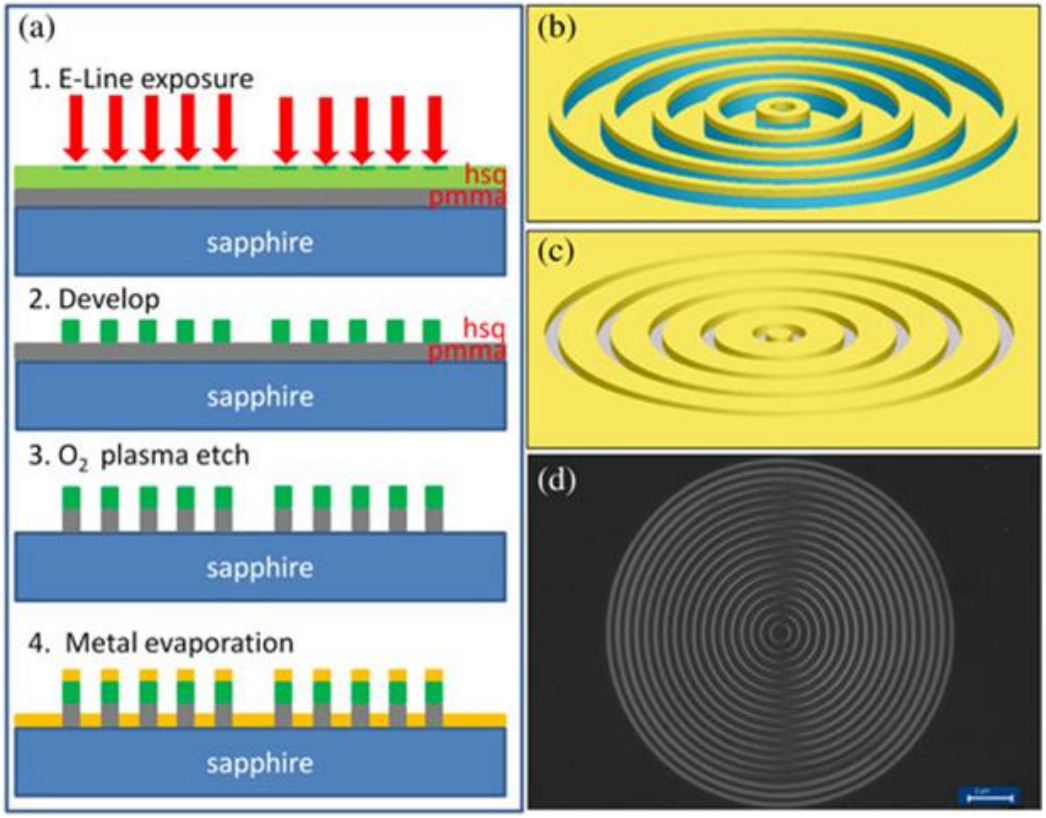

Figure 3.8: (a) Illustration of fabrication steps for a five-ring coupled structure (b) schematic of coupled concentric rings (c) schematic of etched concentric rings (d) SEM image of the coupled structure. Inner ring diameter 965 nm, period 500 nm. The scale bar corresponds to 2 μm.

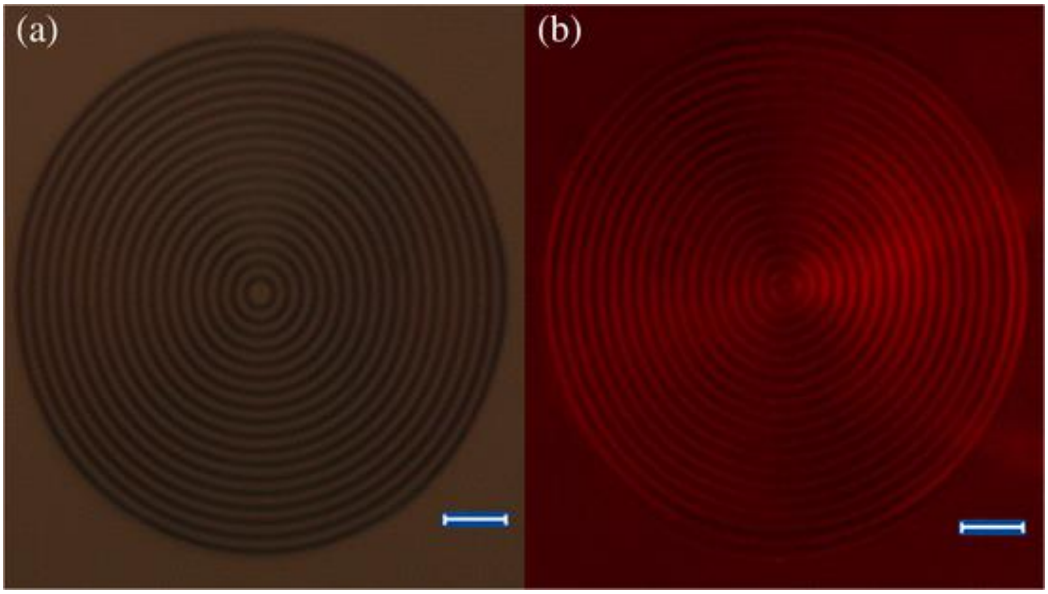

Figure 3.9: Optical microscope image (a) under white light illumination (b) imaging of surface under LED excitation. The scale bar corresponds to 2 μm for both figures.

3.3.2 Imaging surface plasmons

There are several methods to visualize the plasmon fields accompanied by nanostructures. The most convenient method for surface plasmon (SP) imaging is to use near-field optical microscopy [67]. A more practical way is to distribute fluorescing molecules homogeneously close to the metal surface and use optical microscopy [73]. The fluorescing molecules should be positioned at a distance from the metallic surface preferably by a few nanometer thick dielectric layer since the fluorescence of the molecules can diminish in direct contact with the metal. Momentum matching between light and SPs is maintained by the corrugations on the gold surface. A high flux red LED is used for excitation purposes. A Leica optical microscope and its integrated CCD are used to observe and image the surface. The 100x objective with numerical aperture 0.9 is used. The thin dielectric spacer is maintained by the benzenethiol monolayer that was covered for SERS measurements. No other means of dielectric deposition was necessary and no fluorescence quenching effect was observed. Upon this spacer layer a monolayer of Rhodamin 6G molecules were deposited on the surface of the sample by

incubation for 1 hour and post-cleaning several times with deionized water (DI) to remove any residue after incubation. The images obtained in this way, shown in Figure 3.9, represent the SPs qualitatively rather than in a quantitative way [73]. The data presented is in accordance with near field energy density distribution measurements done with NSOM for a plasmonic lens structure made of multiple concentric metallic rings similar to our proposed design [67].

3.3.3 Simulation Results

A commercial software package, Lumerical, which uses finite difference time domain (FDTD) technique is used for the simulations. All the physical boundary conditions are chosen as perfectly matched layer (PML) to avoid undesired reflections. For preserving computational sources 2-ring counterparts of the proposed structures are used for comparison. The physical dimensions of the disk and rings are the same as the fabricated structures except the number of rings. The 5 nm Ti adhesion layer is excluded and 45 nm gold layer is assumed in the simulations considering the 5nm maximum mesh size used in the simulations which saves computation time while preserving accuracy. The material data for sapphire is taken from Palik and Johnson and Christy data is used for gold. The structures are illuminated with a single wavelength plane wave source at 632 nm that matches the laser excitation. 2D cross-sectional monitors are used to visualize the E-field distributions. Coupled structures that provide the best and worst signal intensity (corresponding to the resonant and non-resonant conditions) and etched ring structures are compared.

In accordance with the SERS experiments the coupled structures end up with a higher E-field intensity distribution and hence higher SERS intensity as can be seen in Figure 3.10. In the coupled structure, the upper rings are coupled to the bottom rings which result in the increase of *hot spots* responsible for the SERS enhancement effect. This effect is degraded for the non-resonant version and minimized for the etched-ring structure.

The experimentally obtained enhancement from coupled structures compared

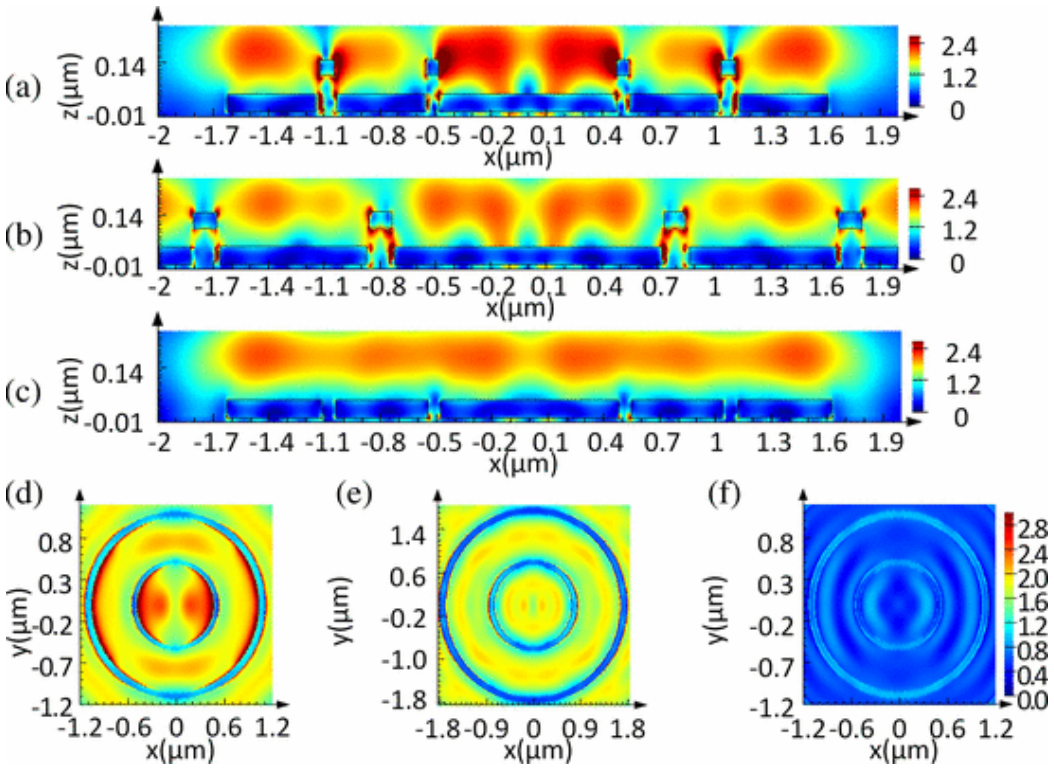

Figure 3.10: Cross-sectional Formula-field distributions $|E|^2$ of the coupled resonant (a, d), coupled nonresonant (b), (e) and etched ring (c), (f) structures, respectively. The same color scale is used for (d), (e) and (f).

to the etched structures is validated by simulations as well. The SERS intensity is considered to be proportional to $|E|^4$ at the laser excitation frequency for this calculation. Electric field distributions obtained through simulations are integrated over the gold surfaces for both designs using 4 μm spot size. The resultant ratio gives $|E|^4_{coupled} \,/\, |E|^4_{etched} \sim 12$ which is close to the experimentally obtained result 8 times larger signal intensity.

3.3.4 Experimental Results and Discussions

The patterned structures are incubated with 100mM benzenethiol in ethanol solution for 2 hours and then thoroughly rinsed with ethanol to ensure a self assembled monolayer (SAM) formation on the surface and to remove residues. The measurements are taken right after coating. The SERS data is collected under excitation with He-Ne laser at 632.8 nm with the Jobin Yvon Horiba system. 100x objective with 0.9 numerical aperture is used throughout the measurements. Same accumulation and exposure times are used for all the patterned samples. For the plain gold sample, accumulation time is multiplied by 4. But no distinguishable signal is observed. The data is presented in stack form for easy visual comparison.

When the nanopatterned structures are compared to the unpatterned plain gold film, characteristic Raman lines of the molecule were invisible, even though 4 times the accumulation time is used for the plain film. Considering the maximum intensity obtained from patterned structures and the minimum detectable intensity throughout the experiment it is derived that patterned structures have 630 times larger SERS intensity when compared with plain gold film.

The number of rings is the same and the slit widths are at close proximity for all the fabricated samples. Therefore the change in signal intensity may be due to the inner ring diameter and the period. The acquired SERS signal intensity from different samples is shown in Figure 3.11. The smallest inner ring diameter sample has the largest signal intensity. One reason for this situation is the increase in the number of rings (and therefore the number of hotspots) that

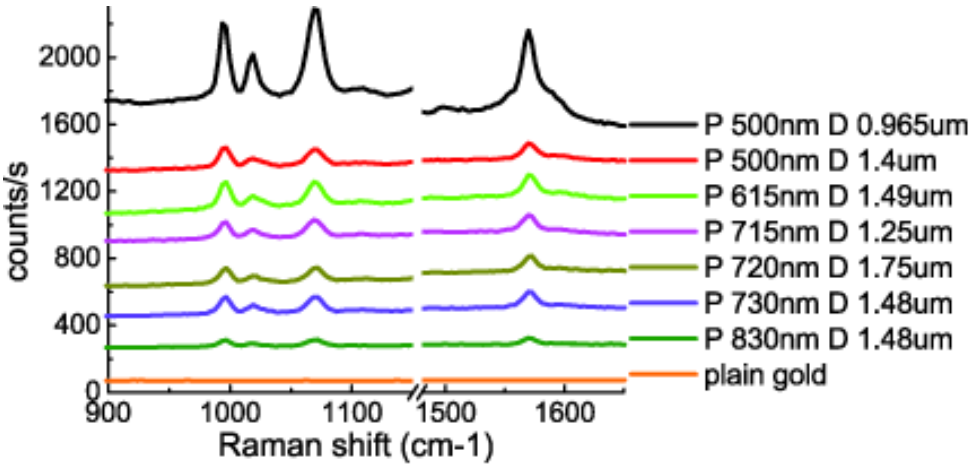

Figure 3.11: SER spectra of Benzenethiol from the *coupled ring* structures and plain gold film. No background correction is done. Spectra are shifted for a better view. A horizontal axis break is applied to save space. In the legend, the letter P denotes period and the letter D denotes diameter.

are included within the laser spot area, as the inner radius decreases. The E-field intensity is considered to be mainly due to the interaction (coupling) of the thinner rings residing on dielectric and thicker rings on sapphire. This coupling can also be visualized from the simulation results presented in Figure 3.10. The period does not seem to have a major impact on the signal for this design. To observe the effect of coupling between upper and lower rings in this fabrication, two structures with and without upper rings having similar physical dimensions are compared. In literature there are various designs that are shown to work as plasmonic lenses similar to this *etched-ring* design [74]. In such a design the period has to be chosen so as to match the surface plasmon wavelength to maximize the focusing and therefore the electric field intensity that dominates the SERS signal intensity [75, 76]. The excitation laser is set to 632.8 nm and plasmon wavelength is calculated as 605 nm. The period of the etched ring structure is slightly longer than this value and sufficient to maximize the focusing. The coupled ring structure that has similar physical dimensions is shown to give 8 times better signal intensity than such an optimal plasmonic lens structure as shown in Figure 3.12.

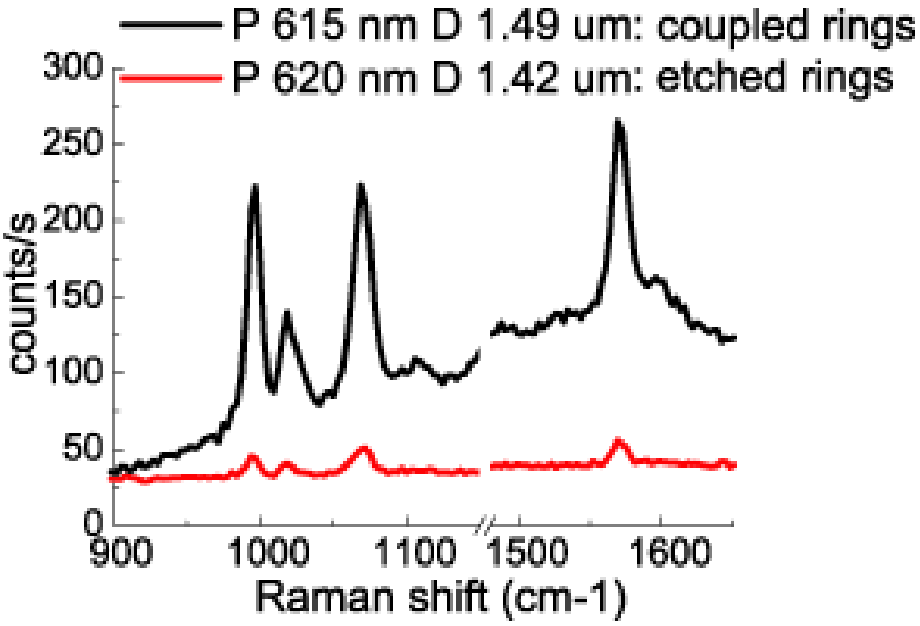

Figure 3.12: SER spectrum of Benzenethiol from the coupled rings and the etched rings. No background correction is done. A horizontal axis break is applied to save space.

Enhancement factor (EF) calculation is beneficial since it provides an objective measurement to compare the performances of different designs. The most common EF definition is $(I_{SERS}/N_{surf})/(I_{RS}/N_{vol})$ [77–79]. Here, I_{SERS} and (I_{RS} are the SERS and Raman signal intensities; N_{surf} and N_{vol} are the number of molecules probed for SERS and the Raman experiments, respectively. The strongest band in the spectra at 1075 cm^{-1} is employed for the EF calculation.

A thin glass container with neat Benzenethiol is used in the Raman experiment where the detection volume is approximated as a cylinder of height that equals the thickness of neat benzenethiol following the same steps and reasoning as in [80, 81]. N_{vol} is determined from $N_{vol} = N\rho hA/M$ where N is the Avogadros number, ρ is the volume density (1.073 g/cm^3) and M is the molar mass (110.18 g/mol) of the benzenethiol molecules. h is the thickness of the neat benzenethiol sample and A is the spot area. N_{surf} is defined as $N_{surf} = \rho_s A$, where ρ_s is the surface packing density ($6.8x10^{14}1/cm^2$), A is the total exposed gold area [81]. The exposed gold surface area of the structures is calculated by taking into account

the lateral and top surfaces of the rings and the disk. A perfectly ordered self-assembled monolayer is assumed on the exposed surfaces in order to calculate the maximum possible N_{surf} [78, 82, 83]. The calculated EF, as described above, is $1.67x10^7$ for the coupled-concentric structures which is well beyond this value. It still has room for improvement through tuning the physical dimensions of the structures.

3.4 Fractal bowtie nanoantennas

Optical bowtie antennas, which consist of two triangles separated by a gap, have been studied among many researchers over the years. Surface plasmon currents are excited on these nanoantennas and the induced charges are shared by the triangles that are capacitively coupled via the gap. In principle, they are similar to dipole antennas; however, they can operate for larger bandwidths compared to dipole antennas. This property provides flexibility in terms of the operation wavelength along with their scalable nature.Furthermore, the triangular features allow the excitation of higher order modes and the corners of the triangles generate lightning-rod effects that result in stronger field enhancement. Bowtie antennas can be used in several applications such as the enhancement of single-molecule fluorescence [84], single-particle trapping [85], measurement of optical intensity enhancements [86], integrated apertures for near-field optical imaging [87], tunable graphene nanophotonics devices [88], and Surface-enhanced Raman spectroscopy (SERS) owing to the strong electromagnetic field localization and enhancement [89]. It has been also shown that the bowtie antennas can be used as efficient SERS substrates [90].

A fractal is a geometric shape which shows self-similar patterns [91]. Fractals present multiperiodic structures that open up new operational bands in RF. Researchers have extensively studied fractal antennas to achieve improved performance by addressing the lacunarity, changing the fractal similarity dimensions (D_s), antenna sizes and feed locations. Fractal geometries have been used in

applications such as miniaturized antennas [92], frequency-selective metamaterials [93], and multiband mobile telecommunication devices [94]. It was theoretically shown that the fractal plasmonic antennas are advantageous in order to achieve controlled broadband spectral response [95]. Another theoretical study pointed out that by designing plasmonic bowtie antennas by employing fractal geometry, it is possible to enhance the electric field within the gap, tune the spectral response at near-infrared wavelength regime, and red-shift the resonance wavelength after each iteration [96].

In the current work, we have demonstrated both experimentally and numerically that the fractal bowtie nanoantennas operate at longer wavelengths after each fractalization, compared to the conventional bowtie antennas of the same size. Moreover, they can further enhance the SERS efficiency due to electric field enhancement. Both the simulations and measurement results depict that as the degree of fractals are increased the SER signal intensity increase, as well.

3.4.1 Design and Fabrication

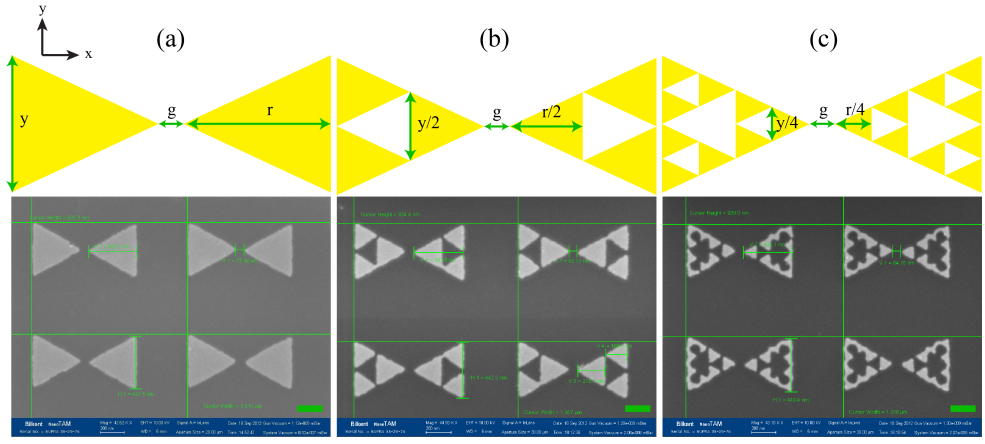

Figure 3.13: Schematics (above) and SEM (below) images of (a) Bowtie, (b) Fractal-1, and (c) Fractal-2 structures. $g = 65nm$, $r = 400nm$, $y = 420nm$. Scale bar is 100 nm.

Fractals are constructed by recursively using an operator on a basis shape. When the basis shape is a triangle, the resultant fractal is named a Sierpinski

gasket (or Pascals triangle modulo 2), and two tip to tip oriented equilateral Sierpinski triangles form a modified bowtie antenna. In this study, Fractal-1 is constructed by subtracting inverted triangles from the main bowtie antenna. The three equal triangles remaining on the structure after the subtraction are half the size of the original one. Fractal-2 is constructed by iterating the same procedure on the remaining triangles one more time. Schematics of the proposed structures are demonstrated in Figure 3.13.

For the fabrication of the antennas, 300 μm thick double-side polished sapphire substrate is cleaned and spin coated by 90 nm thick 950K A2 Poly(methylmethacrylate) PMMA, which is a positive-tone electron beam lithography resist. A water-soluble, conductive polymer called aquasave is spun on in order to prevent electrostatic charging. Raith E-line Plus electron beam lithography system is used for the exposure. The PMMA is exposed at 15 keV accelerating voltage using 10 μm aperture size. After the exposure, the sample is developed with 1:3 MIBK:IPA solution for 40 seconds. Then, 5 nm titanium, as an adhesion layer, and 35 nm gold are deposited by using Leybold electron beam evaporator, followed by the standard lift-off process.

After fabrication, the physical dimensions and gap sizes of the resultant samples are measured by SEM. The gap size, height and base of the triangles are denoted by g, r and y, respectively in Figure 3.13 where their dimensions are listed as $g = 65nm$, $r = 400nm$, $y = 420nm$. The total length of one anntenna in x-direction for all three structures is $g + 2r = 865nm$, the size of the gap between the main triangles is $g = 65nm$, the periodicity in the x-direction is 1.3 μm, and the periodicity in the y-direction is 930 nm. The dimensions are indicated in Figure 3.13 for all the three shapes along with the SEM images of the antenna arrays.

3.4.2 Measurements and Simulations

Transmission measurements are carried out using Vertex 70V FTIR Spectrometer with Hyperion 2000 IR Microscope. The sample is illuminated normally by a near-infrared (NIR) source with a CaF_2 beam splitter and a polarizer. An InGaAs detector is placed inside Hyperion 2000 Microscope detector compartment in order to make measurements between the 800-2500 nm wavelength region.

For the SERS data collection Renishaw in Via Raman microscope equipped with a 785 nm laser is used. The laser power incident on the sample was 15 mW. The reported spectra are the average of 10 spectra collected with 10 ms acquisition times. 50x objectives, and 10 s accumulation time were standard for all of the samples. Benzenethiol was purchased from Sigma-Aldrich and used in the Raman experiments. The substrates for SERS experiments are prepared by spin coating benzenethiol (10 mM) solution in ethanol, at 4000 rpm for 40 seconds. This provided a homogeneous coating of the molecule all over the sensor surface.

A commercial software package, Lumerical FDTD Solutions, is used for the finite difference time domain (FDTD) simulations. The antenna arrays are modeled to be periodic perpendicular to the plane-wave propagation by using periodic boundary conditions, where the operating wavelength of the source is between 800 nm to 2500 nm. The boundary conditions in the illumination direction are set as perfectly matched layer (PML) to eliminate reflections from the boundaries. A spatial resolution of $dx = dy = 1nm$, $dz = 2nm$, is chosen for an accurate calculation. The structures are illuminated by an x-polarized plane wave, which excites the antenna gap. The material data of gold are taken from Palik, and the sapphire substrate has a constant refractive index, $n = 1.74$, for the operating wavelength regime. The dimensions of the structures are in accordance with the physical sizes measured with SEM and are shown in Figure 3.13. Small mesh size was necessary for more accurate calculations and for the investigation of electric field distributions on the surface of the antennas.

3.4.3 Results and Discussions

The transmission results of the antenna arrays are given in Figure 3.14. Figure 3.14 (a) shows the measurement results, and Figure 3.14 (b) shows the calculated transmission results. The results illustrate that the resonance wavelength of the main bowtie is around 1700 nm. On the contrary, the fundamental mode (TM1,0,-1) is expected to reside at around 1050 nm for an optical projection of the identical bowtie patch antenna with perfect electric conductor (PEC) triangles on a sapphire substrate [97]. PEC, as the name implies, perfectly reflects the impinging electromagnetic wave whereas real metals allow the penetration of the light which will interact with the oscillating free-electron gas and form surface plasmon polaritons. Hence, simulations with only theoretically available PECs help to appreciate the contribution of the plasmonic effects. Conversely, the scalability of Maxwell's equations permit the designers to roughly guess the length of the antenna for the corresponding operational wavelength. For example, a dipole antenna has an approximate total length (L) $L \approx \lambda/2$ at the operational wavelength (λ). This proportion holds very well till optical frequencies, as it is outlined in [98]. The scaling fails at these optical wavelengths due to the plasmonic effects and the resonance wavelength gets shifted to another value similar to the case we encounter for our structure. Moreover, the resonance wavelengths of Fractal-1 and Fractal-2 are 1900 nm and 2300 nm, respectively. While the structures are being miniaturized in each fractal case, the resonance wavelength is increasing. There is a good agreement between the transmission measurements and simulations. The differences mainly arise due to the fabrication imperfections, where the tips of the triangles are rounded, especially for Fractal-2.

A similar resonance frequency shift of the fundamental mode toward longer wavelengths with fractalization is also observed at microwave frequencies for Sierpinski fractal antennas [99] and it has been well associated with an increase in the distributed self-inductance accompanied by the new perforations on the antenna. Then, such shifts at optical wavelengths can also be automatically linked to the slight changes in impedance c as in the case of the microwave counterparts at first glance. However, further simulations (not shown here) have been carried out by

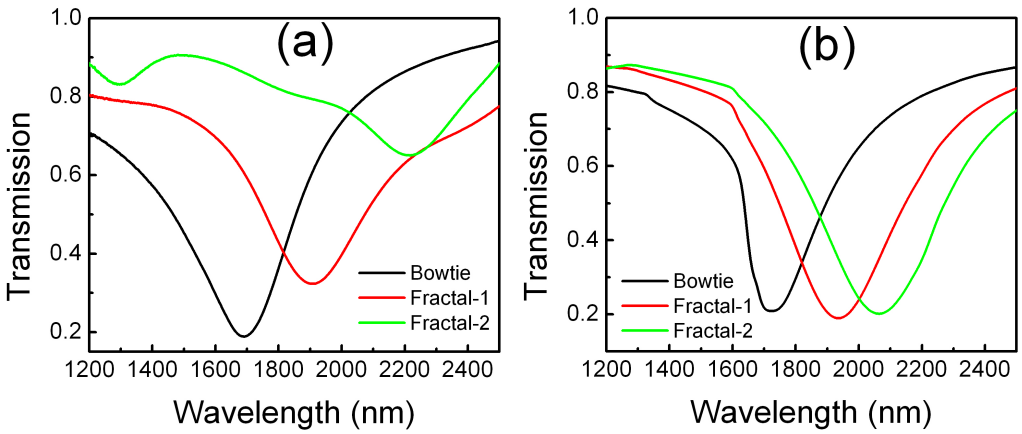

Figure 3.14: Transmission spectra of the antenna arrays (a) experiment, (b) simulation results.

replacing gold with PEC for the same nanoantennas in order to understand the contribution of the plasmonic effects. It is revealed that fractal nanoantennas with PEC parts produce only very minor shifts ($\sim 10nm$) with fractalization steps. Therefore, the shifts at optical wavelengths with real metals should be dominantly attributed to the modifications on the surface plasmon currents of the nanoantennas. If the shifts were mainly caused by the additional self-inductances coming from the perforations, we would end up seeing pronounced resonance wavelength shifts while still assigning PEC as the building block of the fractal nanoantennas. The elucidation of this phenomenon can be helpful in understanding the working principles of such antennas.

The bowtie antenna comprises two triangles that constitute coupled dipole moments. We can only excite the x-polarized modes (bright modes) along the polarization direction of the incident plane wave in our current configuration. This effective coupling between the triangles already causes red shifts from the original resonance frequency of the individual triangles for the bright modes. Hence, an additional red/blue shift is well known to be a consequence of an increase/decrease in the dimension of the nanoantenna along the axis of the polarization [100] or a decrease/increase in the size of the gap in between the triangles [101]. Fractalization takes out certain portions of the metal and creates nanocavities. Generally, nanocavities hybridize the supported plasmonic modes and generate bonding and antibonding states with slightly altered frequencies depending on the strength of

the interaction between the cavity and outer layer plasmons [102]. In case of a bonding state, the plasmon mode can be tuned to longer wavelengths by decreasing the thickness of the surrounding metallic frame, which dictates extracting out larger portions of the metallic layer from the original bowtie. Another scenario for coupling can be visualized between the connected subwavelength features; triangles in our case. The touching spots of the triangles enables a bridge to redistribute the surface charges in a delocalized fashion, as suggested in [103]. The near-field interactions compel both of these coupling scenarios to come into play for higher modes at shorter wavelengths, too. The fractalization stages alter the polarizability as well as the extinction spectra of the bowtie nanoantenna. As a result, in certain wavelength regimes the fields tend to get scattered over the Sierpinski fractal nanoantennas rather than getting localized just in the vicinity of the gap or along the equilateral outer side walls. Moreover, the number of the intensified electrical field points on the surface of the Sierpiski fractal nanoantennas is boosted while the surface charges get delocalized. These changes are the results of the plasmonic coupling between the subwavelength features.

The ideal fractal parts of the Sierpiski fractal antennas touch each other at a single point. However, each triangle element needs to be connected to its neighboring triangle in the simulations in order to avoid the geometric singularities [96]. Otherwise, a collective excitation from all of the triangles cannot be obtained due to the discontinuity. We showed in Figure 3.15 (a) that the connection of the triangles is very crucial. The fractal resonance completely deteriorates if the triangle elements are separate from each other. Moreover, a rather weak resonance is measured at smaller wavelengths, which originates from the individual triangles. In other words, the configuration acts such as a triangular plasmonic array. FDTD simulations are carried out in order to validate this deduction. For that case, the configuration acts as a set of capacitively coupled single subwavelength triangles and yields a weak resonance at 1200 nm when the triangles are isolated. From the framework of the plasmonic coupling discussions that are outlined in the previous paragraph, the red-shifted resonance at 1900 nm is the result of the hybridization and conductive coupling effects. It is seen in Figure 3.15 (b) that the resonance dip of the Fractal-1 is achieved when the tips of the neighboring

triangles are touching. Therefore, it is important that the fractals are connected for the continuum of the current density.

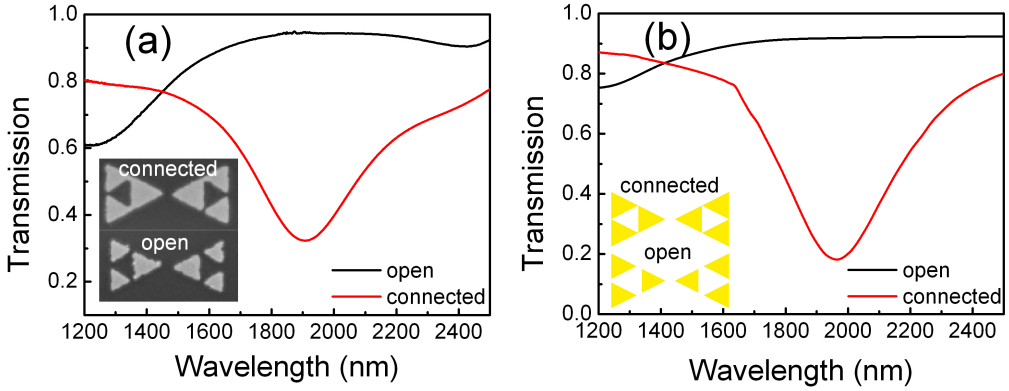

Figure 3.15: Transmission spectra of open and connected Fractal-1 structures: (a) experiment, (b) simulation.

The fractal bowtie nanoantennas are expected to exhibit an extraordinary enhancement and electric field localization when compared to the conventional bowtie antenna. This is due to the increased density of the hotspots generated in the cavities for both designs, which in turn excites a larger area on the metal surface, even though the area of the metal is decreased after each fractalization. The enhanced localized fields on the fractal antennas provide a platform as efficient SERS substrates. It has been shown before that the higher the density of hot-spots, the higher the total signal intensity in SERS will be [90, 104–106]. Raman measurements of the structures are given in Figure 3.16. SERS signal intensity at 1075 cm^{-1} is enhanced by a factor of 8 for Fractal-1, and it is enhanced 16 times for Fractal-2 when compared to the conventional bowtie antenna.

Figure 3.17 shows the electric field distribution of bowtie, Fractal-1, and Fractal-2 structures at 895 nm, which is the Stokes shifted wavelength. In Fractal-1, the simulations show a higher electric field distribution both in the cavity and in between the tips of the triangles forming the bowtie. Moreover, for the case of Fractal-2 geometry, this is further enhanced since the number of engravings that serve as hotspots is increased. The figures clearly depict that the hot spots responsible for the surface enhanced Raman effect are becoming more dominant as the degree of fractals is increased.

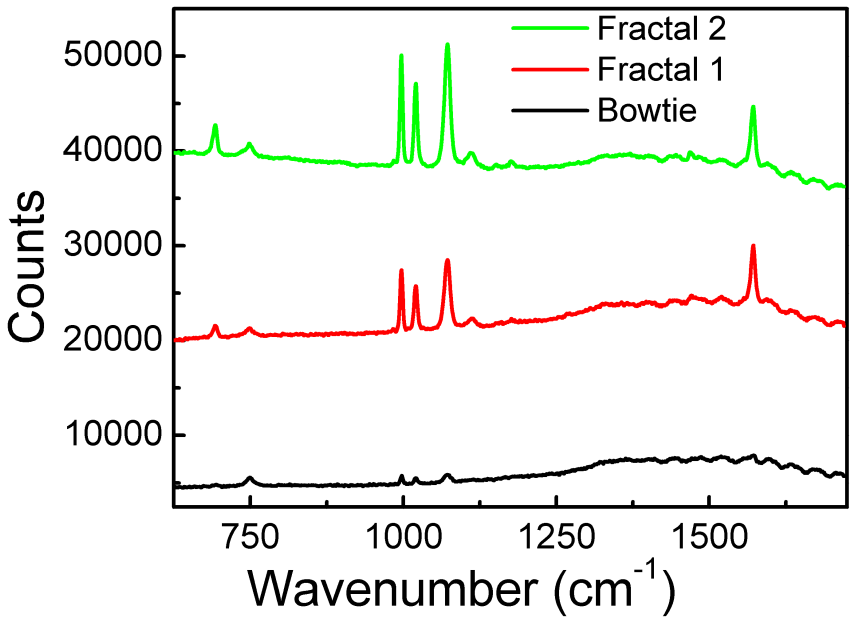

Figure 3.16: SERS measurement results for Bowtie, Fractal-1 and Fractal-2.

In [107], Hsu et al. has shown SERS enhancement with a Sierpinski carpet for which the isolated nanostructures contributed to the electric field localization. Higher electric field enhancement values can be attained in comparison to the continuous metal films. The enhanced SERS factors rely on localized surface plasmons rather than surface plasmons in such structures. On the other hand, the conductive bridges between the self-similar triangles are vital to generating again self-similar electric field distributions as shown in Figure 3.17 for the Sierpinski fractal bowtie nanoantennas.

The electric field distribution is obtained for all three designs both at the excitation and Stokes shifted wavelengths. Then, $|E_{excitation}|^2 |E_{Stokes}|^2$ is integrated over the gold areas. According to the simulation results, the integrated E-field is 24 times the bowtie antenna for Fractal-1, and 32 times the bowtie antenna for Fractal 2.

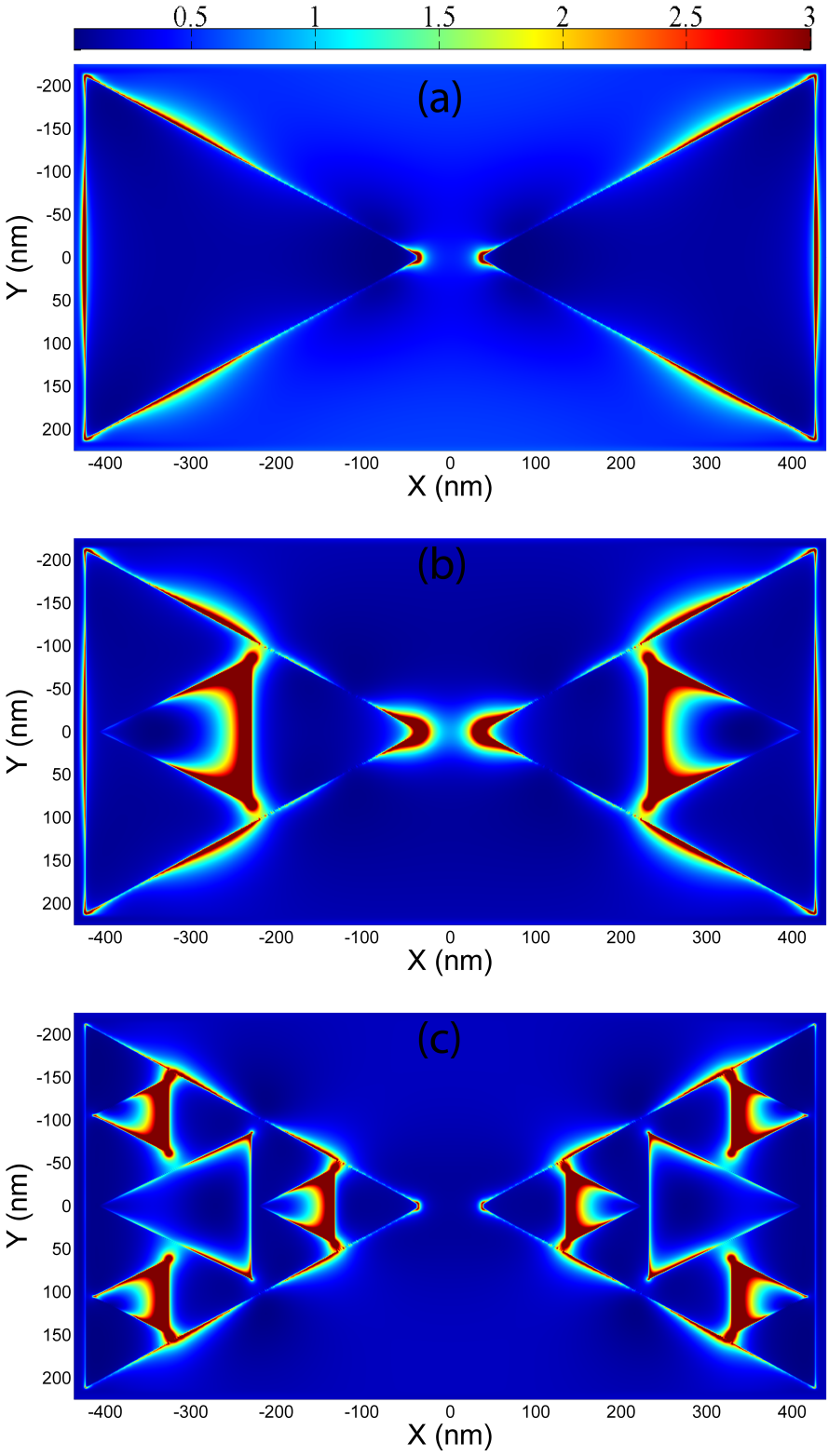

Figure 3.17: Electric field distributions at the Stokes shifted wavelength, 895 nm. (a) Bowtie, (b) Fractal-1, and (c) Fractal-2. The maximum of the color bar is set to the same value for comparison.

3.5 Conclusion

We have demonstrated the influence of plasmonic lens properties (inner diameter and slit width) on SERS performance. The results show that when the slit width is increased, the SERS performance of plasmonic lens decreases. The maximum SERS performance was obtained with the plasmonic lens having 200 nm slit width for all plasmonic lenses with different ring diameters. The slit width was kept constant (200 nm) to investigate the influence of ring diameter on SERS. The SERS intensity obtained from plasmonic lens having 3.0 m inner diameter is 13.2 times higher compared to planar silver thin film which is consistent with the theoretical calculations. This study suggest that the strong relationship between the surface plasmons and SERS activity can be used to built unique structures to prepare well-defined arrays to use in several applications of SERS.

Then, we present our preliminary results in designing plasmonic nano-patterned structures that can work as highly efficient SERS substrates. The proposed design gives more than two orders of magnitude larger signal intensity than plain gold film and nearly one order of magnitude larger than an optimally designed etched-ring plasmonic lens structure.

Finally, we experimentally and numerically demonstrated that the fractal bowtie antennas operate at longer wavelengths compared to the conventional bowtie antenna of the same size, even though the metallic area is reduced after each fractalization. Furthermore, we showed that the fractal antennas have multiple hot spots, in which the electric field is enhanced and localized. We measured that these hot spots increase the SERS signal. The experimental results and the simulations showed good agreement. It is possible to use such structures as frequency-selective miniaturized antennas, and efficient SERS substrates.

Chapter 4

Graphene Based Nanophotonic Devices

4.1 Introduction

Graphene is a monolayer structure composed of hexagonally arranged carbon atoms. It has a two-dimensional (2D) honeycomb lattice structure. Since graphene has interesting electrical and mechanical properties, it has been an attractive research material in recent years. An electron inside a monolayer graphene sheet has zero effective mass [108], and it can travel for micrometers without scattering even at room temperature [19, 109]. Graphene also exhibits many interesting and exotic properties ranging from ballistic electronic transport [110–112] to the anomalous quantum Hall effect in electrical transport [108, 112] and tunable interband transitions [113, 114]. Property of the ballistic transport of electrons in graphene makes it a very unique material, since its mobility can go up to 100000 $cm^2V^{-1}s^{-1}$ [115, 116]. Its optical properties make it ideal for terahertz oscillators and low-noise electronic and optical sensors [117]. There is still an ongoing research on the growth of graphene. There are two main methods: In the first method, single or a-few-layer graphene sheets are mechanically or chemically split off the bulk graphite crystals and deposited on to a SiO_2/Si

substrate by means of transfer methods so that a free-standing graphene is produced [118]. In the other method, single and few layer graphene can be epitaxially grown on 4H-SiC or 6H-SiC substrate, by the thermal decomposition of either Si- or C-terminated surface at high temperatures (up to 1200^oC). The number of graphene layers is controlled by temperature and time [119]. Epitaxial graphene (EG) grown on SiC is suitable for large area fabrication and is more compatible with current Si processing techniques for future applications.

Graphene is a versatile optical material for nanophotonics applications [19] such as metamaterials [20], photodetectors [21], light emitting devices and ultrafast lasers [22]. In particular, graphene with its planar nature, attracts an increasing research interest as a promising novel tool for nanoplasmonics and nanoscale electronics [120, 121]. Pioneering works of graphene were focused on the single particle excitation of electrons. On the other hand, the plasmonic properties of graphene layer, which is a result of the collective excitations of 2D massless electrons, has become an emerging research area in recent years. Plasmonic resonances in graphene give outstanding potential for designing novel optoelectronic devices by its remarkably high absorption [19, 23, 24]. Electrical response at terahertz frequencies are high enough to design plasmonic devices [110, 122]. However, the electrical control of plasmon resonance becomes a challenge at optical frequencies as a result of drastically reduced free electron responses with increasing frequency. Graphene, which is a novel zero bandgap semiconductor [113, 114, 122], is a great candidate to overcome this challenge. Since high frequency interband transition in graphene can be exploited through electrical gating [122], plasmon resonance of graphene-hybrid device like split ring resonators (SRRs) can be modulated by applying gate voltage [25, 26], which changes the carrier concentration, and thus modulating the optical conductivity [27, 28].

Surface plasmons have the characteristics of concentrating light into a subwavelength volume, which is one of the main tools of plasmonics [122, 123]. Plasmons in graphene is an active research field [23, 24, 124–126], and it is desired to control the plasmon resonances for optical switch applications. Surface plasmons that are bound to graphene are confined to volumes on the order of $\sim 10^6$ $(1/\alpha^3)$ times smaller than the diffraction limit, where $\alpha = e^2/\hbar c$ is the fine structure

constant [127]. As a result, these strong light-matter interactions make graphene favorable for new plasmonic applications due to the field enhancement and confinement.

4.2 Electrical characterization of graphene

In this study, we used the Van der Pauw geometry for the Hall Measurements. Hall measurement is a technique to measure the mobility with the help of charge carriers. We designed and fabricated our own photomask by using electron beam lithography. Ohmic contacts are fabricated with the reverse lithography technique. After development, 20 nm titanium and 100 nm gold were deposited by electron beam evaporator, and then followed with the standard lift-off process. The mesa lithography step was performed in order to preserve the active graphene region of the Hall bar devices with a photo-resist, while etching the rest of the graphene on the SiC substrate. The etching process was carried out with oxygen plasma by using Inductively Coupled Plasma Reactive Ion Etching (ICP-RIE), where the ICP power was 100 W and the RF power was kept 50 W. The samples were exposed to the plasma for 20 seconds, which completely removes the graphene on the surface. After the etching process, 500 μm by 1100 μm, the active graphene region was obtained. Interconnect metal lithography was performed by using 30 nm/220 nm Ti/Au metal pair. Finally, devices were bonded for Hall measurements. A complete fabrication is shown in 4.1. Finally, devices were bonded for Hall measurements.

The temperature dependence of the sheet carrier density and Hall mobility in the graphene is plotted in Figure 4.2. At low temperatures, the sheet carrier density remains practically constant up to a temperature of 100^oK. At higher temperatures, the sheet carrier density increases monotonically with increasing temperature due to thermally generated carriers located outside the channel. A similar behavior of carrier density with temperature, although less pronounced, was reported previously for 2D structures. The Hall mobility of electrons in the graphene sample increases monotonically with a decreasing temperature from

Figure 4.1: Fabricated Van der Pauw Hall device.

room temperature, begins to level off at about 100^oK, and saturates at about 50^oK. This behavior reflects the 2D character of the electrons in the channel.

4.3 Epitaxial graphene transistor with transparent top-gate for resonance broadening and tuning of split ring resonators

In this study, we report the fabrication, design, and measurement of a device comprising a split ring resonator (SRR) array on epitaxial graphene. We obtained resonance broadening and tuning of split ring resonators by utilizing an epitaxial graphene transistor with transparent top-gate.

4.3.1 Design and Fabrication

The graphene sample in this study is grown by the sublimation method on 4H-SiC polytype. The sample is intercalated by hydrogen, where the temperature of

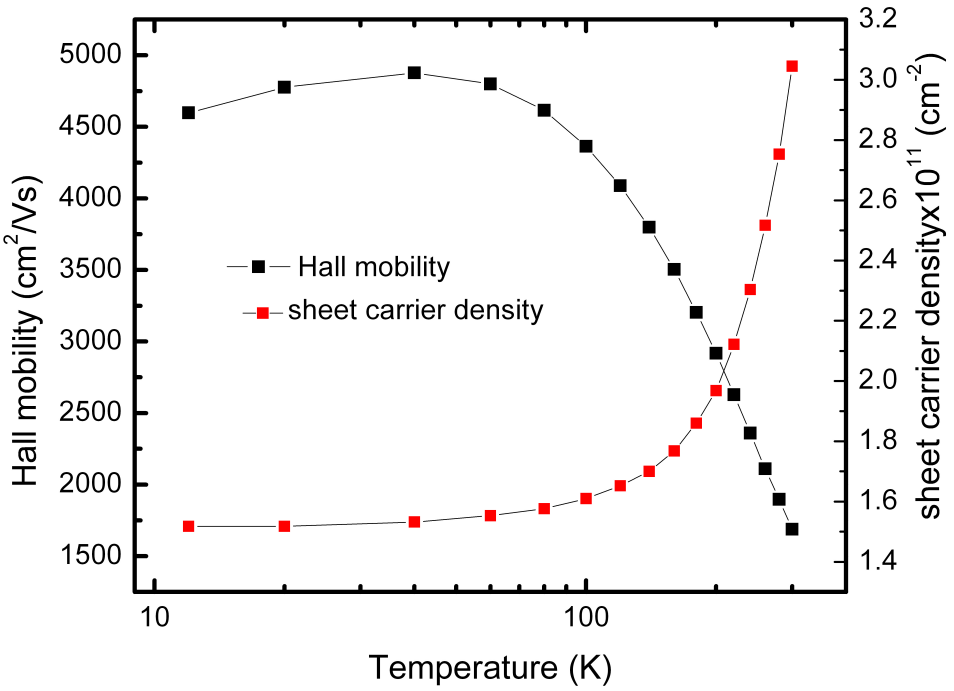

Figure 4.2: Temperature dependence of the sheet carrier density (N_H) and Hall mobility (μ_H) of electrons in the graphene.

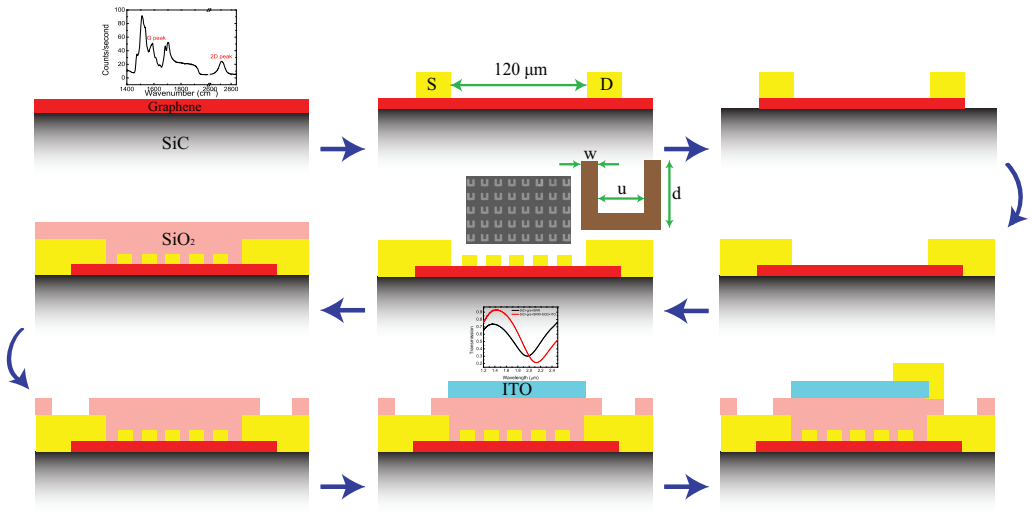

Figure 4.3: Schematic of the device fabrication steps.

sublimation is 1600^oC, and the reactor pressure is set to 50 mbar. The sample is p-type with a carrier concentration of $1.3x10^{13}cm^{-2}$, and the mobility is measured to be 3234 cm^2/Vs. In terms of the fabrication of the samples, first of all, a chromium mask is designed and fabricated by electron beam lithography to be further used in optical lithography for device fabrication. This mask is designed to work with 1 cm x 1 cm graphene samples on SiC substrate, and six devices fit on one sample. Fabrication steps are schematically shown in Figure 4.3 starting from the Raman measurement of the bare graphene, where characteristic 2D and G peaks of graphene are visible along with the SiC peak. The sample is spin coated with a positive-tone photo-resist and then the reverse photolithography of the ohmic contacts are performed to form the source and drain contacts. After developing the samples for 20 seconds, 20 nm titanium and 80 nm gold are deposited by the electron beam evaporation method, followed by a standard lift-off process with acetone. 100 μm x 100 μm ohmic contacts are 120 μm apart from each other, abbreviated as S and D in Figure 4.3. After the ohmic contact metallization, mesa etch lithography is performed in order to isolate the devices electrically from each other. The sample is exposed to oxygen plasma for 20 seconds by using Inductively Coupled Plasma Reactive Ion Etching (ICP-RIE), where the RF power is 50 W and ICP source power is 100 W. This results in a 120 μm x 100 μm graphene channel between the source and drain contacts. Then, another photolithography for interconnect metallization, which consists of 20 nm titanium and 200 nm gold, is performed for the probing and wire bonding purposes during the measurements. This step provides large pads connected to source and drain contacts. Later, the fabrication of the split ring resonators is done by electron beam lithography on the active graphene region. The sample is spin coated with the positive-tone electron beam resist Poly(methyl methacrylate) (PMMA) A4. 15 kV accelerating voltage is applied and 10 μm aperture is used for the exposure. After electron beam lithography, 5 nm titanim as a buffer layer, and 40 nm gold are evaporated. A scanning electron microscopy (SEM) image of a split ring resonator array is shown as an inset of Figure 4.3. Then, the dielectric passivation step is carried out with 100 nm SiO_2. This process is performed in two steps, where 50 nm SiO_2 is deposited by electron beam evaporation and 50 nm SiO_2 is deposited by sputter. Several trials showed that

the gate leakage cannot be avoided by doing the electron beam evaporation step only. The reason is that the electron beam evaporation provides a very directional deposition on the surface and it does not cover the sides of the metallic structures and the bumps due to the gold evaporation, and, hence, it leads to the leakage current caused by the split ring resonators, when the gate fabrication is completed. However, sputtering as a second step entirely covers all of the sides as well as the bumps on the metal surfaces such as a blanket, thus providing a proper isolation layer. The reason why electron beam evaporation is used before the sputtering is to protect the graphene surface from the plasma exposure of the sputter system. Argon plasma is created and used during the sputtering process. It was shown in Refs. [128, 129] that the graphene is highly sensitive to Ar plasma, which can create defect sites on the surface. After the dielectric deposition steps, another etch process is performed in order to physically reach the source and drain contacts, as shown in the left bottom corner of Figure 4.3. CHF_3 plasma is used in order to etch SiO_2 layer, where the RF power is set to 100 W, and ICP power is set to 200 W resulting in 100 nm/min etch rate. Since the 6H-SiC substrate under the graphene layer is semi-insulating, a top-gate is needed to apply the bias voltage. Indium tin oxide (ITO) is chosen to be the gate material due to its conductivity and transparency. Photolithography process is performed, so that a 100 nm-thick ITO window just above the active graphene region can be deposited by sputtering. As a final process step, a gold metal pad connected to the ITO is fabricated with the same steps followed in source-drain interconnect metallization.

4.3.2 Results and Discussions

IV measurements are performed in order to investigate the gate-dependent DC modulation performance of the devices. The results are plotted in Figure 4.4. Figure 4.4 (a) shows the change of the IV characteristics between source and drain contacts under different gate voltages. Each curve is linear, and hence has a constant resistance, which is the indication of the ohmic contact characteristics. Resistance increases up to 60 V of gate voltage and then decreases for higher

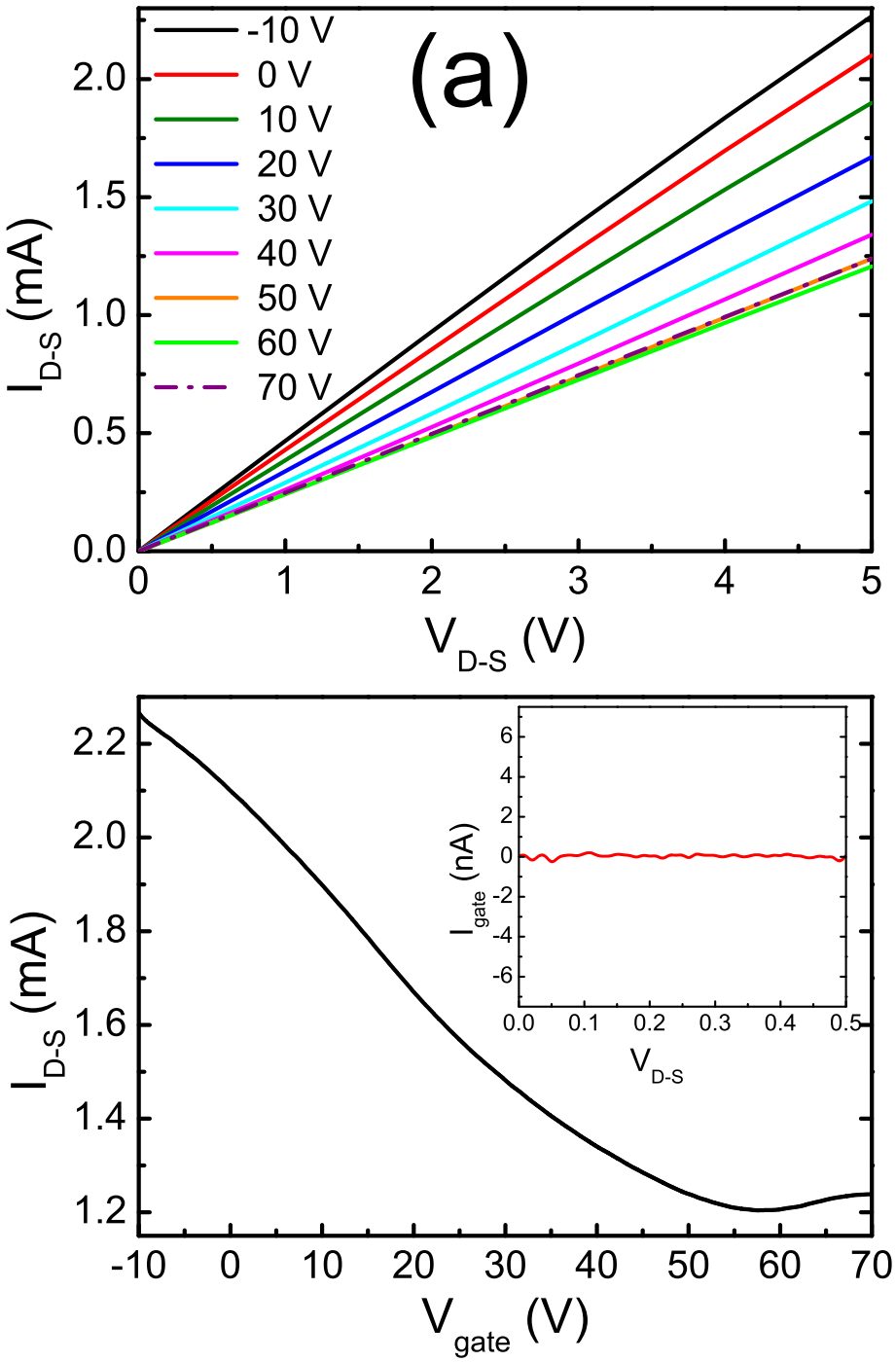

Figure 4.4: DC-IV Measurements (a) drain voltage vs drain current, (b) gate voltage vs drain current; inset shows drain voltage vs gate current.

gate voltages. This turning point can be seen clearly from the saddle point of Figure 4.4 (b). It can be concluded that the Dirac point, which is the charge neutrality point, is around 60 V. Measurements are performed up to 70 V in order not to exceed the breakdown voltage of SiO_2. Gate current at $V_{gate} = 60V$ is measured to be on the orders of 10^{-11} A, as shown in the inset of Figure 4.4 (b), which proves that there is no gate leakage, and the dielectric passivation step is successfully completed.

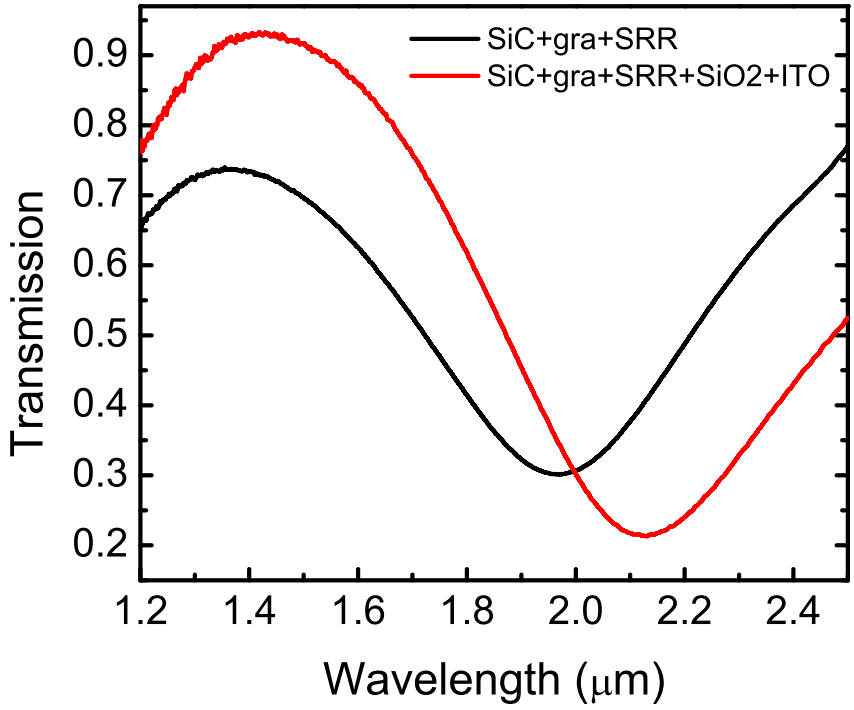

Figure 4.5: Transmission measurements before and after depositing ITO and SiO_2 layers.

Transmission of SRRs before and after the deposition of SiO_2 and ITO layers is measured, as shown in Figure 4.5. A red shift about 200 nm at the resonance wavelength is observed after the deposition of these layers.

In this study, there are two resonant devices that operate at different wavelengths. Resonance wavelength of Device 1 is at around 2 μm, whereas the resonance wavelength of Device 2 is around 4 μm. The transmission spectra of

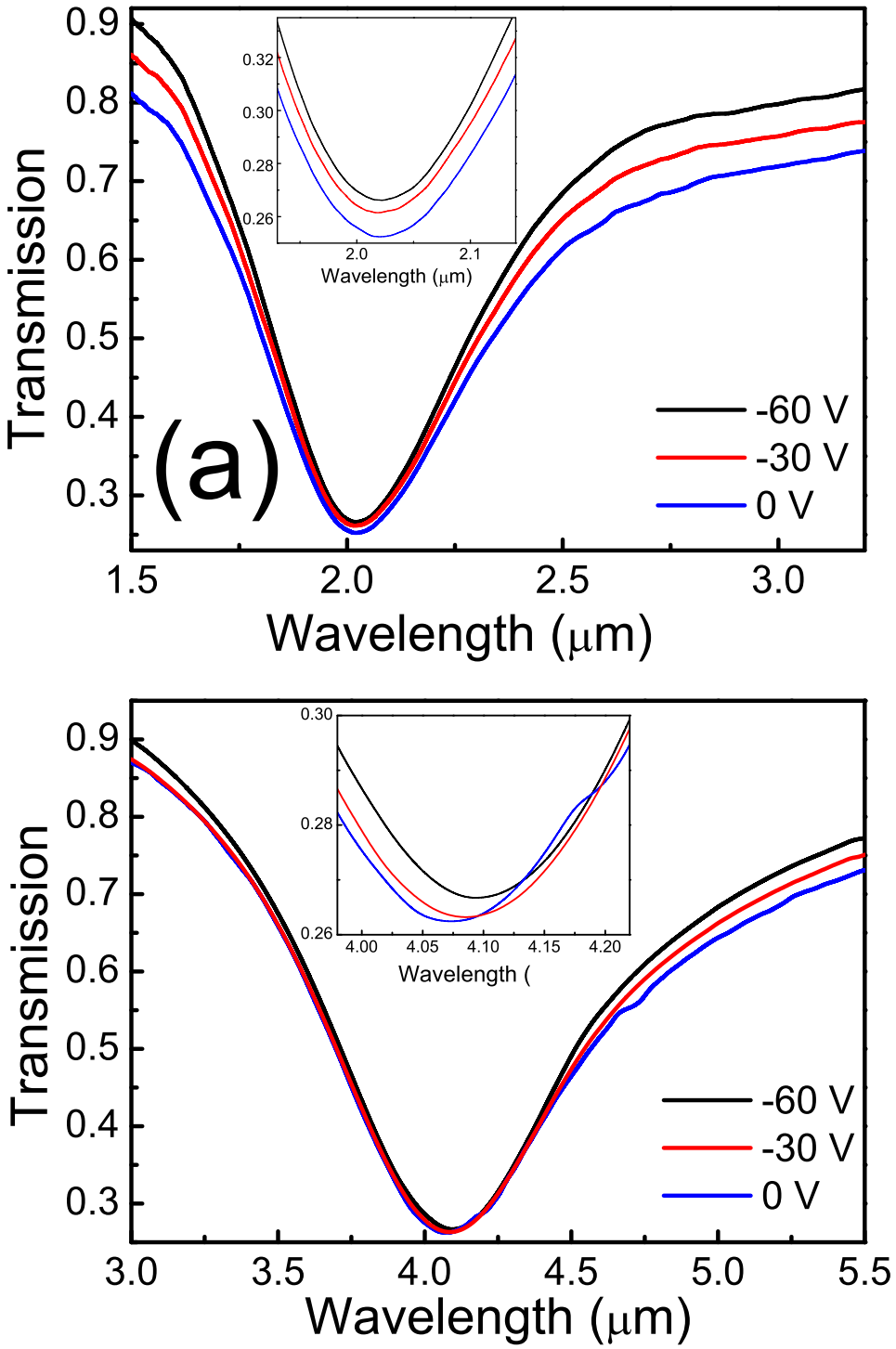

Figure 4.6: Transmission measurements under different gate voltage differences, ΔV, for (a) Device 1, and (b) Device 2.

these two devices under different gate voltage differences, $\Delta\ V$, are shown in Figure 4.6, where the resonance dips are enlarged in the inset. Here, $\Delta\ V$ is defined as $\Delta\ V = V_{gate} - V_{CNP}$, where V_{CNP} is the voltage value at the charge neutrality point. It should be noted that the curves change their shape asymmetrically with applied voltage. 28 nm blue shift at the resonance wavelength is measured and demonstrated in the inset of Figure 4.6 (b). The reason of this asymmetric and the shift behavior is the higher sensitivity of graphene to the light at higher wavelengths.

Line width and quality factor variations with respect to gate voltage difference are plotted in Figure 4.7. $\Delta\ \lambda$ is the line width difference with respect to the line width of the curve measured at $\Delta\ V = 0$. The line width decreases, and as a result the quality factor increases, as ΔV decreases, which is to say that the curves narrow down away from the charge neutrality point. An incident photon having an energy $\hbar > 2E_F$ can be absorbed, because it generates an electron-hole pair. Fermi energy, E_F, approaches zero at the charge neutrality point, which results in more intraband transitions due to the incident photons and hence, absorption increases. The results presented in Figs. 4.6 and 4.7 are consistent with the theory. Transmission curve at the Dirac point, where $\Delta\ V = 0V$, is the broadest one having the lowest quality factor, as expected. The reason is that the absorption is the highest for this case.

4.4 Resonance tuning and broadening of bowtie nanoantennas on graphene

In this study, we demonstrated that the intensity and resonance peak of bowtie nanoantennas on monolayer graphene can be tuned by applying a gate voltage, since the optical properties of graphene change by changing the carrier concentration.

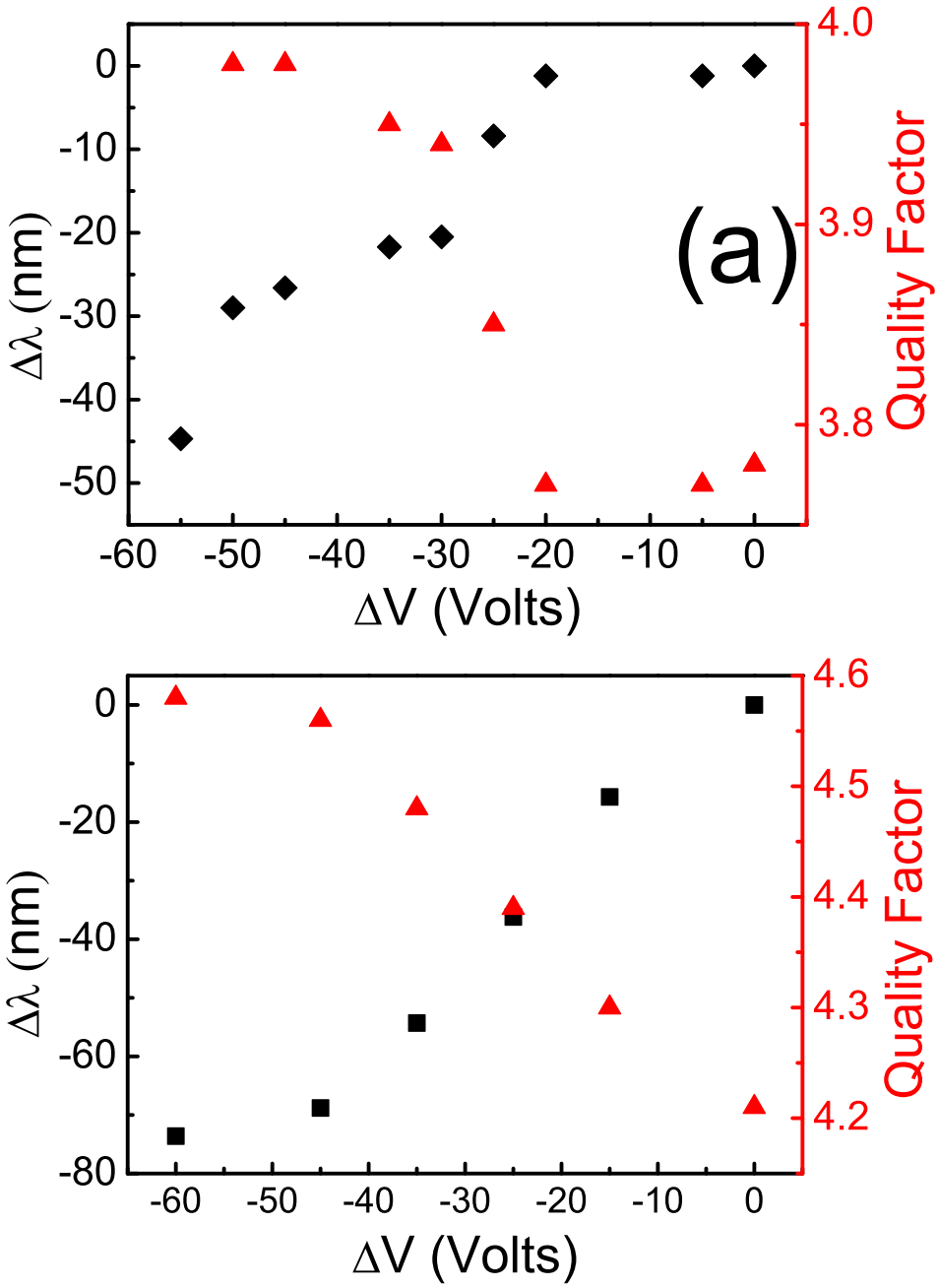

Figure 4.7: Line width difference, $\Delta\ \lambda$, and quality factor variation for (a) Device 1, and (b) Device 2.(Black squares represent the line width difference, and red triangles represent the quality factor.)

4.4.1 Design and Fabrication

Commercially available (Graphene Supermarket) monolayer graphene samples on p-doped silicon substrates coated with 285 nm SiO_2 dielectric film are used in fabrications. In order to measure the mobility and carrier concentration of graphene samples, Hall measurement, which is a technique to measure the mobility with the help of charge carriers, is performed by fabricating four-contact Van der Pauw devices as shown in Figure 4.8 (a). The average of several Hall measurements at room temperature from different Van der Pauw devices of a chip sized 1 cm x 1 cm resulted that the graphene samples are very uniform, and they have a mobility of 2286 cm^2/Vs, and $7.85x10^{12}cm^{-2}$ sheet carrier concentration, where the positive carrier concentration means that the majority carriers are holes.

For the preparation of the transistor-like devices with bowtie antennas, we fabricated our own optical mask by using electron beam lithography. The first step of the device fabrication is the ohmic contacts with optical lithography for the drain and source. 20 nm titanium and 80 nm gold are deposited as ohmic contact metallization with electron beam evaporator. Then, optical lithography for mesa etching is carried out in order to obtain the active area that connects the source (S) and drain (D), and thus removing the unwanted graphene on the chip. The etching process is carried out with ICP-RIE by exposing samples to O_2 plasma for 20 seconds with 50 W RF power, and 1100 W ICP source power. After that, another optical lithography for interconnect metallization is done in order to be used for probing and bonding purposes. 20 nm titanium and 200 nm gold are evaporated as interconnect metals. As the last step of the nanofabrication, bowtie arrays are lithographed on the active region by using electron beam lithography, followed by 5 nm Ti and 40 nm Au evaporation. Optical microscopy image of a completed fabrication of a device is shown in Figure 4.8 (b). Scanning electron microscopy (SEM) image of a unit cell of a bowtie antenna array, which will be referred as Sample 1, is given in the inset of Figure 4.8 1 (b). Here the gap distance is measured to be 177 nm, total length of a single bowtie is 4.46 μm, and the flare angle is 58^o. Before the optical measurements, dark current-voltage measurements were performed. Charge neutrality point of the graphene sheet is

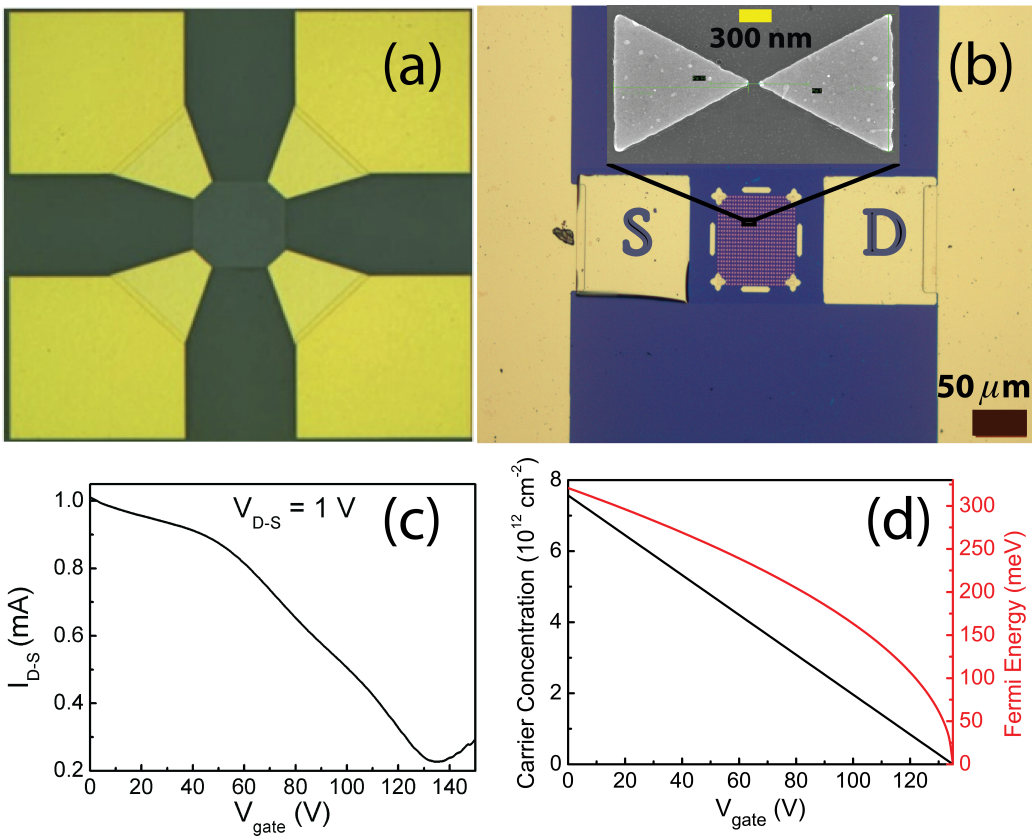

Figure 4.8: (a) Fabricated four-contact Van der Pauw device for Hall measurements, (b) optical microscopy image of the tunable bowtie device, i.e. active graphene region with nanostructures between drain (D) and source (S) contacts; inset showing SEM picture of a bowtie antenna, (c) measured drain-source current with respect to the gate voltage, and (d) calculated variation of carrier concentration and Fermi energy with respect to the gate voltage difference ΔV.

observed to be at 135 V, as plotted in Figure 4.8 (c). High carrier concentration of graphene, as measured using Van der Pauw devices, results in a large value of charge neutrality point. The reason is predicted to be due to the resist residues on the graphene surface as discussed in Reference [130].

It was demonstrated in References [108] and [113] that the charge concentration is linearly proportional with the applied gate voltage and, therefore, the optical conductivity of graphene can be tuned at different gate voltages. Relation between the applied gate voltage and carrier concentation/Fermi energy is plotted in Figure 4.8 (d). Here the voltage difference, ΔV, is defined by $\Delta V = V_g - V_{CNP}$, where V_g is the gate voltage and V_{CNP} the voltage at the charge neutrality point.

4.4.2 Results and Discussion

Fourier transform infrared (FTIR) spectroscopy measurement results for Sample 1 are given in Figure 4.9. Reflection spectrum in Figure 4.9 (a) shows that reflectivity changes with a blue shift, as the voltage difference increases, since the refractive index of the graphene layer changes with the applied voltage. There is a 113 nm shift at the peaks between $\Delta V = 0V$ and $\Delta V = 140V$ cases, as demonstrated in the inset of Figure 4.9 (a). Along with the blue shift, reflection curves exhibit an asymmetric nature with the applied voltage. The reason of this asymmetry is that the tuning of the curves are much more pronounced at longer wavelengths, because the optical conductivity of graphene changes more at the longer wavelengths for different Fermi energies. In other words, graphene is more sensitive at longer wavelengths. It is also observed that the resonant curves narrow down for larger ΔV, which will be discussed later. Relative reflectivity with respect to the reflection at the charge neutrality point is shown in Figure 4.9 (b). It is seen that the curves blue shift by applied voltage. There is also electrical damping especially around 7 μm. Calculated results of $|E_x|^2$ on the surface at the wavelengths of 5.5 μm and 7.0 μm are demonstrated in the inset of Figure 4.9 (b), in order to be able to understand the reason of the intensity change at 7 μm. The real and imaginary parts of the refractive index of graphene are

calculated for different Fermi energies, and hence different gate voltages. The numerical simulations are performed by using commercially available software package Lumerical by embedding these refractive index data as a new material. Field intensity and localization at off-resonance wavelength (7 μm) is higher than that of resonance wavelength 5.5 μm, where the field is mainly localized at the gap region. Additionally, there is a coupling between neighbor bowties at 7.0 μm, and the tunability of the curves depends on the interaction volume between light and graphene. Enhanced electric field at this wavelength results more interaction with the graphene layer, and the generated e-h pairs decrease the resonance more around 7 μm. Calculated reflectivity of the structures under different bias voltage is also shown in Figure 4.10, where the resonance shift is approximately 190 nm. Fermi energy of the graphene is converted to the voltage difference according to the relation given in Figure 4.8 (d). The results are in agreement with the measurements. The discrepancies are due to the fabrication imperfections, as well as the possible defects and grain boundaries on graphene surface.

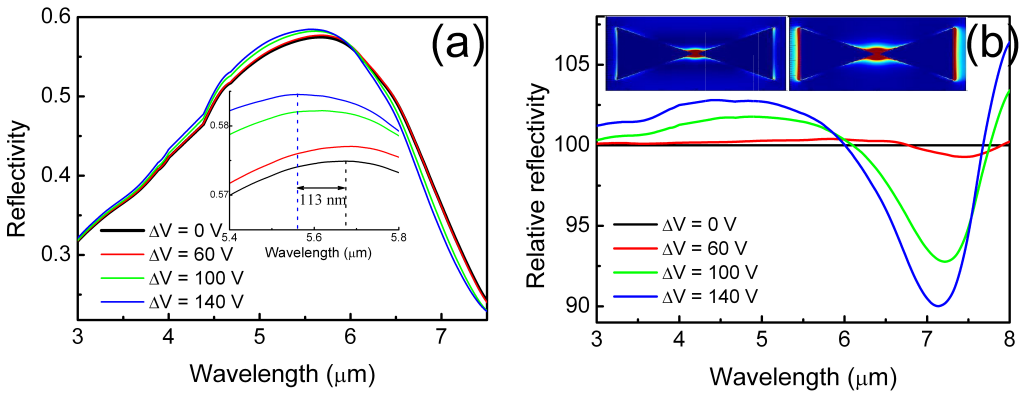

Figure 4.9: (a) Measured reflectance spectra at different ΔV; enlarged view of resonance peaks shown in the inset, and (b) relative reflectivity of bowtie antenna array at different gate voltages; inset showing the x-component of electric field intensity for Sample 1 at 5.5 μm and 7 μm.

Quality factor and line width difference, $\Delta\lambda$, variation under different gate bias are shown in Figure 4.11. Line width represents the full width half maximum of a reflectivity curve, and $\Delta\lambda$ is the difference of full width half maximum values

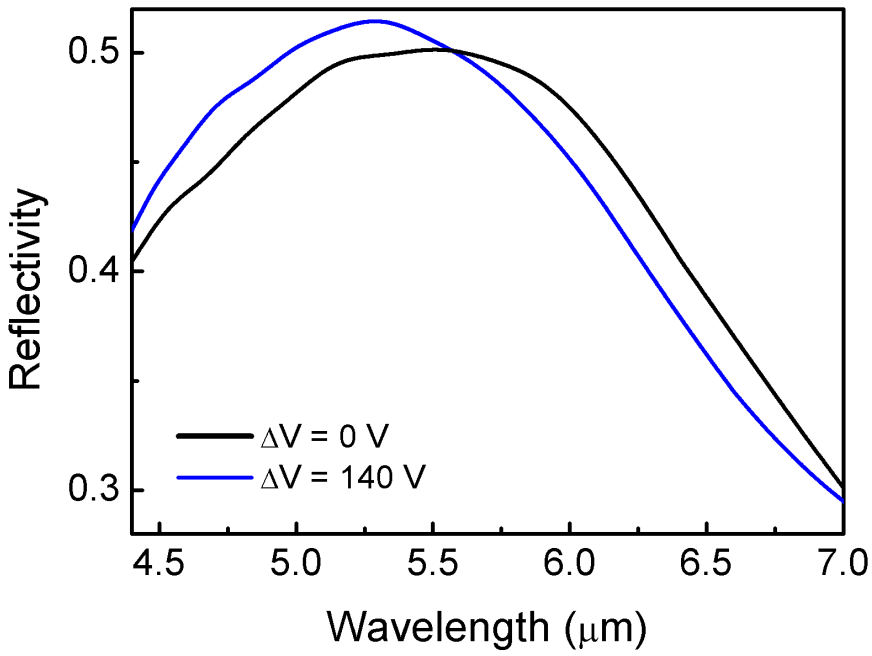

Figure 4.10: Calculated reflectance spectra at different ΔV.

relative to the curve at $\Delta V = 0V$. Line width of the reflectivity peak decreases, as the gate voltage difference, ΔV, increases. In other words, curves narrow down up to 120 nm at larger ΔV. Therefore, the quality factor increases. Incident photons having energies higher than $2E_F$ are absorbed, since they can generate electron-hole pairs. At the charge neutrality point, $\Delta V = 0V$, Fermi energy goes to zero. This results in more interband transitions due to the incident photons, thus increasing the absorption, because almost all of the photons are able to exceed $2E_F$. The results shown in Figure 4.11 are consistent with this qualitative explanation. The reflection curve at the charge neutrality point is the broadest one having the lowest quality factor.

Experimental results for another bowtie antenna array, Sample 2, that operates at 7 μm are given in Figure 4.12 (a) and (b) for TE and TM polarized incident waves, respectively. The total length of a single bowtie is 6.1 μm, and the flare angle is 52^o. It is observed that the damping effect is higher for the case of TE polarization, where the electric field component of the wave is in the x-direction.

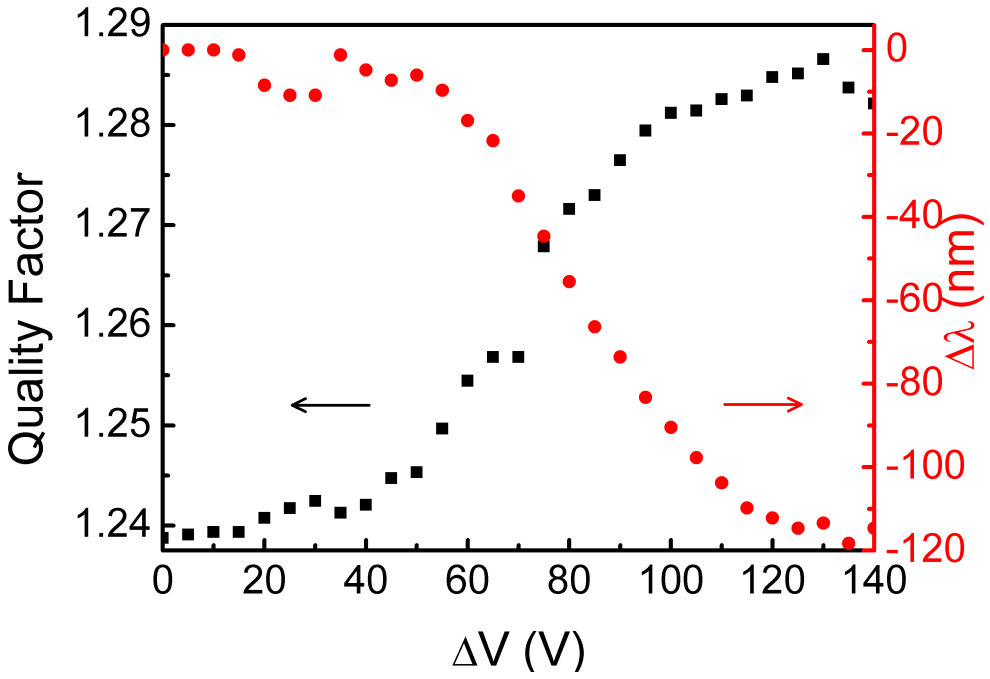

Figure 4.11: Quality factor (black squares) and line width difference (red dots) under different gate bias.

The excitation of the bowtie gap and the coupling between two neighbor antennas can be provided by TE polarization, whereas TM polarization only excites the edges of the triangles. Namely, it works as a periodic array made of triangles, which can be seen from the field distribution insets of Figure 4.12. As a result, the effective graphene area is larger for the case of TE. Therefore, reflectivity is more sensitive to the voltage difference.

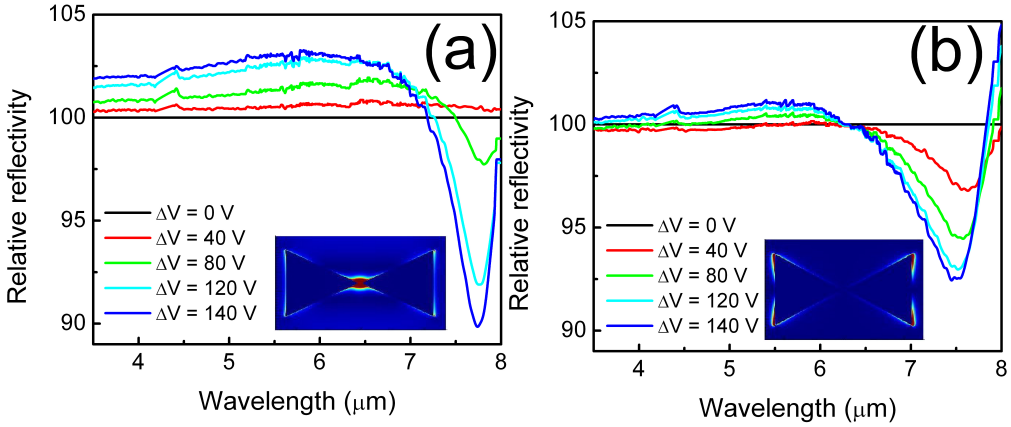

Figure 4.12: Relative reflectivity of Sample 2 for (a) TE polarization, electric field in the x-direction, and (b) TM polarization, electric field in the y-direction.

4.5 Coupling enhancement of split ring resonators on graphene

In this study, we have experimentally and numerically shown that the tunability range of Split Ring Resonators (SRRs) on graphene is enhanced by increasing the interaction volume between graphene and the localized electric field inside the gap region. By designing SRRs that operate at mid-infrared wavelengths with different effective mode areas, we have shown that the reflection spectra of these resonators can be shifted with applied voltage. Moreover, the light-graphene interaction determines the tunability range, and it can be tailored by increasing the effective mode area.

4.5.1 Methods

In this study, CVD grown monolayer graphene on SiO_2 deposited silicon substrate is used, which is provided from the Graphene Supermarket. A schematic of the device is shown in Figure 4.13 (a). SRRs are fabricated on the graphene (shown in purple) sample by electron beam lithography. The metal thickness of the gold SRRs is 50 nm. The devices on the sample are isolated from each other by etching the graphene with oxygen plasma. Later, large contact pad pairs are fabricated by photolithography, and 20/200 nm Ti/Au metals, which function as source and drain contacts, are evaporated for probing and bonding during the measurements. Finally, a Ti/Au metal pair is evaporated on the backside of the sample in order to be used as a back-gate. Gate voltage is applied between graphene and p-type silicon substrate, which are separated by 285 nm thick SiO_2 (shown in blue). Two different types of resonators, SRR-1 and SRR-2 are studied. Their dimensions and SEM images are shown in Figure 4.13 (b) and (c). The only difference between the two structures is that SRR-2 has a larger gap area. The dimensions of the SRRs are $w = 70nm$, $u = 400nm$, $g = 40nm$, and $h = 120nm$; and the period of the arrays is 600 nm in both directions.

The current-voltage (I-V) characteristics of graphene devices are given in Figure 4.14. Figure 4.14 (a) shows that the current flowing on graphene is modulated by varying the gate voltage. The charge neutrality point of graphene is measured as $V_{CNP} = 130V$. I-V measurements between the source and drain contacts are performed. The results in Figure 4.14 (b) show good ohmic characteristics with a constant resistance around $1.2k\Omega$, which is a typical value for graphene samples [131]. Additionally, the mobility and the sheet carrier concentration of graphene are $\mu = 2153cm^2/Vs$ and $N = 5.6x10^{12}cm^{-2}$, respectively, which are obtained by performing Hall measurements. Capacitance per unit area of the devices can be calculated by $C = Ne/V$ [113], which results as $C = 69aF/\mu m^2$.

Finite-difference time domain (FDTD) simulations are carried out using the commercially available software package Lumerical FDTD Solutions. Graphene is introduced as a 1 nm thick dispersive material by using the optical conductivity

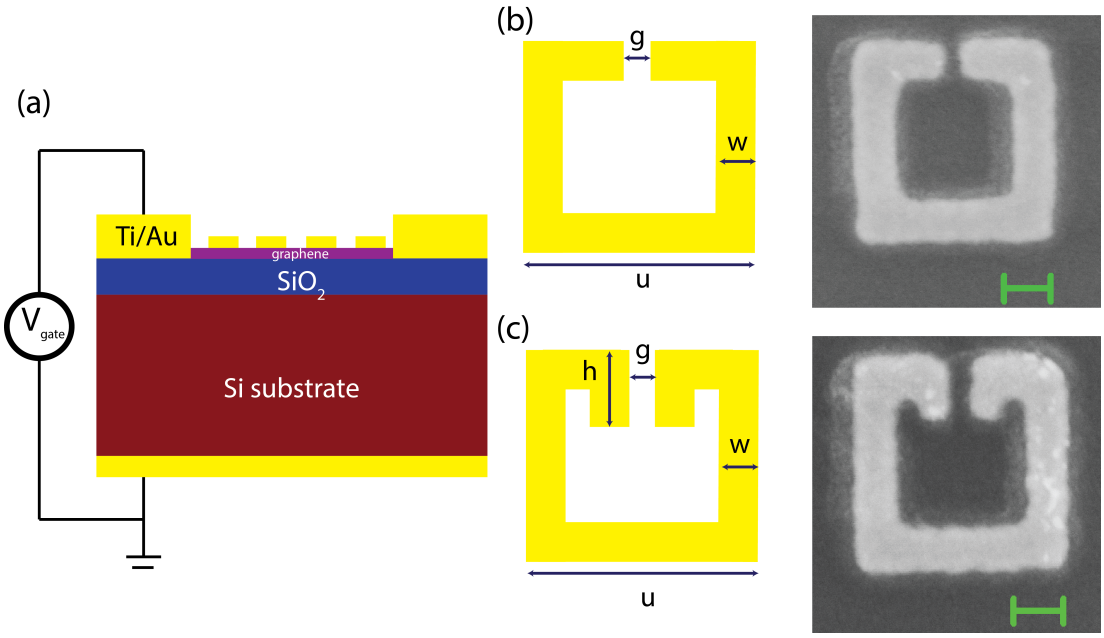

Figure 4.13: (a) Cross-section view of the tunable SRR device; schematics and SEM image of (b) SRR-1, and (c) SRR-2 structures, scale bar is 100 nm. w = 70 nm, u = 400 nm, g = 40 nm, and h = 120 nm.

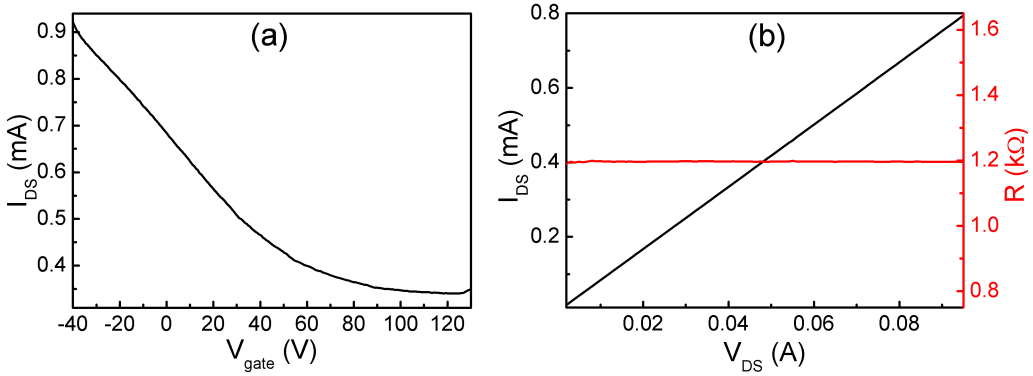

Figure 4.14: DC-IV measurements: (a) current between drain and source under applied gate voltage, (b) current vs. voltage dependence and resistance of graphene.

formula given in Equation 4.1 [27, 28], where k_B is the Boltzmann constant, T is the temperature, ω is the frequency, E_F is the Fermi energy, and τ is the carrier relaxation lifetime.

$$\sigma_s(\omega) = \frac{2ie^2k_BT}{\pi\hbar^2\left(\omega + \frac{i}{\tau}\right)} \ln\left[2\cosh\left(\frac{E_F}{2k_BT}\right)\right] + \frac{e^2}{4\hbar}\left[\frac{1}{2} + \frac{1}{\pi}\arctan\left(\frac{\hbar\omega - 2E_F}{2k_BT}\right) - \frac{i}{2\pi}\ln\left(\frac{(\hbar\omega + 2E_F)^2}{(\hbar\omega - 2E_F)^2 + 4(k_BT)^2}\right)\right] \quad (4.1)$$

The carrier relaxation lifetime, τ, is calculated by using Equation 4.2. Here $\sigma = Ne\mu$ is the semi-classical diffusive conductivity for 2D graphene, where N is the sheet carrier concentration, μ is the mobility, and $g_s = g_v = 2$ are the spin and valley degeneracy factors [132].

$$\tau = \sigma\frac{h}{g_sg_ve^2}\frac{2\hbar}{E_F} \quad (4.2)$$

The optical conductivity of graphene depends on Fermi energy (Equation 4.3), which is a function of the sheet carrier concentration. Fermi energy, and thereby the sheet carrier concentration, can be changed by applying gate voltage, which is linearly proportional to the sheet carrier concentration [108, 113]. As a result, the optical conductivity of graphene can be tuned at different gate voltages. Permittivity of graphene can be obtained for all Fermi energy values by implementing Equation 4.4. Here ϵ_0 is the vacuum permittivity, and t_G is the graphene thickness. As a result, the refractive index of graphene (Equation 4.5) also changes under applied gate voltage, which provides a tunable medium.

$$E_F = \hbar v_F\sqrt{\pi N} \quad (4.3)$$

$$\epsilon(\omega) = 1 + \frac{i\sigma_s}{\omega\epsilon_0 t_G} = \epsilon_r + i\epsilon_i \quad (4.4)$$

$$n = \sqrt{\epsilon(\omega)} \tag{4.5}$$

4.5.2 Results and Discussion

The measured and calculated reflectivity results for SRR-1 are demonstrated in Figure 4.15 (a) and (b). The reflectivity measurements are taken by using Fourier transform infrared (FTIR) spectroscopy at different gate voltages in order to investigate the resonance behavior for different sheet carrier concentrations. Here the voltage difference, ΔV, is defined by $\Delta V = V_g - V_{CNP}$, where V_g is the gate voltage, and $V_{CNP} = 130V$ is the voltage at the charge neutrality point, as shown in Figure 4.14 (a). $\Delta V = -170V$ corresponds to the highest doped case, and hence the highest Fermi energy for graphene. Since the refractive index of the graphene layer, $n = \sqrt{\epsilon(\omega)}$, changes for each different gate voltage, the reflectivity spectrum shifts when the gate voltage is varied. It is seen in both experiment and simulation results that the resonance peak shifts to longer wavelengths as the doping and thus the Fermi energy of the graphene decreases. 62 nm red shift is measured, as the gate voltage approaches the charge neutrality point, $\Delta V = 0V$. The corresponding simulation results show that this shift is 130 nm, as shown in Fig. 3 (b).

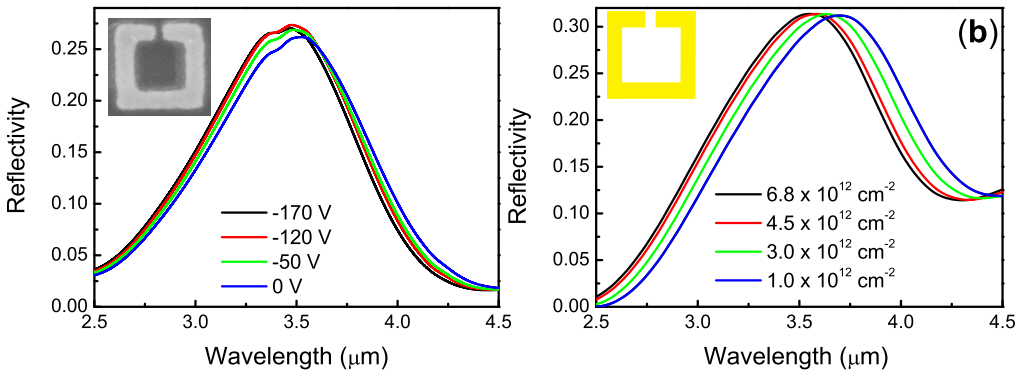

Figure 4.15: Reflectivity spectra of SRR-1 structure (a) experiment, (b) simulation results. The resonance peak shifts to longer wavelengths.

Figure 4.16 shows the reflectivity spectra for SRR-2 array. In this case, 95

nm red-shift in experiments, and 160 nm shift in simulations are obtained. In addition to resonance peaks, curves shift asymmetrically, where the reflection curve at the charge neutrality point becomes the broadest one with the lowest quality factor. The reason is that the interband transitions are allowed over the spectrum for low Fermi energy. Simulation results show larger wavelength shifts than the experiment results for both structures, as demonstrated in Figures 4.15 (b) and 4.16 (b). The possible reasons of this discrepancy can be due to the fabrication imperfections, the defects, and grain boundaries on graphene.

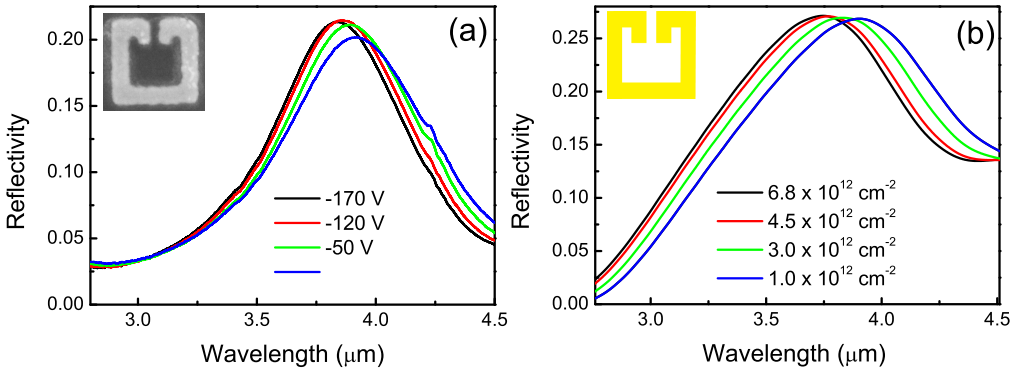

Figure 4.16: Reflectivity spectra of SRR-2 structure (a) experiment, (b) simulation results. The resonance wavelength shifted 95 nm.

Moreover, resonance peaks at each gate voltage is investigated, and the results for SRR-1 and SRR-2 structures are demonstrated in Figure 4.17 (a) and (b), respectively, where the peak-to-peak difference keeps increasing as the doping of the graphene is increased. The results show that SRR-2 exhibits a larger tunability range in reflection spectra compared to SRR-1. Electric field distributions at the resonance wavelengths for SRR-1 and SRR-2 are demonstrated in Figure 4.17 (c) and (d). It is clearly seen that the field is highly localized at the gap region for the polarization indicated in the figures, since the gap of these SRR structures can be excited with x-polarized light.

The gap region plays an important role, since the field is localized inside the gap at the resonance wavelength. Increasing the light-graphene interaction area, as in the case for the SRR-2 structure, results in larger shifts, since the effective mode area is larger compared to SRR-1. For further investigation, effective mode area

inside the gap region is calculated for both of the structures. The effective mode area, A, is the ratio between the total energy density, W(r), per unit length and the peak energy density of the mode (Equations 4.6 and 4.7) [133]. According to this calculation, the effective mode area of SRR-1 is $1100nm^2$, whereas the effective mode area for SRR-2 is $2010nm^2$.

$$A = \frac{1}{max\left\{W(r)\right\}} \int W(r)dA \tag{4.6}$$

$$W(r) = \frac{1}{2} Re\left\{\frac{d[\omega\epsilon(r)]}{d\omega}\right\} \left|E(r)\right|^2 + \frac{1}{2}\mu_0 \left|H(r)\right|^2 \tag{4.7}$$

4.6 Conclusion

In summary, we demonstrated resonance broadening and tuning of split ring resonators by utilizing an epitaxial graphene transistor with transparent top-gate. We obtained a frequency shift by putting a graphene layer between the substrate and SRR layer. Graphene based nanophotonics is an intense research due to a wide range of applications of this phenomenon.

We also demonstrated the resonance tunability of bowtie nanoantennas with the help of electrically gated graphene samples. We obtained a frequency shift, resonance damping, and enhancement by fabricating bowtie structures on a graphene layer. Electrical tuning of antenna resonance with a varying gate bias is studied with a theoretical modeling and confirmed experimentally.

Finally, we showed that the optical response of split ring resonators on graphene can be tuned with a transistor-like device, where the optical conductivity of graphene is modulated by varying the gate voltage. Furthermore, the tuning range can be increased by designing the structures such that the effective mode area between graphene and the localized field becomes larger. The experiment and the simulation results showed a good agreement. It can be foreseen that

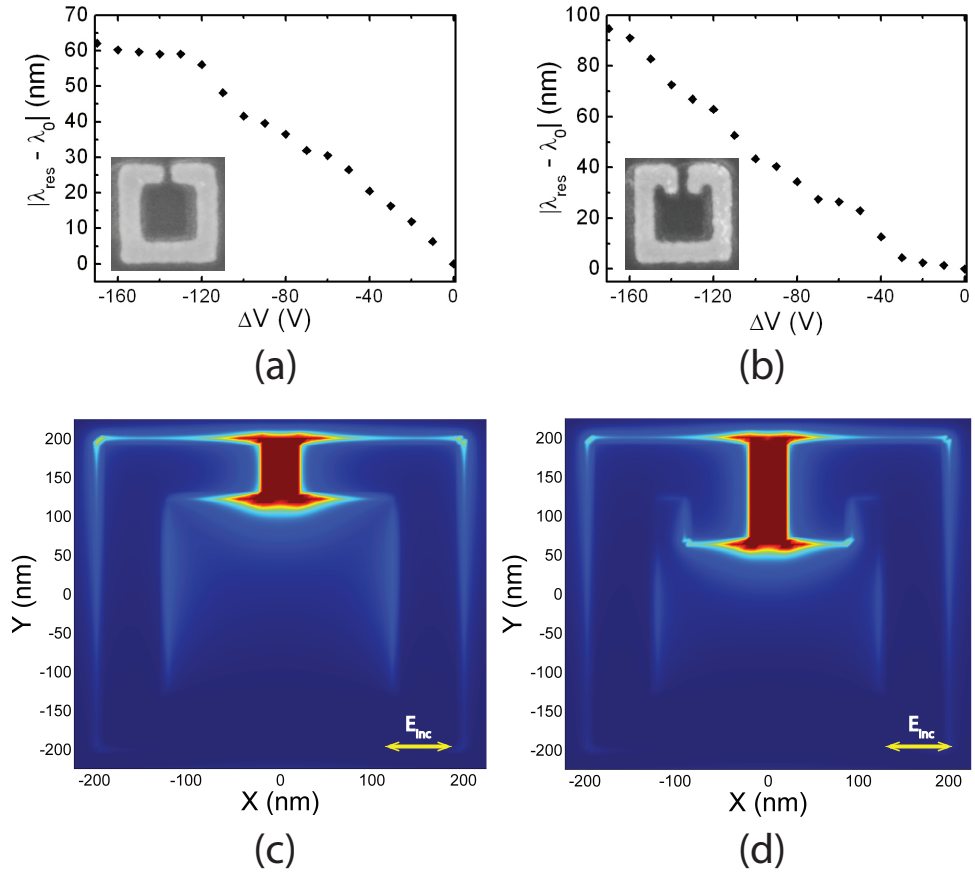

Figure 4.17: Resonance wavelength shift with respect to the reflectivity measurement taken at the charge neutrality point for (a) SRR-1, and (b) SRR-2; λ_{res} represents the resonance wavelength, and λ_0 is the resonance wavelength at the charge neutrality point, $\Delta V = 0V$, so that the difference $|\lambda_{res} - \lambda_0|$ gives the shift with respect to the undoped graphene. Electric field distributions at resonance frequencies for (c) SRR-1 at 3.5 μm, (d) SRR-2 at 3.9 μm; the maximum of the color bar is set to the same value in both figures for comparison, and the electric field is in the x-direction.

the shift at the resonance can be increased with a structure having an effective mode area larger than our proposed SRRs. In addition, the structures can be optimized to operate at even longer wavelengths by scaling up. It is possible to use such devices as tunable sensors, optical switches and modulators.

Chapter 5

Conclusion

We demonstrated the unidirectional beaming through a subwavelength aperture in non-symmetric metallic gratings at microwave frequencies. The role of the spoof surface plasmon resonance at the output interface in the appearance of the strong directional selectivity is demonstrated theoretically with FDTD simulations along with the experiments. The transmission characteristics can strongly differ because the output surface is only responsible for the spatial distribution of the transmitted field. The presented experimental results are such first results that validate the studied mechanism of unidirectional beaming. It is expected that the suggested mechanism can be implemented for a wide frequency range, including when optical frequencies. In particular, for the structures with an asymmetric exit interface, a one-way transmission has been obtained due to the single, off-axis, forward transmitted beam, i.e., the backward transmission is rather weak within a limited range of the observation angle variation. Transmission maps plotted on the frequency-observation-angle plane for the incidence angles, which differ in sign only, are very similar, provided that the input interface is symmetric with respect to the slit. In this case, contributions of the corresponding incident wide beams into the narrow outgoing beam can show the same magnitude at and around the transmission maximum. For the structures with the exit interface being asymmetric with respect to the slit, one-way multiplexing can also occur in the single-beam off-axis regime. For the structures with

a symmetric exit interface, the two resulting off-axis beams, or a single on-axis beam appear in a one-way regime a wide range of the observation angle variation. As a result, one-way, dual-band collimation can be obtained.

We demonstrated a new approach to enable the unidirectional excitation of spoof surface plasmons and the relevant asymmetric extraordinary transmission and beaming. It can be realized in a composite structure that combines a symmetric metallic grating with a single subwavelength slit and a 90^o polarization rotator. This is a good example of how the integration of structures with substantially different properties allows one obtaining new functionalities beyond those associated with each of the individual structures. From the point of view of the metallic grating with a subwavelength slit, the used stacking of the two structures allows the one-way excitation of spoof SPs and the relevant diode-like transmission effect without utilizing anisotropic or nonlinear materials and, furthermore, at normal incidence. For the composite structure, ET can be obtained for s-polarized incident waves that would be impossible while using the grating alone. From the point of view of the metamaterial based 90^o polarization rotator, the diode-like beaming regime would be impossible without stacking with a metallic grating having a subwavelength slit. Reversibility, i.e., ability of the suggested structure to work like a diode in the beaming regime at either s or p polarization, depending on whether the forward or the backward case is considered, is very important. Despite that the performance we used here to demonstrate the suggested mechanism has been designed for microwave frequencies, the main ideas and the results of this paper can be utilized as guidelines for future terahertz and optical frequency designs, which should be a subject of a forthcoming paper.

The proposed metallic grating structures can be utilized to collect contributions from different waves/sources, e.g., in sensing applications.

We have demonstrated the influence of plasmonic lens properties (inner diameter and slit width) on SERS performance. The results show that when the slit width is increased, the SERS performance of plasmonic lens decreases, which is consistent with qualitative explanation. The maximum SERS performance was obtained with the plasmonic lens having 200 nm slit width for all plasmonic lenses

with different ring diameters. The slit width was kept constant (200 nm) to investigate the influence of ring diameter on SERS. The SERS intensity obtained from plasmonic lens having 3.0 m inner diameter is 13.2 times higher compared to planar silver thin film which is consistent with the theoretical calculations. This study suggest that the strong relationship between the surface plasmons and SERS activity can be used to built unique structures to prepare well-defined arrays to use in several applications of SERS.

Then, we present the SERS results for the concentric rings. The proposed design gives more than two orders of magnitude larger signal intensity than plain gold film and nearly one order of magnitude larger than an optimally designed etched-ring plasmonic lens structure. The calculated enhancement factor is $1.67x10^7$ for the coupled-concentric structures which is well beyond this value.

We experimentally and numerically demonstrated that the fractal bowtie antennas operate at longer wavelengths compared to the conventional bowtie antenna of the same size, even though the metallic area is reduced after each fractalization. Furthermore, we showed that the fractal antennas have multiple hot spots, in which the electric field is enhanced and localized. We measured that these hot spots increase the SERS signal. SERS signal intensity at 1075 cm^{-1} is enhanced by a factor of 8 for Fractal-1, and it is enhanced 16 times for Fractal-2 when compared to the conventional bowtie antenna. According to the simulation results, the integrated E-field is 24 times the bowtie antenna for Fractal-1, and 32 times the bowtie antenna for Fractal 2. The experimental results and the simulations showed good agreement. It is possible to use such structures as frequency-selective miniaturized antennas, and efficient SERS substrates.

We demonstrated resonance broadening and tuning of split ring resonators by utilizing an epitaxial graphene transistor with transparent top-gate. We obtained a frequency shift by putting a graphene layer between the substrate and SRR layer.

We also demonstrated the resonance tunability of bowtie nanoantennas with the help of electrically gated graphene samples. We obtained a 113 nm wavelength

shift, resonance damping, and enhancement by fabricating bowtie structures on a graphene layer. Electrical tuning of antenna resonance with a varying gate bias is studied with a theoretical modeling and confirmed experimentally.

Finally, we showed that the optical response of split ring resonators on graphene can be tuned with a transistor-like device, where the optical conductivity of graphene is modulated by varying the gate voltage. Furthermore, the tuning range can be increased by designing the structures such that the effective mode area between graphene and the localized field becomes larger. 62 nm red shift is measured, as the gate voltage approaches the charge neutrality point for the case of a conventional SRR, and the tuning is further increased to 95 nm, when the mode area of the SRR is increased. The experiment and the simulation results showed a good agreement. It can be foreseen that the shift at the resonance can be increased with a structure having an effective mode area larger than our proposed SRRs. In addition, the structures can be optimized to operate at even longer wavelengths by scaling up. It is possible to use graphene based devices as tunable sensors, optical switches and modulators.

Bibliography

[1] H. A. Atwater, "The promise of plasmonics," *Scientific American*, vol. 296, pp. 56–63, 2007.

[2] N. C. Lindquist, P. Nagpal, K. M. McPeak, D. J. Norris, and S. H. Oh, "Engineering metallic nanostructures for plasmonics and nanophotonicst," *Reports on Progress in Physics*, vol. 75, 2012.

[3] H. Raether, *Surface plasmons on smooth and rough surfaces and on gratings*. Springer, 1988.

[4] W. Barnes, A. Dereux, and T. Ebbesen, "Surface plasmon subwavelength optics," *Nature*, vol. 424, pp. 824–830, 2003.

[5] H. Ditlbacher, B. Lamprecht, A. Leitner, and F. R. Aussenegg, "Spectrally coded optical data storage by metal nanoparticles," *Optics Letters*, vol. 8, pp. 563–565, 2000.

[6] H. Atwater and A. Polman, "Plasmonics for improved photovoltaic devices," *Nature Materials*, vol. 9, pp. 205–213, 2010.

[7] K. A. Willets and R. P. V. Duyne, "Localized surface plasmon resonance spectroscopy and sensing," *The Annual Review of Physical Chemistry*, vol. 58, pp. 267–297, 2007.

[8] C. L. Haynes, A. D. McFarland, and R. P. V. Duyne, "Surface-enhanced raman spectroscopy," *Analytical Chemistry*, vol. 77, pp. 338a–346a, 2005.

[9] A. Haes and R. P. V. Duyne, "A unified view of propagating and localized surface plasmon biosensors," *Analytical and Bioanalytical Chemistry*, vol. 379, pp. 920–930, 2004.

[10] J. N. Anker, W. P. Hall, O. Lyandres, N. C. Shah, J. Zhao, and R. P. V. Duyne, "Biosensing with plasmonic nanosensors," *Nature Materials*, vol. 7, pp. 442–453, 2008.

[11] J. B. Pendry, A. J. Holden, D. J. Robbins, and W. J. Stewart, "Magnetism from conductors and enhanced nonlinear phenomena," *IEEE Transactions on Microwave Theory*, vol. 47, pp. 2075–2084, 1999.

[12] R. A. Shelby, D. R. Smith, and S. Schultz, "Experimental verification of a negative index of refraction," *Science*, vol. 292, pp. 77–79, 2001.

[13] D. R. Smith, W. J. Padilla, D. C. Vier, S. C. Nemat-Nasser, and S. Schultz, "Composite medium with simultaneously negative permeability and permittivity," *Physical Review Letters*, vol. 84, pp. 4184–4187, 2000.

[14] K. Aydin, K. Guven, C. M. Soukoulis, and E. Ozbay, "Observation of negative refraction and negative phase velocity in left-handed metamaterials," *Applied Physics Letters*, vol. 86, 2005.

[15] K. Aydin, I. Bulu, K. Guven, M. Kafesaki, C. M. Soukoulis, and E. Ozbay, "Investigation of magnetic resonances for different split-ring resonator parameters and designs," *New Journal of Physics*, vol. 7, 2005.

[16] X. Zhang and Z. Liu, "Superlenses to overcome the diffraction limit," *Nature Materials*, vol. 7, pp. 435–441, 2008.

[17] H. Caglayan, S. Cakmakyapan, S. A. Addae, M. A. Pinard, D. Caliskan, K. Aslan, and E. Ozbay, "Ultrafast and sensitive bioassay using split ring resonator structures and microwave heating," *Applied Physics Letters*, vol. 97, 2010.

[18] R. Schittny, M. Kadic, T. Bckmann, and M. Wegener, "Invisibility cloaking in a diffusive light scattering medium," *Science*, vol. 345, 2014.

[19] F. H. L. Koppens, D. E. Chang, and F. J. G. de Abajo, "Graphene plasmonics: A platform for strong light-matter interactions," *Nano Letters*, vol. 11, pp. 3370–3377, 2011.

[20] T. Kampfrath, L. Perfetti, F. Schapper, C. Frischkorn, and M. Wolf, "Strongly coupled optical phonons in the ultrafast dynamics of the electronic energy and current relaxation in graphite," *Physical Review Letters*, vol. 95, p. 187403, 2005.

[21] K. F. Mak, J. Shan, and T. F. Heinz, "Electronic structure of few-layer graphene: experimental demonstration of strong dependence on stacking sequence," *Physical Review Letters*, vol. 104, p. 176404, 2009.

[22] C. R. M. Breusing and T. Elsaesser, "Ultrafast carrier dynamics in graphite," *Physical Review Letters*, vol. 102, p. 086809, 2009.

[23] A. Bostwick, T. Ohta, T. Seyller, K. Horn, and E. Rotenberg, "Quasiparticle dynamics in graphene," *Nature Physics*, vol. 3, p. 3640, 2007.

[24] A. Bostwick, F. Speck, T. Seyller, K. Horn, M. Polini, R. Asgari, A. H. MacDonald, and E. Rotenberg, "Observation of plasmarons in quasi-freestanding doped graphene," *Scicence*, vol. 328, p. 9991002, 2010.

[25] Y. Yao, M. A. Kats, P. Genevet, N. Yu, Y. Song, J. Kong, and F. Capasso, "Broad electrical tuning of graphene-loaded plasmonic antennas," *Nano Letters*, vol. 13, pp. 1257–1264, 2013.

[26] N. K. Emani, T. F. Chung, X. Ni, A. V. Kildishev, Y. P. Chen, and A. Boltasseva, "Electrically tunable damping of plasmonic resonances with graphene," *Nano Letters*, vol. 12, pp. 5202–5206, 2012.

[27] L. A. Falkovsky and A. A. Varlamov, "Space-time dispersion of graphene conductivity," *European Physics Journal B*, vol. 56, pp. 281–284, 2007.

[28] L. A. Falkovsky and S. S. Pershoguba, "Optical far-infrared properties of a graphene monolayer and multilayer," *Physical Review Letters B*, vol. 76, 2007.

[29] H. A. Bethe, "Theory of diffraction by small holes," *The Physical Review*, vol. 66, 1944.

[30] T. Thio, K. M. Pellerin, R. A. Linke, H. J. Lezec, and T. W. Ebbesen, "Enhanced light transmission through a single subwavelength aperture," *Optics Letters*, vol. 26, pp. 1972–1974, 2001.

[31] H. Raether, "Surface-plasmons on smooth and rough surfaces and on gratings," *Springer Tracts in Modern Physics*, vol. 111, 1988.

[32] J. B. Pendry, L. Martin-Moreno, and F. J. Garcia-Vidal, "Mimicking surface plasmons with structured surfaces," *Science*, vol. 305, pp. 847–848, 2004.

[33] A. P. Hibbins, B. R. Evans, and J. R. Sambles, "Experimental verification of designer surface plasmons," *Science*, vol. 308, pp. 670–672, 2005.

[34] T. W. Ebbesen, H. J. Lezec, A. Degiron, E. Devaux, R. A. Linke, L. Martin-Moreno, and F. J. Garcia-Vidal, "Beaming light from a subwavelength aperture," *Science*, vol. 297, pp. 820–822, 2002.

[35] H. Caglayan, I. Bulu, and E. Ozbay, "Beaming of electromagnetic waves emitted through a subwavelength annular aperture," *Journal of Optical Society of America B*, vol. 23, pp. 419–422, 2006.

[36] S. Cakmakyapan, A. E. Serebryannikov, H. Caglayan, and E. Ozbay, "One-way transmission through the subwavelength slit in nonsymmetric metallic gratings," *Optics Letters*, vol. 35, pp. 2597–2599, 2010.

[37] S. Cakmakyapan, H. Caglayan, A. E. Serebryannikov, and E. Ozbay, "Experimental validation of strong directional selectivity in nonsymmetric metallic gratings with a subwavelength slit," *Applied Physics Letters*, vol. 98, 2011.

[38] S. B. Choi, D. J. Park, Y. K. Jeong, Y. C. Yun, M. S. Jeong, C. C. Byeon, J. H. Kang, Q. H. Park, and D. S. Kim, "Directional control of surface plasmon polariton waves propagating through an asymmetric bragg resonator," *Applied Physics Letters*, vol. 94, 2009.

[39] F. Lopez-Tejeira, S. G. Rodrigo, L. Martin-Moreno, F. J. Garcia-Vidal, E. Devaux, T. W. Ebbesen, J. R. Krenn, I. P. Radko, S. I. Bozhevolnyi, M. U. Gonzalez, J. C. Weeber, and A. Dereux, "Efficient unidirectional nanoslit couplers for surface plasmons," *Nature Physics*, vol. 3, pp. 324–328, 2007.

[40] N. Bonod, E. Popov, L. F. Li, and B. Chernov, "Unidirectional excitation of surface plasmons by slanted gratings," *Optics Express*, vol. 15, pp. 11427–11432, 2007.

[41] I. P. Radko, S. I. Bozhevolnyi, G. Brucoli, L. Martin-Moreno, F. J. Garcia-Vidal, and A. Boltassev, "Efficient unidirectional ridge excitation of surface plasmons," *Optics Express*, vol. 17, pp. 7228–7232, 2009.

[42] A. Roszkiewicz and W. Nasalski, "Unidirectional spp excitation at asymmetrical two-layered metal gratings," *Journal of Physics B-Atomic Molecular and Optical Physics*, vol. 43, 2010.

[43] A. Baron, E. Devaux, J. C. Rodier, J. P. Hugonin, E. Rousseau, C. Genet, T. W. Ebbesen, and P. Lalanne, "Compact antenna for efficient and unidirectional launching and decoupling of surface plasmons," *Nano Letters*, vol. 11, pp. 4207–4212, 2011.

[44] S. Kim, H. Kim, Y. Lim, and B. Lee, "Off-axis directional beaming of optical field diffracted by a single subwavelength metal slit with asymmetric dielectric surface gratings," *Applied Physics Letters*, vol. 90, 2007.

[45] H. Caglayan, I. Bulu, and E. Ozbay, "Off-axis beaming from subwavelength apertures," *Journal of Applied Physics*, vol. 104, no. 7, 2008.

[46] J. J. Chen, Z. Li, S. Yue, and Q. H. Gong, "Efficient unidirectional generation of surface plasmon polaritons with asymmetric single-nanoslit," *Applied Physics Letters*, vol. 97, 2010.

[47] S. Cakmakyapan, A. E. Serebryannikov, H. Caglayan, and E. Ozbay, "Spoof-plasmon relevant one-way collimation and multiplexing at beaming from a slit in metallic grating," *Optics Express*, vol. 20, 2012.

[48] A. Degiron and T. W. Ebbesen, "Analysis of the transmission process through single apertures surrounded by periodic corrugations," *Optics Express*, vol. 12, pp. 3694–3700, 2004.

[49] Y. C. Jun, K. C. Y. Huang, and M. L. Brongersma, "Plasmonic beaming and active control over fluorescent emission," *Nature Communications*, vol. 2, 2011.

[50] L. Zhou, W. J. Wen, C. T. Chan, and P. Sheng, "Electromagnetic-wave tunneling through negative-permittivity media with high magnetic fields," *Physical Review Letters*, vol. 94, 2005.

[51] G. Castaldi, I. Gallina, V. Galdi, A. Alu, and N. Engheta, "Electromagnetic tunneling through a single-negative slab paired with a double-positive bilayer," *Physical Review B*, vol. 83, 2011.

[52] R. Elghanian, J. J. Storhoff, R. C. Mucic, R. L. Letsinger, and C. A. Mirkin, "Selective colorimetric detection of polynucleotides based on the distance-dependent optical properties of gold nanoparticles," *Science*, vol. 277, pp. 1078–1081, 1997.

[53] D. C. Hone, A. H. Haines, and D. A. Russell, "Rapid, quantitative colorimetric detection of a lectin using mannose-stabilized gold nanoparticles," *Langmuir*, vol. 19, pp. 7141–7144, 2003.

[54] B. Pettinger, B. Ren, G. Picardi, R. Schuster, and G. Ertl, "Nanoscale probing of adsorbed species by tip-enhanced raman spectroscopy," *Physical Review Letters*, vol. 92, 2004.

[55] X. M. Lu, M. Rycenga, S. E. Skrabalak, B. Wiley, and Y. N. Xia, "Chemical synthesis of novel plasmonic nanoparticles," *The Annual Review of Physical Chemistry*, vol. 60, pp. 167–192, 2009.

[56] K. Kneipp, H. Kneipp, and J. Kneipp, "Surface-enhanced raman scattering in local optical fields of silver and gold nanoaggregatess - from single-molecule raman spectroscopy to ultrasensitive probing in live cells," *Accounts of Chemical Research*, vol. 39, pp. 443–450, 2006.

[57] H. Kneipp, J. Kneipp, and K. Kneipp, "Surface-enhanced raman optical activity on adenine in silver colloidal solution," *Analytical Chemistry*, vol. 78, pp. 1363–1366, 2006.

[58] M. Moskovits, "Surface-enhanced spectroscopy," *Reviews of Modern Physics*, vol. 57, pp. 83–86, 1985.

[59] M. Kahl, E. Voges, S. Kostrewa, C. Viets, and W. Hill, "Periodically structured metallic substrates for sers," *Sensors and Actuators B*, vol. 51, pp. 285–291, 1998.

[60] N. Guillot, H. Shen, B. Fremaux, O. Peron, E. Rinnert, T. Toury, and M. L. de la Chapelle, "Surface enhanced raman scattering optimization of gold nanocylinder arrays: Influence of the localized surface plasmon resonance and excitation wavelength," *Applied Physics Letters*, vol. 97, 2010.

[61] N. A. Cinel, S. Cakmakyapan, G. Ertas, and E. Ozbay, "Concentric ring structures as efficient sers substrates," *IEEE Journal of Selected Topics in Quantum Electronics*, vol. 19, 2013.

[62] N. A. Cinel, S. Butun, G. Ertas, and E. Ozbay, "Fairy chimney-shaped tandem metamaterials as double resonance sers substrates," *Small*, vol. 9, pp. 531–537, 2013.

[63] M. Kahraman, S. Cakmakyapan, E. Ozbay, and M. Culha, "An array of surface-enhanced raman scattering substrates based on plasmonic lenses," *Annalen der Physik*, vol. 524, pp. 663–669, 2012.

[64] Y. Xie, A. R. Zakharian, J. V. Moloney, and M. Mansuripur, "Transmission of light through slit apertures in metallic films," *Optics Express*, vol. 12, pp. 6106–6121, 2004.

[65] W. L. Barnes, "Surface plasmon-polariton length scales: a route to sub-wavelength optics," *Journal of Optics A - Pure and Applied Optics*, vol. 8, pp. 87–93, 2006.

[66] Z. W. Liu, J. M. Steele, W. Srituravanich, Y. Pikus, C. Sun, and Z. X, "Focusing surface plasmons with a plasmonic lens," *Nano Letters*, vol. 5, pp. 1726–1729, 2005.

[67] W. B. Chen, D. C. Abeysinghe, R. L. Nelson, and Q. W. Zhan, "Plasmonic lens made of multiple concentric metallic rings under radially polarized illumination," *Nano Letters*, vol. 9, pp. 4320–4325, 2009.

[68] J. C. Love, L. A. Estroff, J. K. Kriebel, R. G. Nuzzo, and G. M. Whitesides, "Self-assembled monolayers of thiolates on metals as a form of nanotechnology," *Chemical Reviews*, vol. 105, pp. 1103–1169, 2005.

[69] A. Campion and P. Kambhampati, "Surface-enhanced raman scattering," *Chemical Society Reviews*, vol. 27, pp. 241–250, 1998.

[70] Z. Liu, J. M. Steele, W. Srituravanich, Y. Pikus, C. Sun, and X. Zhang, "Focusing surface plasmons with a plasmonic lens," *Nano Letters*, vol. 5, pp. 1726–1729, 2005.

[71] C. Genet and T. W. Ebbesen, "Light in tiny holes," *Nature*, vol. 445, pp. 39–46, 2007.

[72] S. Mahajan, M. Abdelsalam, Y. Suguwara, S. Cintra, A. Russell, J. Baumberg, and P. Bartlett, "Tuning plasmons on nano-structured substrates for nir-sers," *Physical Chemistry Chemical Physics*, vol. 9, pp. 104–109, 2007.

[73] H. Ditlbacher, J. R. Krenn, N. Felidj, B. Lamprecht, G. Schider, M. Salerno, A. Leitner, and F. R. Aussenegg, "Fluorescence imaging of surface plasmon fields," *Applied Physics Letters*, vol. 80, no. 3, 2002.

[74] J. M. Steele, Z. W. Liu, Y. Wang, and X. Zhang, "Resonant and non-resonant generation and focusing of surface plasmons with circular gratings," *Optics Express*, vol. 14, pp. 5664–5670, 2006.

[75] J. J. Miao, Y. S. Wang, C. F. Guo, Y. Tian, S. M. Guo, Q. Liu, and Z. P. Zhou, "Plasmonic lens with multiple-turn spiral nano-structures," *Plasmonics*, vol. 6, pp. 235–239, 2011.

[76] H. Ditlbacher, J. R. Krenn, A. Hohenau, A. Leitner, and F. R. Aussenegg, "Efficiency of local light-plasmon coupling," *Applied Physics Letters*, vol. 83, pp. 3665–3667, 2003.

[77] E. C. L. Ru, E. Blackie, M. Meyer, and P. G. Etchegoin, "Surface enhanced raman scattering enhancement factors: a comprehensive study," *Journal of Physical Chemistry C*, vol. 111, pp. 13794–13803, 2007.

[78] E. C. L. Ru, E. Blackie, M. Meyer, and P. G. Etchegoin, "Plasmon-sampled surface-enhanced raman excitation spectroscopy," *Journal of Physical Chemistry B*, vol. 107, pp. 7426–7433, 2003.

[79] A. D. McFarland, M. A. Young, J. A. Dieringer, and R. P. V. Duyne, "Wavelength-scanned surface-enhanced raman excitation spectroscopy," *Journal of Physical Chemistry B*, vol. 109, pp. 11279–11285, 2005.

[80] M. G. Banaee, P. Peng, E. D. Diebold, E. Mazur, and K. B. Crozier, "Mixed dimer double resonance substrates for surface-enhanced raman spectroscopy," *2010 Conference on Lasers and Electro-Optics (CLEO) and Quantum Electronics and Laser Science Conference (QELS)*, 2010.

[81] Y. Z. Chu, M. G. Banaee, and K. B. Crozier, "Double-resonance plasmon substrates for surface-enhanced raman scattering with enhancement at excitation and stokes frequencies," *ACS Nano*, vol. 4, pp. 2804–2810, 2010.

[82] L. J. Wan, M. Terashima, H. Noda, and M. Osawa, "Molecular orientation and ordered structure of benzenethiol adsorbed on gold(111)," *Journal of Physical Chemistry B*, vol. 104, pp. 3563–3569, 2000.

[83] C. M. Whelan, M. R. Smyth, and C. J. Barnes, "Hreels, xps, and electrochemical study of benzenethiol adsorption on au(111)," *Langmuir*, vol. 15, pp. 116–126, 1999.

[84] A. Kinkhabwala, Z. F. Yu, S. H. Fan, Y. Avlasevich, K. Mullen, and W. E. Moerner, "Large single-molecule fluorescence enhancements produced by a bowtie nanoantenna," *Nature Photonics*, vol. 3, pp. 654–657, 2009.

[85] B. J. Roxworthy, K. D. Ko, A. Kumar, K. H. Fung, E. K. Chow, G. L. Liu, N. X. Fang, and K. C. T. Jr., "Application of plasmonic bowtie nanoantenna arrays for optical trapping, stacking, and sorting," *Nano Letters*, vol. 12, pp. 796–801, 2012.

[86] P. J. Schuck, D. P. Fromm, A. Sundaramurthy, G. S. Kino, and W. E. Moerner, "Improving the mismatch between light and nanoscale objects with gold bowtie nanoantennas," *Physical Review Letters*, vol. 94, 2005.

[87] L. Wang and X. F. Xu, "High transmission nanoscale bowtie-shaped aperture probe for near-field optical imaging," *Applied Physics Letters*, vol. 90, 2007.

[88] N. K. Emani, T. F. Chung, X. J. Ni, A. V. Kildishev, Y. P. Chen, and A. Boltasseva, "Electrically tunable damping of plasmonic resonances with graphene," *Nano Letters*, vol. 12, pp. 5202–5206, 2012.

[89] N. K. Emani, T. F. Chung, X. J. Ni, A. V. Kildishev, Y. P. Chen, and A. Boltasseva, "Free-standing optical gold bowtie nanoantenna with variable gap size for enhanced raman spectroscopy," *Nano Letters*, vol. 10, p. 49524955, 2010.

[90] D. P. Fromm, A. Sundaramurthy, A. Kinkhabwala, P. J. Schuck, G. S. Kino, and W. E. Moerner, "Exploring the chemical enhancement for surface-enhanced raman scattering with au bowtie nanoantennas," *Journal of Chemical Physics*, vol. 124, p. 061101, 2006.

[91] B. B. Mandelbrot, "Fractal geometry - what is it, and what does it do," *Proceedings of the Royal Society of London: Series A*, vol. 423, pp. 3–16, 1989.

[92] J. H. Zhu, A. Hoorfar, and N. Engheta, "Bandwidth, cross-polarization, and feed-point characteristics of matched hilbert antennas," *IEEE Antenna and Wireless Proceedings*, vol. 2, pp. 2–5, 2003.

[93] V. Crnojevic-Bengin, V. Radonic, and B. Jokanovic, "Fractal geometries of complementary split-ring resonators," *IEEE Transactions on Microwave Theory*, vol. 56, pp. 2312–2321, 2008.

[94] D. H. Werner and S. Ganguly, "An overview of fractal antenna engineering research," *IEEE Antennas and Propagation*, vol. 45, pp. 38–57, 2003.

[95] G. Volpe, G. Volpe, and R. Quidant, "Fractal plasmonics: subdiffraction focusing and broadband spectral response by a sierpinski nanocarpet," *Optics Express*, vol. 19, pp. 3612–3618, 2011.

[96] S. Sederberg and A. Y. Elezzabi, "Sierpinski fractal plasmonic antenna: a fractal abstraction of the plasmonic bowtie antenna," *Optics Express*, vol. 19, pp. 10456–10461, 2011.

[97] J. S. Dahele and K. F. Lee, "On the resonant frequencies of the triangular patch antenna," *IEEE Transactions and Antenna Propagation*, vol. 35, pp. 100–101, 1987.

[98] L. Novotny, "Effective wavelength scaling for optical antennas," *Physical Review Letters*, vol. 98, 2007.

[99] J. Anguera, C. Puente, C. Borja, R. Montero, and J. Soler, "Small and high-directivity bow-tie patch antenna based on the sierpinski fractal," *Microwave and Optical Technology Letters*, vol. 31, pp. 239–241, 2001.

[100] G. W. Bryant, F. J. G. D. Abajo, and J. Aizpurua, "Mapping the plasmon resonances of metallic nanoantennas," *Nano Letters*, vol. 8, pp. 631–636, 2008.

[101] E. C. E. J. Smythe and F. Capasso, "Optical properties of surface plasmon resonances of coupled metallic nanorods," *Optics Express*, vol. 15, pp. 7439–7447, 2007.

[102] N. J. H. E. Prodan, C. Radloff and P. Nordlander, "A hybridization model for the plasmon response of complex nanostructures," *Science*, vol. 302, pp. 419–422, 2003.

[103] N. Berkovitch and M. Orenstein, "Thin wire shortening of plasmonic nanoparticle dimers: The reason for red shifts," *Nano Letters*, vol. 11, pp. 2079–2082, 2011.

[104] K. D. Alexander, K. Skinner, S. P. Zhang, H. Wei, and R. Lopez, "Tunable sers in gold nanorod dimers through strain control on an elastomeric substrate," *Nano Letters*, vol. 10, pp. 4488–4493, 2010.

[105] S. J. Lee, A. R. Morrill, and M. Moskovits, "Hot spots in silver nanowire bundles for surface-enhanced raman spectroscopy," *Journal of American Chemical Soceity*, vol. 128, pp. 2200–2201, 2006.

[106] S. M. Asiala and Z. D. Schultz, "Characterization of hotspots in a highly enhancing sers substrate," *Analyst*, vol. 136, pp. 4472–4479, 2011.

[107] K. H. Hsu, J. H. Back, K. H. Fung, P. M. Ferreira, M. Shim, and N. X. Fang, "Sers em field enhancement study through fast raman mapping of sierpinski carpet arrays," *Journal of Raman Spectroscopy*, vol. 41, pp. 1124–1130, 2010.

[108] K. S. Novoselov, A. K. Geim, S. V. Morozov, D. Jiang, M. I. Katsnelson, I. V. Grigorieva, S. V. Dubonos, and A. A. Firsov, "Two-dimensional gas of massless dirac fermions in graphene," *Nature*, vol. 438, pp. 197–200, 2005.

[109] K. I. Bolotin, K. J. Sikes, Z. Jiang, M. Klima, G. Fudenberg, J. Hone, P. Kim, and H. Stormer, "Ultrahigh electron mobility in suspended graphene," *Solid State Communications*, vol. 146, pp. 351–355, 2008.

[110] K. S. Novoselov, A. K. Geim, S. V. Morozov, D. Jiang, Y. Zhang, S. V. Dubonos, I. V. Grigorieva, and A. A. Firsov, "Electric field effect in atomically thin carbon films," *Science*, vol. 306, pp. 666–669, 2004.

[111] Y. Zhang, Y. W. Tan, H. L. Stormer, and P. Kim, "Experimental observation of the quantum hall effect and berrys phase in graphene," *Nature*, vol. 438, p. 201204, 2005.

[112] A. B. X. Du, I. Skachko and E. Y. Andrei, "Approaching ballistic transport in suspended graphene," *Nature Nanotechnology*, vol. 3, pp. 491–495, 2008.

[113] Z. Q. Li, E. A. Henriksen, Z. Jiang, Z. Hao, M. C. Martin, P. Kim, H. L. Stormer, and D. N. Basov, "Dirac charge dynamics in graphene by infrared spectroscopy," *Nature Physics*, vol. 4, pp. 532–535, 2008.

[114] F. Wang, Y. Zhang, C. Tian, C. Girit, A. Zettl, M. Crommie, and Y. R. Shen, "Gate-variable optical transitions in graphene," *Science*, vol. 320, pp. 206–209, 2008.

[115] A. K. Geim and K. S. Novoselov, "The rise of graphene," *Nature Materials*, vol. 6, pp. 183–191, 2007.

[116] A. H. C. Neto, "Electronic and structural properties of graphene," *Abstracts of Papers of the American Chemical Society*, vol. S 238, 2009.

[117] F. Rana, "Graphene terahertz plasmon oscillators," *IEEE Transactions on Nanotechnology*, vol. 7, pp. 91–99, 2008.

[118] K. I. Bolotin, K. J. Sikes, J. Hone, H. L. Stormer, and P. Kim, "Temperature-dependent transport in suspended graphene," *Physical Review Letters*, vol. 101, 2008.

[119] J. Hass, W. A. de Heer, and E. H. Conrad, "The growth and morphology of epitaxial multilayer graphene," *Journal of Physics: Condensed Matter*, vol. 20, 2008.

[120] X. S. Li, W. W. Cai, J. H. An, S. Kim, J. Nah, D. X. Yang, R. D. Piner, A. Velamakanni, I. Jung, E. Tutuc, S. K. Banerjee, L. Colombo, and R. S. Ruoff, "Large-area synthesis of high-quality and uniform graphene films on copper foils," *Science*, vol. 324, p. 13121314, 2009.

[121] V. V. Khardikov, E. O. Iarko, and S. L. Prosvirnin, "Trapping of light by metal arrays," *Journal of Optics*, vol. 12, p. 045102, 2010.

[122] J. Kim, H. Son, D. J. Cho, B. Geng, W. Regan, S. Shi, K. Kim, A. Zettl, Y. Shen, and F. Wang, "Electrical control of optical plasmon resonance with graphene," *Nano Letters*, vol. 12, p. 55985602, 2012.

[123] A. K. Geim and K. Novoselov, "The rise of graphene," *Nature Materials*, vol. 6, pp. 183–191, 2007.

[124] Y. Liu, R. F. Willis, K. V. Emtsev, and T. Seyller, "Plasmon dispersion and damping in electrically isolated two-dimensional charge sheets," *Physical Review Letters B*, vol. 78, p. 201403, 2008.

[125] C. Tegenkamp, H. Pfnur, T. Langer, J. Baringhau, and H. WSchumacher, "Plasmon electron-hole resonance in epitaxial graphene," *Journal of Physics: Condensed Matter*, vol. 23, p. 012001, 2011.

[126] V. W. Brar, S. Wickenburg, M. Panlasigui, C. Park, T. O. Wehling, Y. Zhang, R. Decker, C. Girit, A. V. Balatsky, S. G. Louie, A. Zettl, and M. F. Crommie, "Observation of carrier-density-dependent many-body effects in graphene via tunneling spectroscopy," *Physical Review Letters*, vol. 104, p. 036805, 2010.

[127] J. N. Chen, M. Badioli, P. Alonso-Gonzalez, S. Thongrattanasiri, F. Huth, J. Osmond, M. Spasenovic, A. Centeno, A. Pesquera, P. Godignon, A. Z. Elorza, N. Camara, F. J. G. de Abajo, R. Hillenbrand, and F. H. L. Koppens, "Optical nano-imaging of gate-tunable graphene," *Nature*, vol. 487, pp. 77–81, 2012.

[128] M. M. Ugeda, I. Brihuega, F. Guinea, and J. M. Gomez-Rodriguez, "Missing atom as a source of carbon magnetism," *Physical Review Letters*, vol. 104, p. 096804, 2010.

[129] K. Kim, H. Kang, C. Y. Lee, and W. S. Yun, "Enhanced response to molecular adsorption of structurally defective graphene," *JVST B*, vol. 31, p. 030602, 2013.

[130] Z. Cheng, Q. Zhou, C. Wang, Q. Li, and Y. Fang, "Toward intrinsic graphene surfaces: a systematic study on thermal annealing and wet-chemical treatment of sio2-supported graphene devices," *Nano Letters*, vol. 11, pp. 767–771, 2011.

[131] S. Russo, M. F. Craciun, M. Yamamoto, A. F. Morpurgo, and S. Tarucha, "Contact resistance in graphene-based devices," *Physica E*, vol. 42, pp. 7677–679, 2010.

[132] S. Adam, E. H. Hwang, V. M. Galitski, and S. D. Sarma, "A self-consistent theory for graphene transport," *Proceedings of the National Academy of Sciences*, vol. 104, pp. 18392–18397, 2007.

[133] L. Landau, E. Lifshitz, and L. Pitaevskii, *Electrodynamics of Continuous Media. Vol. 8.* Butterworth-Heinemann, 1984.

Appendix A

Publications in SCI journals

1. E. Arslan, S. Cakmakyapan, P. Aydogan, W. Strupinski, E. Ozbay and S. Suzer, *"Amplifying the chemically addressed electrical properties of graphene layers grown on C- and Si- faces of SiC by voltage contrast XPS,"* ACS Nano (Under Review).

2. S. Cakmakyapan, H. Caglayan, and E. Ozbay, *"Coupling enhancement of split ring resonators on graphene,"* Carbon 80, 351-355 (2014).

3. S. Cakmakyapan, N. Cinel, A. O. Cakmak, and E. Ozbay, *"Validation of Electromagnetic Field Enhancement in Near-Infrared through Sierpinski Fractal Nanoantennas ,"* Optics Express 22, 19504-19512 (2014).

4. Z. Li, S. Cakmakyapan, B. Butun, C. Daskalaki, S. Tzortzakis, X. Yang, and E. Ozbay, *"Fano resonances in THz metamaterials composed of continuous metallic wires and split ring resonators,"* Optics Express 22 (22), 26572-26584 (2014).

5. T. Ciuk, S. Cakmakyapan, E. Ozbay, P. Caban, I. Pasternak, A. Krajewska, J. Szmidt, W. Strupinski, *"Step-edge-induced resistance anisotropy in commercially feasible bilayer graphene on SiC,"* Journal of Applied Physics 116 (12), 123708 (2014).

6. S. Cakmakyapan, L. Sahin, F. Pierini, and E. Ozbay, *"Resonance tuning and broadening of bowtie nanoantennas on graphene,"* Photonics and Nanostructures: Fundamentals and Applications 12, 199-204 (2014).

7. S.B. Lisesivdin, G. Atmaca, E. Arslan, S. Cakmakyapan, . Kazar, S. Btn, J. Ul-Hassan, E. Janzn, E. zbay, *"Extraction and scattering analyses of 2D and bulk carriers in epitaxial graphene-on-SiC structure,"*, Physica E: Low-dimensional Systems and Nanostructures 63, 87-92 (2014)

8. E. Arslan, S. Cakmakyapan, O. Kazar, S. Butun, B. Lisesivdin, N. A. Cinel, G. Ertas, . Ardali, E. Tiras and E. Ozbay, *"SiC Substrate effects on electron transport in the epitaxial graphene layer,* Electronic Material Letters 10, 411-416 (2014)

9. S. Cakmakyapan, L. Sahin, F. Pierini, W. Strupinski, and E. Ozbay, *"Resonance broadening and tuning of split ring resonators by top-gated epitaxial graphene on SiC substrate,"* Applied Physics Letters 103 (2013).

10. M. Mutlu, S. Cakmakyapan, A. E. Serebryannikov, and E. Ozbay, *"One-way reciprocal spoof surface plasmons and relevant reversible diodelike beaming,"* Physical Review B 87 (2013).

11. N. A. Cinel, S. Cakmakyapan, G. Ertas, and E. Ozbay, *"Concentric Ring Structures as Efficient SERS Substrates,"* IEEE JSTQE 19 (2013).

12. E. Tiras, S. Ardali, T. Tiras, E. Arslan, S. Cakmakyapan, O. Kazar, J. Hassan, E. Janzen, and E. Ozbay, *"Effective mass of electron in monolayer graphene: Electron-phonon interaction,"* Journal of Applied Physics 113 (2013).

13. S. Cakmakyapan, A. E. Serebryannikov, H. Caglayan, and E. Ozbay, *"Spoof-plasmon relevant one-way collimation and multiplexing at beaming from a slit in metallic grating,"* Optics Express 20, 26636-26648 (2012).

14. M. Kahraman, S. Cakmakyapan, E. Ozbay, and M. Culha, *"An array of surface-enhanced Raman scattering substrates based on plasmonic lenses,"* Ann.

Phys-Berlin 524, 663-669 (2012).

15. S. Cakmakyapan, H. Caglayan, A. E. Serebryannikov, and E. Ozbay, *"Experimental validation of strong directional selectivity in nonsymmetric metallic gratings with a subwavelength slit,"* Applied Physics Letters 98 (2011).

16. H. Caglayan, S. Cakmakyapan, S. A. Addae, M. A. Pinard, D. Caliskan, K. Aslan, and E. Ozbay, *"Ultrafast and sensitive bioassay using split ring resonator structures and microwave heating,"* Applied Physics Letters 97 (2010).

17. S. Cakmakyapan, A. E. Serebryannikov, H. Caglayan, and E. Ozbay, *"One-way transmission through the subwavelength slit in nonsymmetric metallic gratings,"* Optics Letters 35, 2597-2599 (2010).

18. S. A. Addae, M. A. Pinard, H. Caglayan, S. Cakmakyapan, D. Caliskan, E. Ozbay, and K. Aslan, *"Rapid and Sensitive Colorimetric ELISA using Silver Nanoparticles, Microwaves and Split Ring Resonator Structures,"* Nano Biomedicine and Engineering 2, 155-164 (2010).